

NASA Contractor Report 4417

Development of Theoretical Models of Integrated Millimeter Wave Antennas

K. Sigfrid Yngvesson and Daniel H. Schaubert

CONTRACT NAS1-18310
DECEMBER 1991

NASA

NASA Contractor Report 4417

Development of Theoretical Models of Integrated Millimeter Wave Antennas

K. Sigfrid Yngvesson and Daniel H. Schaubert
University of Massachusetts
Department of Electrical and Computer Engineering
Amherst, Massachusetts

Prepared for
Langley Research Center
under Contract NAS1-18310



National Aeronautics and
Space Administration
Office of Management
Scientific and Technical
Information Program

1991

Table of Contents

	ABSTRACT	v
1.	INTRODUCTION	1
2.	LTSA SINGLE ELEMENT MODELING	1
	2.1. <i>Further Experimental Data on LTSA Single Elements</i>	1
	2.2. <i>Analysis of Cross-Polarization Data on Single LTSAs</i>	3
	2.3. <i>Effect of Cross-Polarized Radiation on the Directivity, and Gain of Single Element LTSAs</i>	4
	2.4. <i>Moment Method Analysis of Linearly Tapered Slot Antennas</i>	7
3.	ANALYSIS AND EXPERIMENTAL STUDIES OF LTSA ARRAYS	8
	3.1. <i>Formulation of Analysis</i>	8
	3.2. <i>Numerical Results</i>	11
	3.3. <i>Remarks</i>	13
	3.4. <i>Continued Experimental Study of LTSA Arrays</i>	14
4.	DESIGN OF A MIXER SUITABLE FOR USE WITH LTSA ARRAYS	16
5.	CONCLUSIONS	17
	5.1 <i>Analytical Modeling</i>	17
	5.2 <i>Experimental Modeling</i>	17
6.	PUBLICATIONS AND THESES ON THE BASIS OF THE CONTRACT	18
	6.1. <i>Theses</i>	18
	6.2. <i>Publications</i>	18
7.	REFERENCES	19
8.	TABLES	21
9.	FIGURE CAPTIONS AND FIGURES	24
	APPENDIX A	87
	APPENDIX B	89

Abstract

This report summarizes the results obtained during the three year contract "Development of Theoretical Models of Integrated Millimeter Wave Antennas".

The task *LTSA Single Element Modeling* has been completed. Extensive data are presented, especially for the cross-polarized radiation properties of such elements. The question of how to correctly predict the directivity of LTSA elements has been resolved, by taking the cross-polarized pattern into account. The directivity now is in good agreement with the measured gain. A moment-method program predicts radiation patterns (co- and cross-polarized) for air LTSAs with excellent agreement with experimental data.

Further work using the moment-method program showed that the phase center is located at different points in the different planes (E or H). It was also found that the longitudinal currents along the inner edges of the LTSA plates give rise to most of the cross-polarized radiation in the diagonal plane. Much lower cross-polarization has been found (empirically) for Vivaldi elements in a continuation of this work on an industrial contract.

A moment-method program has also been developed for the task *LTSA Array Modeling*. Computations performed with this program are in excellent agreement with published results for dipole and monopole arrays. Computations for more complicated structures are in good agreement with waveguide simulator experiments. Thus, a basic approach has been developed successfully, which is now ready for application in other programs, and the effort will continue with support from a major electronics company.

Empirical modeling of LTSA arrays has demonstrated that the maximum theoretical element gain (for a large array with negligible edge effects) can be obtained. Formulations were also developed for calculating the aperture efficiency of LTSA arrays used in reflector systems. The importance of incorporating cross-polarized patterns in such calculations is emphasized. It was shown that LTSA arrays used in multi-beam systems can achieve aperture efficiencies which are comparable to the highest efficiency which can be obtained with waveguide feeds, but with a considerable advantage in terms of higher packing density.

The task *Preliminary Design of a Mixer Suitable for Use With LTSA Arrays* has been completed. Conversion loss of 10 dB was demonstrated at 35 GHz, using inexpensive diodes, with a microstrip circuit design.

One Ph.D. thesis which has been supported by the contract, was completed. Major parts of another Ph.D. thesis, as well as two M.Sc. theses were also supported.

1. INTRODUCTION

This report summarizes the results obtained for the three year contract "Development of Theoretical Models of Integrated Millimeter Wave Antennas". The main tasks specified in our schedule for the contract were (with numbers as designated in the statement of work as amended):

4.1. *LTSA Single Element Modeling*

4.2. *LTSA Array Modeling*

4.3. *LTSA with Receiver Elements Modeling*

Task 4.4, *LTSA with Receiver Elements Array Modeling*, was eliminated when the contract was descoped during the middle of the second year.

The three topics mentioned above are discussed in Chapters 2, 3, and 4, respectively. We also give, in Section 5, our conclusions and in Section 6, a list of publications and theses which have resulted from the contract. Finally, appendices give data which are useful in executing the LTSA array analysis program.

2. LTSA SINGLE ELEMENT MODELING

2.1. *Further Experimental Results on LTSA Single Elements*

Experimental data have been produced to further elucidate the influence of various parameters on the performance of single elements, and for comparison with the properties of the same elements in the array environment. A new millimeter wave mini-range has been employed since the beginning of this contract, and has enabled us to obtain a large amount of data without loading the busy antenna range in the ANTLAB. The dynamic range of the new mini-range is about 25 dB, and it is fully computer controlled, so that calculations can be conveniently performed on the data.

Most of the measurements have been performed between 20 and 50 GHz, and a split waveguide block was usually employed to feed the antennas. For comparison, we also took some measurements on identical LTSA's for which the detection was performed with a diode directly soldered to the narrow portion of the slot. The latter method represents the minimum possible perturbation on the fields of the ideal antenna shape used in the theoretical calculations, and was the main method we had used previously for this reason. The radiation patterns for LTSA's with a waveguide block, and a standard waveguide detector, were found to be essentially identical in the main beam region, and only showed minor differences in the sidelobes. The waveguide block employed had a very small cross-section, in order to perturb the LTSA's as little as possible. A comparison of radiation patterns obtained with the two detection methods is shown in Figure 2.1.1.

Further data were also generated for comparison with the traveling-wave antenna data given by Zucker [1]. The results which will be presented in this report are for the beamwidth and directivity as a function of normalized length (in wavelengths). The measurements have been performed on LTSA's fabricated on Kapton substrates (dielectric constant 3.5),

of sufficient width that finite width effects should be negligible. Frequencies from 25 to 49 GHz were used, with substrate thickness of 5 mil, as well as one series using a 2 mil substrate at 25 GHz. This results in values of t/λ_0 from 0.004 to 0.021. The directivities are higher than previously measured. One reason for this is that the signal-to-noise ratio generally was better in these measurements, than in the previous measurements on Kapton antennas. The latter were performed at 94 GHz, at which frequency the diode sensitivity is much lower. The directivity has been plotted in Figure 2.1.2 and compared with the standard traveling-wave antenna data from Zucker [1]. The directivity is quite close to the *maximum gain* case used by Zucker, whereas previously measured directivities were at the *low side-lobe* curve, or below that. One can also find the dielectric thickness which yields the highest directivity. For shorter antennas (up to about $6-8 \lambda$) there is very little difference between the three thinnest substrates, whereas the thickest substrate has lower directivity. At the longer lengths, the directivity starts to drop off, starting with the thickest substrate, etc. The two thinnest substrates have quite similar directivities up to the longest lengths measured. The optimum directivity thus is a slow function of dielectric thickness, with a somewhat thinner substrate favored at the longer lengths. The beam-efficiency to the -10 dB level has also been plotted, see Figure 2.1.3. Typical values are about 60-80 % for the three lowest values of t/λ , and 50% for $t/\lambda = 0.021$, compared with previously obtained data of about 30%. The beamwidths at the -3 dB and -10 dB levels, respectively, are given in Figure 2.1.4 and 2.1.5. Note that the normalized dielectric thickness has very little effect on the -10 dB beamwidth. It does, however, have a major effect on the beam efficiency, which indicates that the sidelobe level goes up for the largest dielectric thickness (see Fig. 2.1.3)

We have also investigated the dependence of the beamwidths and directivity on opening angle, and show the directivity versus length for several different opening angles of the LTSA in Figure 2.1.6. There is a clear range of opening angles which results in optimum directivity, from about 7 to 11° . It can be surmised that for wider opening angles, the traveling-wave description is no longer so accurate. For example, the theoretical model of Janaswamy and Schaubert assumes that the power in the traveling-wave is conserved. There are indications from other work [DeFonzo, private communication] at the University of Massachusetts that for large opening angles (about 35°), other models have to be employed. This is a range of antenna parameters which is more of interest for antennas with good time-response (i.e. extremely broad-band), and these will not be considered for the NASA contract.

The above measurements have further established the usefulness of regarding the dielectric-based LTSA's as traveling-wave antennas, and shown how to design such antennas so that the directivity approaches the maximum attainable for a traveling-antenna of a given length, at least for substrates with dielectric constant close to that of Kapton (3.5). The effect of decreasing the dielectric constant to 2.2, or increasing it to 10.2, can be seen in the radiation patterns shown in Fig. 2.1.7. No large effects occur upon decreasing the dielectric constant, while increasing ϵ_r to 10.2 causes major changes in the radiation patterns. The directivity versus normalized length for these three substrates is compared in Figure 2.1.8. The $\epsilon_r = 2.2$ case has a directivity larger than for $\epsilon_r = 3.5$, and essen-

tially along Zucker's "high gain" curve. The directivity of the $\epsilon_r = 10.2$ LTSA "saturates" at about 12.5 dB, and this antenna clearly does not follow the behavior expected for a traveling-wave type antenna. Absolute gain measurements have also been made, however, and these point to the fact that some caution must be exercised in using the directivity, as obtained by our standard procedure. This procedure consists in integrating the measured radiation patterns in the E- and H-planes, and using a smooth sine-cosine interpolation between these planes. The equations used are given below:

$$D = \frac{4\pi [U_E^2 + U_H^2]_{\theta=0}}{\int_0^\pi \int_{-\pi}^\pi [U_E^2 + U_H^2] \sin \theta d\theta d\phi} \quad (2.1.1)$$

$$= \frac{8U_1^2(\theta = 0)}{\int_{-\pi}^\pi [U_1^2 + U_2^2] \sin \theta d\theta}$$

$$\eta_B = \frac{\int_0^\pi \int_0^{\theta^*} [U_E^2 + U_H^2] \sin \theta d\theta d\phi}{\int_0^\pi \int_{-\pi}^\pi [U_E^2 + U_H^2] \sin \theta d\theta d\phi} \quad (2.1.2)$$

Here, $U_E = U_1 \cos \phi$ and $U_H = U_2 \sin \phi$, where U_1 and U_2 are the measured field patterns in the E- and H-planes, respectively. The integration for the efficiencies is extended to an angle θ^* , which may either be the angle subtended by the reflector, or the -10 dB level of the measured pattern.

The method we have described for calculating the directivity has also been used on a standard gain horn, and the calculated directivity from the measured patterns of this horn agree with the nominal gain specified by the manufacturer within 0.2 dB. This should therefore give us an estimate of the error for the efficiency due to errors in the actual radiation pattern data, and the assumption of a smooth variation between the E- and H-planes.

The absolute gain measured for a single element is compared with the estimated directivity in Table 2.1.1, and it can be seen that the measured gain is considerably lower than the estimated directivity. The above procedure for estimating the directivity is fairly accurate, but does not take into account losses to cross-polarization. While we have known that the cross-polarization response close to the main beam, and in the two major planes, is very low, measurements in other planes have not been performed until recently. These are described in the next section. We also describe in Section 2.3, a method for correcting the estimated directivity and efficiency, by using the measured values for the gain.

2.2. Analysis of Cross-Polarization Data on Single LTSA's

Measurements of cross-polarized radiation from LTSA antennas were performed. An extensive set of co- and cross-polarized radiation patterns have been obtained for six antennas. The patterns were measured at several frequencies covering a range of antenna lengths from approximately one-half wavelength (appropriate for scanning phased arrays) to five wavelengths (appropriate for focal plane arrays). In addition to the co- and cross-polarized patterns in the principal and diagonal planes, several of the data sets include spin-linear patterns in these planes.

Four of the antennas were fabricated on 30-mil (0.0762-cm) Duroid 5880, $\epsilon_r = 2.33$, and the other two were fabricated from beryllium copper shim stock using foam bridges that provided rigid support with air in the regions of highest electric field strength. The dimensions of the antennas are shown in Figure 2.2.1. Table 2.2.1 indicates the frequencies and pattern cuts for which data exist. A typical set of patterns is shown in Figure 2.2.2, which is for antenna 2 at 6 GHz. This example was chosen because it illustrates several of the characteristics to be discussed below, not because it represents the most desirable antenna performance. The definition of co- and cross-polarization for these data is Ludwig's third definition [2]. This definition is consistent with measurements performed by tilting the LTSA relative to the vertical axis of rotation of an azimuthal positioner (see Fig. 2.2.3). The angles γ_r and γ_t are noted on the patterns in Figure 2.2.2, and $\gamma_r = 0$ corresponds to H-plane, while $\gamma_r = 90$ corresponds to E-plane.

As is evident in the 45°-plane co- and cross-polarization patterns of Figure 2.2.2, the peaks of the cross-polarized signal in the forward hemisphere occur approximately at the nulls of copolarized signal, and vice versa. This trend has been observed consistently for the antennas that were tested. Also, the axial ratio in the diagonal plane usually has a local minimum near the -10 dB angle of the copolarized signal. Since the change of polarization from linear to elliptical over the radiation region may be a more serious problem in antenna applications than a simple rotation of the plane of polarization, the axial ratio has been identified as a key performance parameter for the LTSAs, and has been tabulated and plotted for all of the cases measured. Representative plots in Figure 2.2.4 show the measured 3-dB and 10-dB beamwidths and the smallest axial ratios observed in the diagonal plane (part b). Two axial ratio curves are plotted; one for the smallest axial ratio within the 3-dB-copolarized beamwidth, and one for the smallest ratio within the 10-dB-beamwidth. Beamwidths greater than 180° were considered to be meaningless for array applications, and are not plotted in Figure 2.1.4.

Since the antennas were not designed to be optimum for any particular frequency, the beamwidths of the antennas measured generally do not follow the familiar trends we have seen for well-designed LTSAs. Nevertheless, the larger antennas (e.g. numbers 4 and 6) do exhibit a general decrease of beamwidths as frequency increases. The minimum axial ratio within the 10-dB beamwidth, $AR_{10 \text{ dB}}$, is typically less than 5 dB, but the value for a particular antenna varies by several dB depending on the frequency of operation. The minimum axial ratio within the 3-dB beamwidth, $AR_{3 \text{ dB}}$, is usually a few dB greater than $AR_{10 \text{ dB}}$, but it is usually less than 10 dB. Therefore, most applications of the LTSA will be affected by their polarization properties, and more work on this critical area is needed.

2.3. *Effect of Cross-Polarized Radiation on the Directivity, and Gain of Single Element LTSAs*

In general, we can expand the radiation pattern from a feed antenna element in terms of spherical harmonic functions as follows [3]:

$$\bar{E}(r, \theta, \phi) = \frac{e^{-jk r}}{r} \left[E_\theta(\theta, \phi) \hat{\theta} + E_\phi(\theta, \phi) \hat{\phi} \right], \quad (2.3.1)$$

where

$$E_\theta(\theta, \phi) = \sum_{m=1}^N [A_m(\theta) \sin(m\phi) + B_m(\theta) \cos(m\phi)]$$

$$E_\phi(\theta, \phi) = \sum_{m=1}^N [C_m(\theta) \cos(m\phi) - D_m(\theta) \sin(m\phi)],$$

Here, $A_m(\theta)$, $B_m(\theta)$, $C_m(\theta)$, and $D_m(\theta)$ are complex functions of the wave index and the polar angle θ .

For most antennas used as reflector antenna feeds, the field is given to a very good approximation by the $m = 1$ terms in this expansion only, and most calculations of aperture efficiency, etc., for reflector antennas utilize this assumption. In this case, it is sufficient to characterize the full pattern at any angle in terms of the E- and H-plane patterns, co- and cross-polarized, as follows:

$$\hat{E}(r, \theta, \phi) = \frac{e^{-jkr}}{r} \left[\left\{ A(\theta) \sin \phi \hat{\theta} + C(\theta) \cos \phi \hat{\phi} \right\} + \left\{ B(\theta) \cos \phi \hat{\theta} - D(\theta) \sin \phi \hat{\phi} \right\} \right] \quad (2.3.2)$$

In this expression,

$$A(\theta) = F_E(\theta) \text{ is the E-plane co-pol pattern } (\phi = 90^\circ)$$

$$B(\theta) = F_H^X(\theta) \text{ is the H-plane cross-pol pattern } (\phi = 0^\circ)$$

$$C(\theta) = F_H(\theta) \text{ is the H-plane co-pol pattern } (\phi = 0^\circ)$$

$$D(\theta) = F_E^X(\theta) \text{ is the E-plane cross-pol pattern } (\phi = 90^\circ)$$

For instance, we can predict the D-plane ($\phi = 45^\circ$) patterns from these as follows: The co-polarized pattern is

$$F_D(\theta) = \frac{1}{2} [F_E(\theta) + F_H(\theta) + F_E^X(\theta) + F_H^X(\theta)], \quad (2.3.3a)$$

and the cross-polarized pattern, $F_D^X(\theta)$, is

$$F_D^X(\theta) = \frac{1}{2} [F_E(\theta) - F_H(\theta) + F_H^X(\theta) - F_E^X(\theta)] \quad (2.3.3b)$$

These expressions become particularly simple if the cross-polarized patterns in the E- and H-plane can be neglected. If, furthermore, the E- and H-plane patterns are identical (as they should be for symmetric illumination of the reflector), the D-plane cross-polarization will vanish. It was then interesting to investigate whether the cross-polarized pattern in the D-plane, which we measure for LTSA elements, could be explained as due to the E- and H-plane patterns being unsymmetric. Patterns for a typical element investigated in Y.S. Kim's thesis [4] are shown in Figure 2.3.1. In Figure 2.3.2, we compare the measured

D-plane patterns (co- and cross-pol.) with those derived from the measured E- and H-plane patterns, using Eq. (2.3.3). The main lobe of the co-polarized patterns is in good agreement, while the measured cross-polarized pattern has a peak which is about 7 dB higher than the predicted one. For the calculation, the phase of the E- and H-plane patterns was assumed to be the same, corresponding to coincident phase-centers for these planes. The possible conclusions from the comparison are that

1. Higher order terms than the $m = 1$ ones in Eq. (2.3.1) must be considered to describe the LTSA patterns fully.
2. The phase-centers may not be coincident, in which case the phase-terms for the patterns should be included in Eq. (2.3.3).

It is possible that a combination of the effects (1) and (2) occurs. We were later able to show, however, that condition (2), while it is likely to contribute, can not account for the entire discrepancy between measured and predicted D-plane patterns for several LTSA elements which include a dielectric. A range of physically reasonable phase-functions were used in attempting to fit the data. We have thus established that the patterns of many LTSA elements have a more complicated symmetry than those of most other types of feed elements, and may require higher order ($m > 1$) terms to describe the azimuthal variation. We may note that for the case of the particular air-dielectric LTSAs, to which the moment-method technique was applied (see section 2.4), Eq. (2.3.3) gives good agreement, at least for the main lobe region of the pattern. It is therefore possible that the higher order terms arise due to the dielectric loading of most LTSAs. The questions discussed in the above paragraph will be studied further.

For feeds with patterns which can be expressed in terms of $m = 1$ terms only in Eq. (2.3.1), it is also sufficient to use either the co-polarized E- and H-plane patterns, or the co- and cross-polarized D-plane patterns, in order to calculate the directivity of the element [5]. This is of course the standard procedure which is used in almost all such estimates, and which we had used initially for LTSAs. It had been noted that the directivity derived in this manner could differ from the measured absolute gain by anywhere from 3 to 5 dB, but we had not previously been able to identify the source of the extra loss with certainty. When measurements of both polarizations became available, we re-estimated the directivity for three different elements, with results as shown in Table 2.1.1. When the co- and cross-polarized patterns in the E-, H, and D-planes are used, we can derive the following expression for the directivity:

$$D = \frac{8}{\int_0^\pi [F_E(\theta)^2 + F_H(\theta)^2 + 2F_D(\theta)^2 + F_E^X(\theta)^2 + F_H^X(\theta)^2 + 2F_D^X(\theta)^2] \sin \theta d\theta} \quad (2.3.4)$$

Table 2.3.1 shows that the difference between measured gain and estimated directivity now is consistently about 1 dB or less. The gain was carefully measured by comparison with a standard gain horn. It can be concluded that the previously un-identified losses were mainly due to the integrated cross-polarized radiation. The table also gives the ratio of integrated cross-polarized power, to the total radiated power, in % (the "X-pol-ratio"),

calculated from:

$$XPR = \left[\int_0^\pi \{ F_E^X(\theta)^2 + F_H^X(\theta)^2 + 2F_D^X(\theta)^2 \} \sin \theta d\theta \right] \div \left[\int_0^\pi \{ F_E(\theta)^2 + F_H(\theta)^2 + 2F_D(\theta)^2 + F_E^X(\theta)^2 + F_H^X(\theta)^2 + 2F_D^X(\theta)^2 \} \sin \theta d\theta \right] \quad (2.3.5)$$

Some of the remaining difference between directivity and gain is undoubtedly due to ohmic losses, and it seems reasonable to put an upper limit of about 1 dB for these.

2.4 Moment Method Analysis of Linearly Tapered Slot Antennas

A report containing the results of the moment-method analysis of LTSA single elements was attached as Appendix I to the yearly report for Year 2. The program has been described in detail in an earlier report submitted to NASA. The report was written by Dr. Joakim Johansson of Chalmers University of Technology, and used as part of his Ph.D. thesis. A tape of the program will be delivered to NASA under separate cover. The program gave good agreement between measured and predicted radiation patterns.

In a more recent utilization of the data from this calculation, Johansson analyzed the variation of the phase of the far-field pattern with angle off axis. In all cases studied for which the main beam had a single peak, it was possible to fit these data to a function which indicated a unique phase-center for that particular plane. Generally, the E-plane phase-center was found to be located close to the aperture of the LTSA, while the H-plane phase-center was located closer to the apex. The D-plane phase-center was found to be at the exact half-way position between the E- and H-plane ones. Johansson later proved that this feature follows for any antenna which has a symmetric radiation pattern. For further details, we refer to Appendix I of the yearly report for Year 2.

The locations of the E-plane and H-plane phase centers are intuitively correct, if one considers the well-known fact that the E-plane beamwidths have a tendency to vary with the aperture size roughly the same way as for an aperture antenna, while the H-plane beamwidths vary with antenna length as those of a traveling-wave antenna.

Experimental studies of the phase of the radiated fields from an LTSA antenna would clearly be of further interest. The issue is at least partially related to the cross-polarization issue, as indicated in Sections 2.1 and 2.2.

A further utilization of the code developed by Johansson was begun under this program. That work has subsequently been completed and a thesis entitled "Endfire Tapered Slot Antennas and Their Polarization Characteristics," has been completed. One of the key findings of that work was the source of much of the cross-polarized radiation in the diagonal plane. The longitudinal currents flowing along the edges of the tapered slotline contribute most significantly to the cross-polarization. However, these currents also contribute to the copolarized E-plane pattern. Therefore, it appears unlikely that crosspolarized radiation can be eliminated. Nevertheless, some antenna designs have reduced crosspolarization, and the thesis contains several graphs depicting the polarization and beamwidth characteristics

of LTSAs as a function of antenna length, width, and opening angle. A copy of the thesis has been provided to the contract monitor under separate cover.

3.0 ANALYSIS AND EXPERIMENTAL STUDIES OF LTSA ARRAYS

The analytical studies of the LTSA arrays have proceeded along two paths. Section 3.1 describes a moment method analysis of infinite arrays of tapered slot antennas. A computer program called SPECASMNASA has been developed and delivered as a result of this effort. Section 3.2 discusses some experimental work and its interpretation. Some concluding remarks are offered in Section 3.3. Section 3.4 describes further experimental studies of the efficiency of TSA elements used in multi-beam systems in conjunction with reflector antennas.

3.1 Formulation of the Analysis

In this section, we outline the formulation of our Fourier integral method. This method cannot readily be extended to treat the finite dielectric substrate, but it is relatively straight-forward to formulate and can be modified to provide the key portion of a more general analysis that does treat finite dielectric substrates. The method is based on an integral equation for the electric currents on the conducting fins. The equation comes from enforcing the boundary condition that $\bar{E}_{tan} = 0$ on the conducting fins, where \bar{E}_{tan} is related to the fin current \bar{J} by a Green's function that incorporates the periodicity of the array. This allows us to restrict attention to a single unit cell.

Formulation of the problem proceeds as follows:

1. Determine the fields created by an infinite array of y -directed infinitesimal currents in front of a ground plane, as depicted in Figure 3.1.1. This proceeds by using TM_y fields generated by the potential function

$$\psi_y(x, y, z) = \frac{1}{2\pi} \sum_{n=-\infty}^{\infty} \int_{-\infty}^{\infty} [A_n(\alpha)e^{-j\beta_n z} + B_n(\alpha)e^{j\beta_n z}] e^{-jV_n y} \sin \alpha z d\alpha \quad (3.1)$$

where

$$\beta_n^2 + V_n^2 + \alpha^2 = k^2 \quad (3.2)$$

$$V_n = kv_o + n\frac{2\pi}{b}. \quad (3.3)$$

$$v_o = \sin \theta_o \sin \phi_o \quad (3.4)$$

and (θ_o, ϕ_o) is the scan direction.

The currents are phase such that a source at (y_o, z_o) in the $x = x_o$ plane is

$$J_y(x_o, y, z) = e^{-jkx_o x_o} e^{-jkv_o y_o} \delta(y - y_o) \delta(z - z_o). \quad (3.5)$$

For the purposes of this analysis, the current sources are considered to be sheets of current located on the planes $x = \text{constant}$.

- Determine the fields due to an infinite array of z -directed infinitesimal currents in front of a ground plane as depicted in Figure 3.1.2. For this we use TM_z fields generated by

$$\psi_z(x, y, z) = \frac{1}{2\pi} \sum_{n=-\infty}^{\infty} \int_0^{\infty} [C_n(\alpha)e^{-j\beta_n z} + D_n(\alpha)e^{j\beta_n z}] e^{-jV_n y} \cos \alpha z d\alpha \quad (3.6)$$

Again the current located at (y_o, z_o) on the plane $x = x_o$ is

$$J_z(x_o, y, z) = e^{-jk_u x_o} e^{-jk_v y_o} \delta(y - y_o) \delta(z - z_o) \quad (3.7)$$

The results of steps 1 and 2 are the Green's functions for the problem.

- The boundary condition that has not been satisfied in generating the Green's functions is

$$\bar{E}_{\text{tan}} = \bar{E}_{\text{tan}}^{\text{inc}} + \bar{E}_{\text{tan}}^{\text{scat}} = 0 \quad (3.8)$$

on the fins. This is written in component form as

$$-E_{yy}(x_o, y, z) - E_{yz}(x_o, y, z) = E_y^{\text{inc}}(x_o, y, z) \quad (3.9)$$

$$-E_{zy}(x_o, y, z) - E_{zz}(x_o, y, z) = E_z^{\text{inc}}(x_o, y, z) \quad (3.10)$$

where $E_{ij}(x_o, y, z)$ is the i component of the electric field due to the j component of current. The fields are evaluated on the fin at $x = x_o$.

- A moment method solution is generated by expanding the currents as

$$J_y(y, z) = \sum_{r=1}^R I_{yr} J_{yr}(y, z) \quad (3.11)$$

$$J_z(y, z) = \sum_{s=1}^S I_{zs} J_{zs}(y, z) \quad (3.12)$$

The equations (3.9) and (3.10) are enforced by multiplying by testing functions $W_{yp}(y, z)$ and $W_{zq}(y, z)$, respectively, and integrating over the fins. This leads to the matrix equation

$$\begin{bmatrix} Z_{yy} & \vdots & Z_{yz} \\ \dots & \vdots & \dots \\ Z_{zy} & \vdots & Z_{zz} \end{bmatrix} \begin{bmatrix} I_y \\ \dots \\ I_z \end{bmatrix} = \begin{bmatrix} E_y^{\text{inc}} \\ \dots \\ E_z^{\text{inc}} \end{bmatrix} \quad (3.13)$$

where the elements of the submatrices and vector are

$$Z_{yypr} = - \sum_{n=-\infty}^{\infty} \int_0^{\infty} K(\beta_n)(V_n^2 - k^2) \tilde{W}_{yp}^*(V_n, \alpha) \tilde{J}_{yr}(V_n, d) d\alpha \quad (3.14)$$

$$Z_{yzps} = - \sum_{n=-\infty}^{\infty} \int_0^{\infty} K(\beta_n)(\alpha V_n) \tilde{W}_{yp}^*(V_n, \alpha) \tilde{J}_{zs}(V_n, \alpha) d\alpha \quad (3.15)$$

$$Z_{zyqr} = - \sum_{n=-\infty}^{\infty} \int_0^{\infty} K(\beta_n)(\alpha V_n) \tilde{W}_{zq}^*(V_n, \alpha) \tilde{J}_{yr}(V_n, \alpha) d\alpha \quad (3.16)$$

$$Z_{zzqs} = - \sum_{n=-\infty}^{\infty} \int_0^{\infty} K(\beta_n)(\alpha^2 - k^2) \tilde{W}_{zq}^*(V_n, \alpha) \tilde{J}_{zs}(V_n, \alpha) d\alpha \quad (3.17)$$

$$E_{yp}^{inc} = \int_{fin} \int E_y^{inc}(x_o, y, z) W_{yp}(y, z) dy dz \quad (3.18)$$

$$E_{zq}^{inc} = \int_{fin} \int E_z^{inc}(x_o, y, z) W_{zq}(y, z) dy dz \quad (3.19)$$

$$K(\beta_n) = \frac{a}{j4\pi\omega\epsilon_o b} \frac{\sin \beta_n a}{\beta_n a} \frac{1}{\cos k u_o a - \cos \beta_n a} \quad (3.20)$$

$$u_o = \sin \theta_o \cos \phi_o \quad (3.21)$$

and I_y, I_z contain the unknown expansion coefficients in (3.11) and (3.12). The functions with tilde are Fourier transforms of the respective expansion and testing functions, defined as follows:

$$\left\{ \begin{array}{l} \tilde{J}_{yr} \\ \tilde{W}_{yp} \end{array} \right\} = j2 \int_0^{\infty} \left\{ \begin{array}{l} J_{yr}(y, z) \\ W_{yp}(y, z) \end{array} \right\} e^{jV_n y} \sin \alpha z dy dz \quad (3.22)$$

$$\left\{ \begin{array}{l} \tilde{J}_{zs} \\ \tilde{W}_{zq} \end{array} \right\} = 2 \int_0^{\infty} \left\{ \begin{array}{l} J_{zs}(y, z) \\ W_{zq}(y, z) \end{array} \right\} e^{jV_n y} \cos \alpha z dy dz \quad (3.23)$$

and the asterisk denotes complex conjugate. (All expansion and testing functions are assumed to be real.)

For our solution, the expansion and testing functions for each component were taken to be the same (Galerkin) and the functions were of piecewise sinusoidal roof-top form,

$$J_{yr}(y, z) = \frac{1}{w_r} \frac{\sin k_e(h_r - |y - y_r|)}{\sin k_e h_r} \quad \begin{array}{l} |y - y_r| \leq h_r \\ |z - z_r| \leq \frac{w_r}{2} \end{array} \quad (3.24)$$

$$J_{zs}(y, z) = \frac{1}{w_s} \frac{\sin k_e(h_s - |z - z_s|)}{\sin k_e h_s} \quad \begin{array}{l} |z - z_s| \leq h_s \\ |y - y_s| \leq \frac{w_s}{2} \end{array} \quad (3.25)$$

From these,

$$\begin{aligned} \bar{J}_{yr}(V_n, \alpha) &= \frac{j8k_e}{w_r(k_e^2 - V_n^2) \sin k_e h_r} e^{jV_n y_r} [\cos V_n h_r - \cos k_e h_r] \\ &\cdot \frac{\sin \alpha z_r \sin \alpha \frac{w_r}{2}}{\alpha}, \quad k_e^2 \neq V_n^2 \end{aligned} \quad (3.26)$$

$$\begin{aligned} \bar{J}_{zs}(V_n, \alpha) &= \frac{8k_e}{w_s V_n \sin k_e h_s} e^{jV_n y_s} \sin V_n \frac{w_s}{2} \\ &\cdot \frac{\cos \alpha z_s [\cos \alpha h_s - \cos k_e h_s]}{(k_e^2 - \alpha^2)}, \quad k_e^2 \neq \alpha^2 \end{aligned} \quad (3.27)$$

(The functions are not normally needed at the excluded values $V_n^2 = k_e^2$ and $\alpha^2 = k_e^2$, but if necessary they can be found easily by evaluating the integrals in (3.22) and (3.23) for these special values.)

A computer program has been written to evaluate (3.14)–(3.17). A description of the program is presented in Appendix A and its inputs and outputs along with a sample problem are presented in Appendix B. The integrals are evaluated by an adaptive quadrature formula with the upper limit determined by the lesser of (i) convergence of the integral or (ii) reaching a user set limit, typically $\alpha \leq 150k_o$. The summation on n is truncated at a user specified limit that must be determined by performing convergence checks. Typically, $|n| \leq 15$.

The straight-forward approach described in the preceding paragraph was found to be computationally unacceptable due to CPU times that exceeded 20 hours on a microVAX 2000 for problems of small to moderate size. The times can be reduced by evaluating the asymptotic forms of the integrals involved in (3.14)–(3.17), and adding these values to the integrals with the asymptotic forms subtracted, that is

$$\begin{aligned} I &= \int f(\alpha) d\alpha = \int [f(\alpha) - f_a(\alpha)] d\alpha \\ &+ \int f_a(\alpha) d\alpha \end{aligned} \quad (3.28)$$

where $f_a(\alpha)$ is the asymptotic form of $f(\alpha)$ and the last integral can be evaluated analytically, or numerically and stored for later use in a look-up table. This scheme produced a tenfold reduction in CPU time, and moderate size problems can now be solved in a few hours per data point. Further reduction of these times should be possible, but this has not been attempted during this contract.

No attempt has been made to reduce matrix solution times because this time is negligible compared to the fill time.

3.2 Numerical Results

In this section, we present the results of several computations that were performed to test the computer program and to illustrate the types of problems that can be solved. Each

of the examples presented here has been compared to experimental or other computational results.

3.2.1 Dipole Array

Stark [6] has solved the problem of an infinite array of strip dipoles parallel to a ground plane. For narrow strips, his geometry will be electrically equivalent to strips in the $y - z$ plane (see Fig. 3.2.1). In Figures 3.2.2–3.2.5, our data, computed with one expansion mode for the dominant current, is plotted on copies of Stark's curves, also computed with one expansion mode. The agreement for these simple cases is excellent, verifying our formulation method, which must be completely different from Stark's in order to treat fins in $x = \text{constant}$ planes.

3.2.2 Monopole Array

Fenn [7] has solved the problem of an infinite array of monopoles. We have computed the input impedance of an array of narrow strip monopoles and compared our results to those of Fenn for small diameter monopoles. The results in Figure 3.2.6 display agreement to within the accuracy with which we can transcribe Fenn's data.

3.2.3 Balun-Fed Dipole Array

Schumann, et al, [8] have analyzed an array of wire dipoles over a ground plane with a two-wire balun. This configuration is known to possess a scan blindness for an appropriate choice of parameters, and we have replicated their results by using a strip approximation to their geometry. Our results have a slightly different absolute value for input impedance (particularly reactance), but the trends are similar and the blindness near 40° is correctly predicted (Fig. 3.2.7). The discrepancy in reactance is probably associated with the differences of the feed region reactance for the wire segment model of [8], and our strip model. Removing the balun structure to yield a simple dipole over ground (similar to Stark's array), our method obtained an input impedance of $75 - j109$ compared to $75 - j75$ obtained in [8]. Adjusting the data by the difference of these values would bring the two methods into closer agreement.

3.2.4 Strip-Loop Array

We have built and tested in a waveguide simulator the antenna array depicted in Figure 3.2.8. This antenna has many of the features of the CWSA antenna that is discussed in the next subsection, but the strips are narrow enough that only one component of current needs to be considered along the strips, except near the feed and corners. The dimensions are in Figure 3.2.9.

A comparison of measured and computed input impedance in the simulator is shown in Figure 3.2.10. The agreement for resistance is excellent above 4 GHz. The reactance shows a negative shift approximately equal to a series capacitance of 0.24 pf. The configuration of the simulator is depicted in Figure 3.2.11. The SSMA coaxial feed probe is soldered to a tab on one half of the strip-loop antenna, which is located in the center of a half-height waveguide. It is likely that this feed junction has parasitic reactances that are not modeled

by a numerical method.

After completing this simulator experiment, we discovered that the termination in the waveguide was not well matched below 4 GHz. Therefore, the measurements in that frequency range are not reliable.

3.2.5 CWSA array

An array of CWSA antennas has been measured using the waveguide simulator described in section 3.2.4. The dimensions of the antenna are given in Figure 3.2.12 and a Smith chart comparison of measured and calculated results is presented in Figure 3.2.13. For this comparison a reactance of $j62$ ohms was added to the computed results. This value represents the average difference between the measured and calculated reactances. With this correction for excess feed reactance, the agreement is very good.

These computations utilized $22J_y$ modes and $26J_z$ modes to model the antenna and required approximately 16 hours of CPU time per data point. From this, it is clear that further effort at reducing computation time is needed. We believe that a reduction of 5 to 10 times should be possible by changing the quadrature integration scheme to one that allows the time-consuming portions of the integrands to be computed and stored for use within the matrix filling loops. However, a considerable amount of storage will be required and the computer must be capable of allocating this to the program without paging to the disk.

3.3 Remarks

The formulation and computer program described in this section can be used to analyze a variety of antenna arrays comprised of metallic sheets arranged in a "fin" geometry. This formulation is valid for homogeneous dielectrics, so it cannot explicitly account for the thin dielectric substrates that frequently are used to support the antennas. However, for thin substrates, the dielectric loading may not be as dominant in determining array performance as the metallic fins. If this is the case for an antenna under study, the dielectric loading may cause only a small shift in frequency or blindness angle without altering the basic nature of the antenna's performance. Further work is needed to determine the range of parameters over which this is valid.

For antennas that require explicit treatment of the finite substrate, the formulation described in section 3.1 of the second yearly technical report should be used. Our work on this formulation will continue under support from an industrial sponsor, but considerable improvement in computation times will be required to permit accurate analysis of antennas supported by dielectric substrates. As noted at the beginning of section 3.1, the Fourier integral method can be used to obtain a major portion of the more general method. In particular, all of the fin-to-fin interactions are obtained from (3.14)–(3.17) by replacing the alpha integral with a summation where $\alpha = n\frac{\pi}{d}$, n being an integer and d the depth of the element.

The antennas treated so far have metallic boundaries that coincide with the rectangular coordinate system. In order to treat tapered structures, we could use a step-wise

approximation. However, we plan to extend the present analysis by including new basis functions for the current. Each mode will be piecewise sinusoidal in the direction of current flow and uniform in the cross-flow direction. It appears that we can incorporate these modes without major changes in the analysis, but computation times are expected to increase somewhat for these modes because they have both y and z components.

3.4. Continued Experimental Study of LTSA Arrays

The material in this section summarizes results with respect to LTSA arrays which were described in detail in the Ph.D. thesis of Young-Sik Kim [4]. This thesis has been transmitted to NASA LaRC with an earlier report. A parametric study was performed of 5×5 element LTSA arrays fed from a waveguide block containing fin-line transitions. Parameters which were varied include the opening angle, the length, and the element spacing. New combinations of these parameters which yielded symmetric beams were identified. Arrays with element spacing 2.5λ behaved closer to the single elements, but still showed noticeable effects due to mutual coupling. Arrays with 1.5λ spacing generally showed wider beamwidths at the -10 dB level than for single elements, whereas the 2.5λ spacing arrays showed a slight narrowing instead. Radiation patterns were quite similar from element to element in an array, with small asymmetries detectable at the edge of the array. Large forward traveling wave coupling and essentially negligible backward coupling were measured in a special test fixture.

A major finding was that the element gain can approach the maximum theoretical element gain in a large array, i.e.

$$G_{max} = 4\pi d^2 / \lambda^2 \quad (3.4.1)$$

where d is the element to element spacing. This was true for the arrays with element spacing close to 1.5λ , not for those with 2.5λ spacing. Figure 3.4.1 shows two examples of the measured gain versus frequency, covering the entire K_a -band. The directivity in these curves was calculated from co-polarized patterns only, and is higher than the measured gain by 2 to 3 dB. This result is thus very similar to what was found for single elements, as discussed in section 2.2 in this report.

The peaks of the cross-polarized pattern in the D-plane were found to be of similar magnitude for both array elements and single elements. The pattern symmetry is probably more complicated in the array case, though, judging from the results of applying Eq. (2.4.3) to the E- and H-plane patterns. Figure 3.4.2 shows the predicted and measured D-plane patterns for one such case. Note that neither the co-polarized nor the cross-polarized patterns agree well with the prediction, whereas for single elements, the co-polarized pattern agreed well in the main beam region. The array results shown in Figure 3.4.2 are for an element spacing of 1.5λ , whereas the 2.5λ spacing array gave a co-polarized D-plane beam much more in agreement with Eq. (2.4.3). Again, the larger spacing array thus behaved closer to a single element, as might be expected.

In order to evaluate the usefulness of LTSA arrays as feed arrays for multi-beam systems, it is important to estimate the aperture efficiency which would be obtained in

such a system. The studies related above gave us valuable clues to how such an estimate should be obtained. It was clear that this estimate would have to take into account the cross-polarized radiation in all planes for which measurements were available. Three different expressions were derived for the aperture efficiency:

$$\epsilon_{ap} = \frac{\cot^2(\theta^*/2)}{2} \left[\left| \int_0^{\theta^*} \{F_E(\theta) + F_H(\theta) + 2F_D(\theta)\} \tan(\theta/2) d\theta \right|^2 + \left| \int_0^{\theta^*} \{F_E^X(\theta) + F_H^X(\theta) + 2F_D^X(\theta)\} \tan(\theta/2) d\theta \right|^2 \right] \div \quad (3.4.2)$$

$$\left[\int_0^\pi \{F_E(\theta)^2 + F_H(\theta)^2 + 2F_D(\theta)^2 + F_E^X(\theta)^2 + F_H^X(\theta)^2 + 2F_D^X(\theta)^2\} \sin \theta d\theta \right]$$

$$\epsilon_{ap} = \frac{\text{Gain}}{4} \cot^2(\theta^*/2) \left[\left| \int_0^{\theta^*} \{F_E(\theta) + F_H(\theta)\} \tan(\theta/2) d\theta \right|^2 + \left| \int_0^{\theta^*} \{F_E^X(\theta) + F_H^X(\theta)\} \tan(\theta/2) d\theta \right|^2 \right] \quad (3.4.3)$$

$$\epsilon_{ap} = 2 \cot^2(\theta^*/2) \cdot \left| \int_0^{\theta^*} [F_E(\theta) + F_H(\theta)] \tan(\theta/2) d\theta \right|^2 \div \left[\int_0^{\theta_e} F_E(\theta)^2 \sin \theta d\theta + \int_{\theta_e}^\pi \sigma^2 \sin \theta d\theta + \int_0^{\theta_h} F_H(\theta)^2 \sin \theta d\theta + \int_{\theta_h}^\pi \sigma^2 \sin \theta d\theta \right], \quad (3.4.4)$$

The first equation represents an integration over the E-, H-, and D-planes, similar to the calculation of the directivity in section 2.3. The second expression uses the measured gain as an estimate for the denominator of the aperture efficiency integral. The third expression makes use of the measured gain in a slightly different manner, which allows us to estimate the aperture efficiency from the measured gain plus the co-polarized E- and H-plane patterns. In this case an equivalent pattern was introduced, which had the same main beam patterns as the experimentally measured ones, but with a constant side-lobe level (σ) which was adjusted until the calculated directivity equalled the measured gain. The angles θ_e and θ_h are defined such that $F_E(\theta_e) = F_H(\theta_h) = \sigma$. The aperture efficiency was then found for this equivalent pattern. Table 3.4.1 gives the results of aperture efficiency calculations for four arrays using both methods. It is predictable that an aperture efficiency estimate based on co-polarized patterns in the E- and H-plane patterns only (the traditional method) would be quite inaccurate due to the fairly high fraction of power in cross-polarized lobes. Table 3.4.1 compares the estimates from the above three equations, as well as the traditional method, using data from four arrays. Generally, the agreement between the three expressions is quite good. As expected, the estimate based on the traditional method (co-polarized patterns only) over-estimates the aperture efficiency. The best of the four arrays has an aperture efficiency of about 45%. The investigation shows that one can estimate the aperture efficiency with any of the three above methods

with good confidence about the results. We have later verified the aperture efficiency by direct comparison between a TSA feed and a waveguide feed, in a prime-focus paraboloid (in work on another contract). Also, values of about 60% have been obtained in this later work. While we do not have a complete model of the LTSA array, so far, we have developed an experimental procedure from which the aperture efficiency can thus be predicted for feed elements which have large cross-polarized components in their radiation patterns. The main factor in the aperture efficiency which still needs to be taken into account is the phase-efficiency. This is so far unknown due to the lack of phase-measurements, but is unlikely to decrease the total aperture efficiency by more than 5 or 10%. We thus feel that the investigation has demonstrated that LTSA feed arrays should yield aperture efficiencies in systems fully comparable with those of waveguide feeds, corrugated horns excluded. It should be re-iterated that the LTSA array achieves this efficiency at an element spacing which is about half of that of a waveguide array, with the spacing of corrugated horns being even larger than for waveguide horns.

4. DESIGN OF A MIXER SUITABLE FOR USE WITH LTSA ARRAYS

A preliminary mixer design for a balanced mixer suitable for use with LTSA arrays has been developed and tested. The mixer employs LO injection from the "back" side of the substrate, and microstrip technology. The substrate is 10 mil thick Duroid 6010.5, with a permittivity of 10.5. The mixer has so far been tested by feeding the signal via a fin-line transition and also from a Vivaldi antenna. The waveguide port available in the fin-line version vastly facilitates making conversion loss measurements by direct power measurements. The general layout is shown in Figure 4.1, and Figure 4.2 shows close-ups of two of the mixer patterns tested.

The IF power is prevented from leaking out the LO port by a one section bandpass filter. At the design frequency of 35 GHz, this filter has a minimum insertion loss of 5 dB, and return loss better than 10 dB. A three-section filter was also designed, which has a much sharper bandpass-characteristic. The filters were designed on Super-compact and the AUTOCAD system was used for cutting the rubyolith mask. Photoresist was spun onto the substrate, and exposed and etched using standard procedures. It may be of interest to NASA that a re-design of the one-section filter using a 10 mil quartz substrate gave an insertion loss of only 0.5 dB. (Courtesy of Russel Bardsley, now at the G.E. Company.)

Two low-pass filters were tested, one 3-section filter with a cut-off frequency of about 2 GHz, and a 5-section one with a higher cut-off-frequency, 20 GHz. The latter one was used in the mixer tests, since it was much more compact, and allowed use of a wider range of IF-frequencies.

Figure 4.3 gives the best conversion loss obtained with a minimum loss of about 10 dB. Two HP K_u -band diodes were silver-epoxied into the circuit. For these measurements the LO frequency was held constant and the signal frequency varied. The conversion loss saturated at an LO power level of about 10 dBm. This corresponds to a power of about 4 dBm at the mixer, if one takes into account the loss of the microstrip and the bandpass filter.

The measured isolation between the LO and IF ports was better than 35 dB, and the isolation from the LO port to the signal port was better than 26 dB, across the waveguide band.

IF amplifiers with a passband from 0 to 2 GHz were incorporated on the substrate, and the noise performance of the mixer tested. The noise figure is shown in Figure 4.4 and a radiation pattern of a Vivaldi antenna integrated with the mixer, is given in Figure 4.5.

The mixer could easily be used with a power splitter for the LO feed, in order to feed a pair of LTSA elements from the same LO source, without leading to any routing problems for the LO and IF transmission lines. If it were desired to have one LO source feed more than two elements, with a power-splitter on the same substrate, then crossings of the different types of lines would occur, and some more complicated scheme must be used. We looked into using co-planar waveguide lines on one side of the substrate, and microstrip on the other side. It appears feasible to design a crossing of these lines, but further work on these ideas was discontinued in favor of finishing a mixer design in time for the designated end of this effort in August, 1988. We conclude that we reached our goal of developing a preliminary mixer design, and that this design appears to be quite close to the best performance which can be expected from the K_u -band diodes used.

5. CONCLUSIONS

5.1 *Analytical Modeling*

A moment method analysis of infinite arrays of endfire slot antennas has been developed. Computations performed with the computer program are in excellent agreement with published results for dipole and monopole arrays. Computations for more complicated structures are in good agreement with waveguide simulator measurements, except for a reactive shift that is believed to be caused by the simplified delta gap model of the feed region. The work performed under this contract has formed the basis for a continuing effort supported by a major electronics company and further improvements and extensions of the analysis capabilities are expected. In particular, further reduction of the somewhat excessive computation times is expected in the near future.

5.2 *Experimental Modeling*

The empirical studies of LTSA single elements and arrays have led to a set of design rules which can be used to predict a design of an LTSA (Vivaldi or CWSA) element for a particular application. At this stage, the best procedure involves choosing an initial design, which is measured, whereupon the shape, dielectric, etc. are changed until the desired performance is obtained. Useful data have been summarized in publication [4] (see section 6.2). A procedure for evaluating the directivity of LTSA elements from measured patterns (co- and cross-polarized) in the E, D, and H-planes has been developed. With this method good agreement is obtained between estimated directivity and measured gain for the first time. The aperture efficiency for an LTSA element, when used in a reflector system, can be estimated from the same set of patterns. Later work on another contract has shown that the estimated aperture efficiency agrees well with the measured efficiency

in an $f/D = 1$ paraboloid. Values of about 60% can be obtained with Vivaldi elements, and it can be concluded that TSA elements thus can be used in multi-beam systems, with about the same efficiency as typical waveguide feeds, but at a spacing of about one half that of waveguide feeds. Phased arrays with high efficiency for spatial power combining have also been demonstrated in ongoing work for JPL.

6. PUBLICATIONS AND THESES ON THE BASIS OF THE CONTRACT

6.1. *Theses*

A Ph.D. thesis at UMass has been completed based on work supported by the LaRC contract:

Young-Sik Kim: "Linearly Tapered Slot Antenna Arrays for Multibeam Systems," Defense passed in March, 1988, degree granted in May, 1988. Copies of Dr. Kim's thesis have been submitted with monthly report 2-8, April 1988.

A Ph.D. thesis at Chalmers University has been completed, which was partially supported by the contract:

Joakim F. Johansson: "Tapered Slot Antennas and Focal Plane Imaging Systems", Defended in September, 1988, at Chalmers University of Technology, Gothenburg, Sweden. Two chapters of Dr. Johansson's thesis are included as Appendices I and II with the second yearly report.

Two M.Sc. theses have been partially supported by the contract:

"Endfire Tapered Slot Antennas and Their Polarization Characteristics," Ajay Asija, August 1989.

"Design, Fabrication and Analysis of an Integrated K_A -Band Receiver Front End," Frederick R. Bardsley III, May 1989.

6.2 *Publications*

Publications which have appeared in journals

- [1] "Analysis of the Transverse Electromagnetic Mode Linearly Tapered Slot Antenna", R. Janaswamy, D.H. Schaubert, and D.M. Pozar, *Radio Science*, Volume 21, 797-804, September-October 1986.
- [2] "A New Integrated Slot Element Feed Array for Multibeam Systems", K. Sigfrid Yngvesson, Joakim F. Johansson, and E.L. Kollberg, *IEEE Trans. Antennas Propagat.*, AP-34, 1372-1376, Nov. 1986. (Based on related work on the earlier NASA grant, and on cooperative work with the Chalmers University group)
- [3] "Realizable Feed-Element Patterns and Optimum Aperture Efficiency in Multi-Beam Antenna Systems", by K.S. Yngvesson, J.F. Johansson, Y. Rahmat-Samii, and Y.S. Kim, *IEEE Trans. Antennas Propagat.*, AP-36, 1637-1641 (Nov. 1988).

- [4] "The Tapered Slot Antenna - A New Integrated Element for Millimeter Wave Applications", by K.S. Yngvesson, T.L. Korzeniowski, Y.S. Kim, E.L. Kollberg, and J. F. Johansson, Invited paper, *IEEE Trans. Microw. Theory Techn.*, MTT-37, 365-374 (Feb. 1989).

Conference Publications:

- [5] "Millimeter/Submillimeter Imaging With Planar Focal Plane Arrays", K.S. Yngvesson and J.F. Johansson, The National AP-S/URSI Meeting, Boulder, Colorado, (Commission J), January 1987.
- [6] "Aperture Efficiency of LTSA Focal Plane Arrays for Millimeter Waves", by Y.S. Kim and K.S. Yngvesson, *12th Intern Conf. IR MM Waves*, Orlando, FLA, Dec. 1987, p.220.
- [7] "Tapered Slot Antenna Focal Plane Arrays for Submillimeter Waves", by K.S. Yngvesson, Y.S. Kim, J.X. Yang, J.F. Johansson, and E.L. Kollberg, *Fourth Intern Conf. Infrared Physics*, Zurich, Switzerland, August, 1988.
- [8] "A Moment Method Analysis of Tapered Slot Antennas" by J.F. Johansson, presented at the *Nordic Antenna Symposium "Antenn 88"*, May, 1988.

Conference Papers supported in part

- [9] Daniel H. Schaubert, "Radiation Characteristics of Linearly Tapered Slot Antennas," 1989 IEEE Antennas and Propagation Symposium, 1324-1327, San Jose, June 1989.
- [10] Joakim F. Johansson, "A Moment Method Analysis of Linearly Tapered Slot Antennas," 1989 IEEE Antennas and Propagation Symposium, 383-386, San Jose, June 1989.
- [11] D.H. Schaubert, "Endfire Tapered Slot Antenna Characteristics," Sixth International Conference on Antennas and Propagation, 1.432-1.436, University of Warwick, Coventry, April 1989.
- [12] Joakim F. Johansson, "Stein's Limit for Multi-Beam Reflector Systems," 1989 IEEE Antennas and Propagation Symposium, San Jose, June, 1989.

Publications submitted to journals

- [13] Y.S. Kim and K.S. Yngvesson, "Characterization of Reflector Antenna Feeds and Feed Arrays with High Cross-Polarization in the D-plane," submitted to *IEEE Trans. Ant. Prop.*, 1989.

7. REFERENCES

- [1] Zucker, F.J., in Jasik, H. (Editor), "Antenna Engineering Handbook", Chapter 16, McGraw-Hill, New York (1961).
- [2] A.C. Ludwig, "The Definition of Cross-Polarization", *IEEE Trans. Ant. Prop.*, AP-21, 116-119, January 1973.

- [3] W.V.T. Rusch, and P.D. Potter, "Analysis of Reflector Antennas," Academic Press, New York, 1970, pp. 70-80.
- [4] Young-Sik Kim: "Linearly Tapered Slot Antenna Arrays for Multibeam Systems," Ph.D. Thesis, Univ. of Mass., May 1988.
- [5] P.-S. Kildal, "Factorization of the Feed Efficiency of Paraboloids and Cassegrain Antennas," *IEEE Trans. Antennas Propagat.*, AP-33, 903-908 (1985)
- [6] L. Stark, "Radiation Impedance of a Dipole in an Infinite Planar Phased Array," *Radio Science*, vol. 1, no. 3, 361-377, March 1966.
- [7] A. Fenn, "Theoretical and Experimental Study of Monopole Phased Array Antennas," *IEEE Trans. Ant. Propagat.*, vol. AP-33, no. 10, 1118-1126, Oct. 1985.
- [8] H.K. Schuman, D.R. Pflug and L.D. Thompson, "Infinite Planar Arrays of Arbitrarily Bent Thin Wire Radiators," *IEEE Trans. Ant. Propagat.*, vol. AP-32, 364-377, April 1984.

8. TABLES

Table 2.1.1. Gain, Directivity, X-Pol Ratio, and Peak of X-Pol Pattern for Single Element LTSAs

LTSA Description (All Substr. 5 mil thick)	Directivity (dB)		Measured Gain (dB)	XPR (%) (eq. (2.2.5.))	Peak of X-Pol, D-plane (dB)
	From Co-Pol E-/H-patt.	From Eq. (2.2.4.)			
$\epsilon_r = 2.2$ $2\gamma = 11.2^\circ$ $L/\lambda = 10$	20.15	17.1	16.7	33.1	-4.9
$\epsilon_r = 3.5$ $2\gamma = 5.6^\circ$ $L/\lambda = 10$	17.4	15.3	14.2	21.7	-9.4
$\epsilon_r = 3.5$ $2\gamma = 11.2^\circ$ $L/\lambda = 6$	16.9	14.9	13.6	27.1	-5.7

Table 2.2.1. Dimension of Some LTSA Single Elements Measured

30-Mil Duroid Antennas					
Antenna	ϵ_r	A (cm)	H (cm)	L (cm)	F (mils)
1	2.2	2.5	3.0	4.0	12.5
2	2.2	2.5	3.0	8.0	12.5
3	2.2	2.5	3.0	15.0	12.5
4	2.2	5.0	6.0	15.0	12.5

Air Antennas			
Antenna	L (cm)	W (cm)	F (cm)
5	6.0	3.0	0.04
6	15.0	3.0	0.04

**Table 3.4.1. Aperture Efficiency of a Reflector System
with 5×5 LTSA Array (for center beam)**

Element Description (all substrates 5mil Kapton)	Aperture Efficiency (%)			
	Eq. (3.4.2.)	Eq. (3.4.3.)	Eq. (3.4.4.)	Co-Pol. only E-, H- planes (Conventional)
$2\gamma = 11.2^\circ$ $d/\lambda = 2.5$ $L/\lambda = 6$	35.2	34.6	34.7	57.3
$\gamma = 7.5^\circ$ $d/\lambda = 2.5$ $L/\lambda = 7$	37.2	24.5	24.4	55.8
$2\gamma = 11.2^\circ$ $d/\lambda = 1.5$ $L/\lambda = 6$	39.3	36.8	36.6	57.2
$2\gamma = 7.5^\circ$ $d/\lambda = 1.5$ $L/\lambda = 6$	44.6	45.3	45.2	70

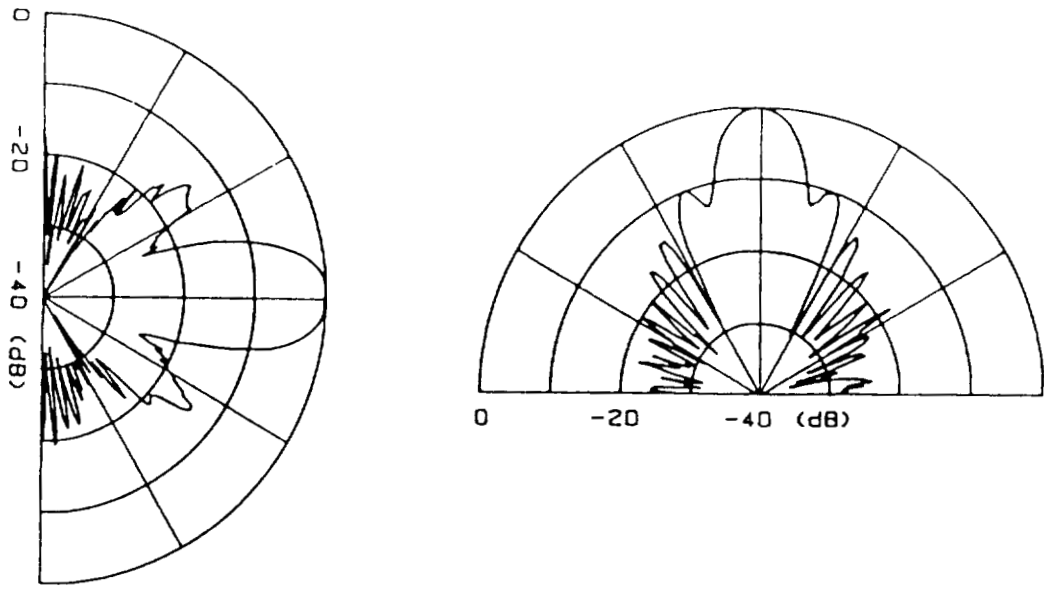
9. Figures

9.1 Figure Captions

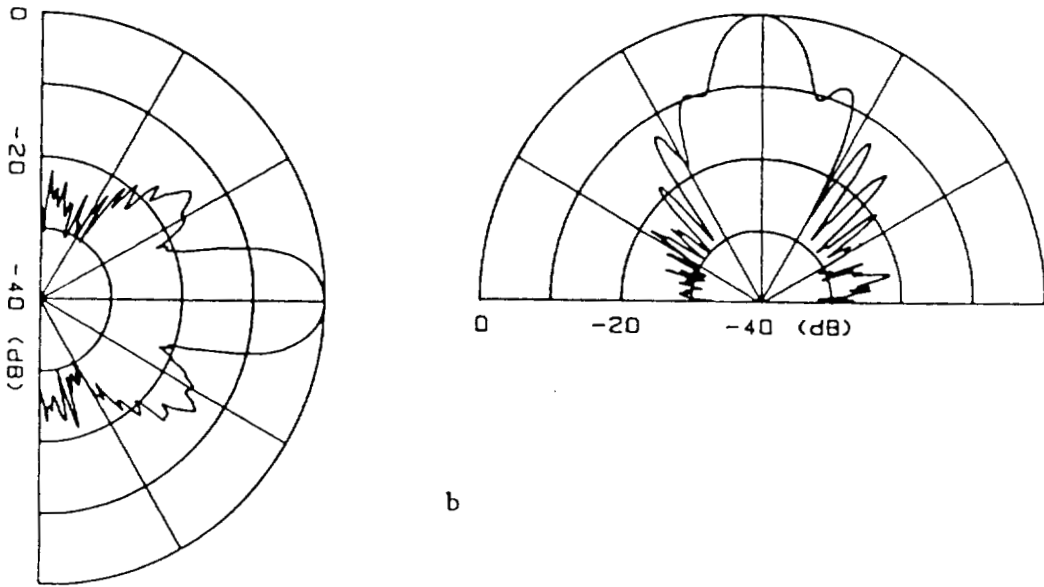
- Figure 2.1.1. A comparison of single element LTSA radiation patterns obtained by using a) a split waveguide block feed and b) a detector diode soldered to the narrow portion of the slot.
- Figure 2.1.2. Directivity of single element LTSA's versus normalized length for four values of normalized dielectric thickness. Dielectric is Kapton ($\epsilon_r = 3.5$) and $2\gamma = 11.2^\circ$.
- Figure 2.1.3. 10 dB beam efficiency versus normalized length for the same antennas as in Figure 2.1.2.
- Figure 2.1.4. 3 dB beam width versus L/λ_o for the same antennas as in Figure 2.1.2. (a) E-plane (b) H-plane.
- Figure 2.1.5. 10 dB beamwidth versus L/λ_o for the same antennas as in Figure 2.1.2. (a) E-plane (b) H-plane.
- Figure 2.1.6. Directivity versus normalized length for LTSA single elements with the opening angle (2γ) as a parameter. Substrate: 5 mil (0.13 mm) Kapton.
- Figure 2.1.7. Radiation patterns of LTSA single elements on three different substrates, all of 5 mil (0.13 mm) thickness: (1) Kapton ($\epsilon_r = 3.5$), (2) Duroid ($\epsilon_r = 2.2$), (3) Duroid 6010 ($\epsilon_r = 10.2$), $2\gamma = 11.2^\circ$ (a) E-plane (b) H-plane.
- Figure 2.1.8. Directivity versus normalized length for the same LTSA's as in Figure 2.1.7.
- Figure 2.2.1. Antenna geometries and dimensions.
- Figure 2.2.2. Definitions of antenna orientation (a) and transmitted field (b) for radiation pattern measurements.
- Figure 2.2.3. Radiation patterns of antenna number 4 at 7 GHz.
- Figure 2.2.4. Beamwidths and axial ratios of antenna 4 (a) principal plane beamwidths, (b) diagonal plane beamwidths and axial ratios.
- Figure 2.3.1. Co- and cross-polarized radiation patterns of the single element LTSA with $2\gamma = 11.2^\circ$ and $L/\lambda = 6$ on a 0.0127 cm Kapton substrate at 35 GHz (— co-pol, = · = x-pol)
- Figure 2.3.2. Comparison of calculated and measured patterns in the D-plane of a single LTSA.
- Figure 3.1.1. Array of y -directed currents for Green's function.

- Figure 3.1.2. Array of z-directed currents for Green's function.
- Figure 3.2.1. Strip dipole array configuration.
- Figure 3.2.2. Resistance versus scan of 0.5-wavelength dipoles 0.25-wavelength above ground plane. $a = b = 0.5$ wavelength.
- Figure 3.2.3. Reactance versus scan of 0.5-wavelength dipoles 0.25-wavelength above ground plane. $a = b = 0.5$ wavelength.
- Figure 3.2.4. Resistance versus scan of 0.5-wavelength dipoles 0.25-wavelength above ground plane. $a = b = 0.6$ wavelength.
- Figure 3.2.5. Reactance versus scan of 0.5-wavelength dipoles 0.25-wavelength above ground plane. $a = b = 0.6$ wavelength.
- Figure 3.2.6. Comparison of calculations with SPECASMNASA to those of Fenn [7]. Fenn's data points coincide nearly perfectly with the points plotted for UMass.
- Figure 3.2.7. Dipole over ground with two-wire balun. UMass data for case B plotted on graph from [8].
- Figure 3.2.8. Strip-loop antenna array used as test case of computer program.
- Figure 3.2.9. Dimensions of strip-loop antenna.
- Figure 3.2.10. Measured and calculated impedance of strip-loop antenna in waveguide simulator. Square boxes of reactance plot are raw computations and X_s are obtained by removing an equivalent capacitance of 0.24 pf.
- Figure 3.2.11. Waveguide simulator for strip-loop array.
- Figure 3.2.12. Dimensions of CWSA element.
- Figure 3.2.13. Measured and calculated impedance of CWSA array. Calculated data are adjusted for excess capacitive reactance of 62 ohms.
- Figure 3.4.1. Comparison of the measured gain, G_{max} , and directivity of the 5×5 array center element with $d/\lambda = 1.5$: (a) $2\gamma = 7.5^\circ$ and $L/\lambda = 10$, and (b) $2\gamma = 11.2^\circ$ and $L/\lambda = 7.6$.
- Figure 3.4.2. Comparison of calculated and measured patterns in the D-plane of the center element in an LTSA array with $d/\lambda = 1.5$.
- Figure 4.1. General layout of the balanced mixer.
- Figure 4.2. Detailed layout of the mixer.
- Figure 4.3. Conversion loss versus frequency for the mixer shown in Figure 4.2.

- Figure 4.4. Mixer noise temperature versus LO power.
- Figure 4.5. Radiation patterns of the mixer integrated with a Vivaldi antenna.
- Figure B.1. Command file to execute program SPECASMNASA.
- Figure B.2. Input data file.
- Figure B.3. Log file from batch execution.
- Figure B.4. Output file.
- Figure B.5. Definition of center coordinates, half-length (h), and width (w) for one expansion mode.



a



b

Figure 2.1.1. A comparison of single element LTSA radiation patterns obtained by using a) a split waveguide block feed and b) a detector diode soldered to the narrow portion of the slot.

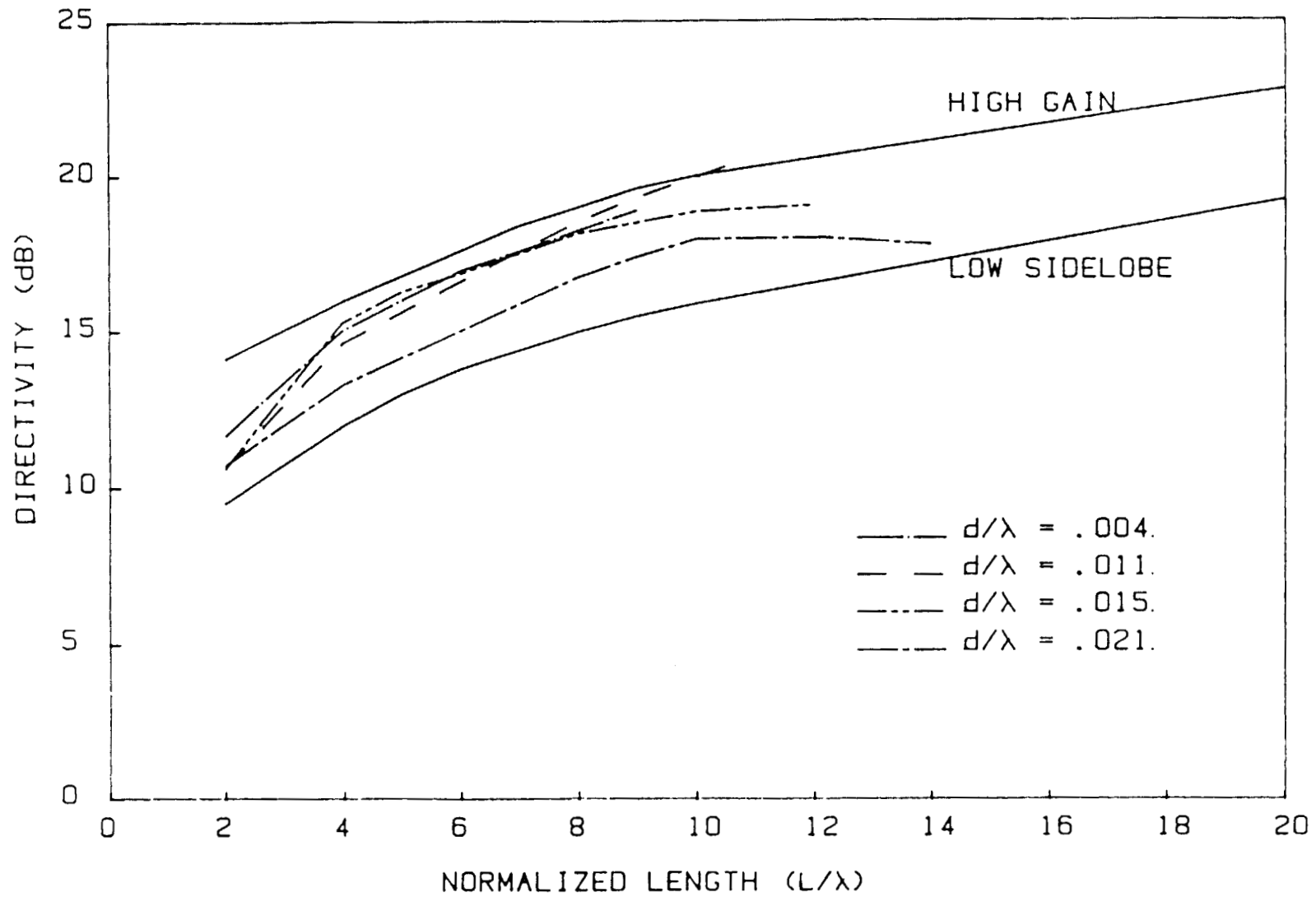


Figure 2.1.2. Directivity of single element LTSA's versus normalized length for four values of normalized dielectric thickness. Dielectric is Kapton ($\epsilon_r = 3.5$) and $2\gamma = 11.2^\circ$.

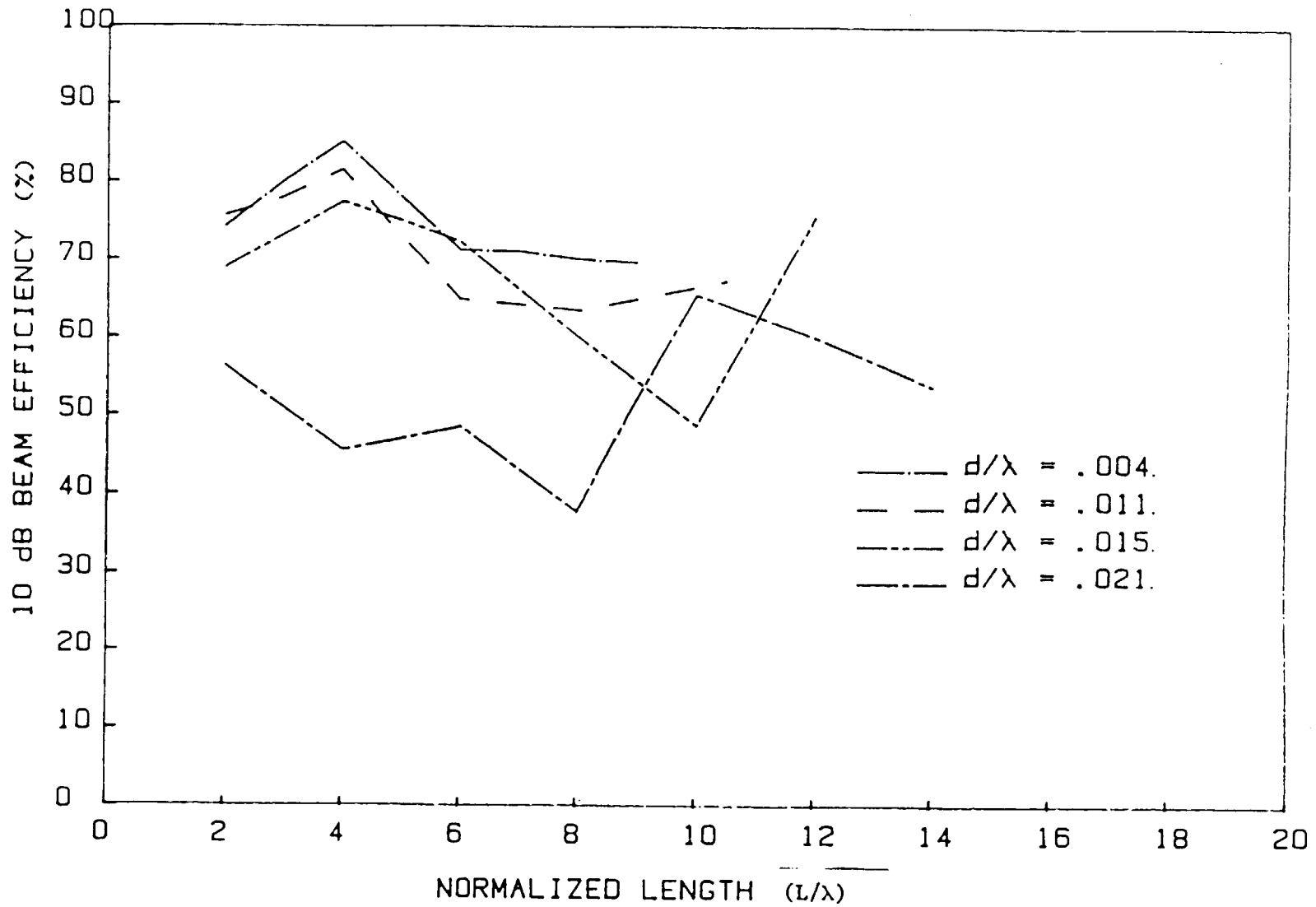


Figure 2.1.3. 10 dB beam efficiency versus normalized length for the same antennas as in Figure 2.1.2.

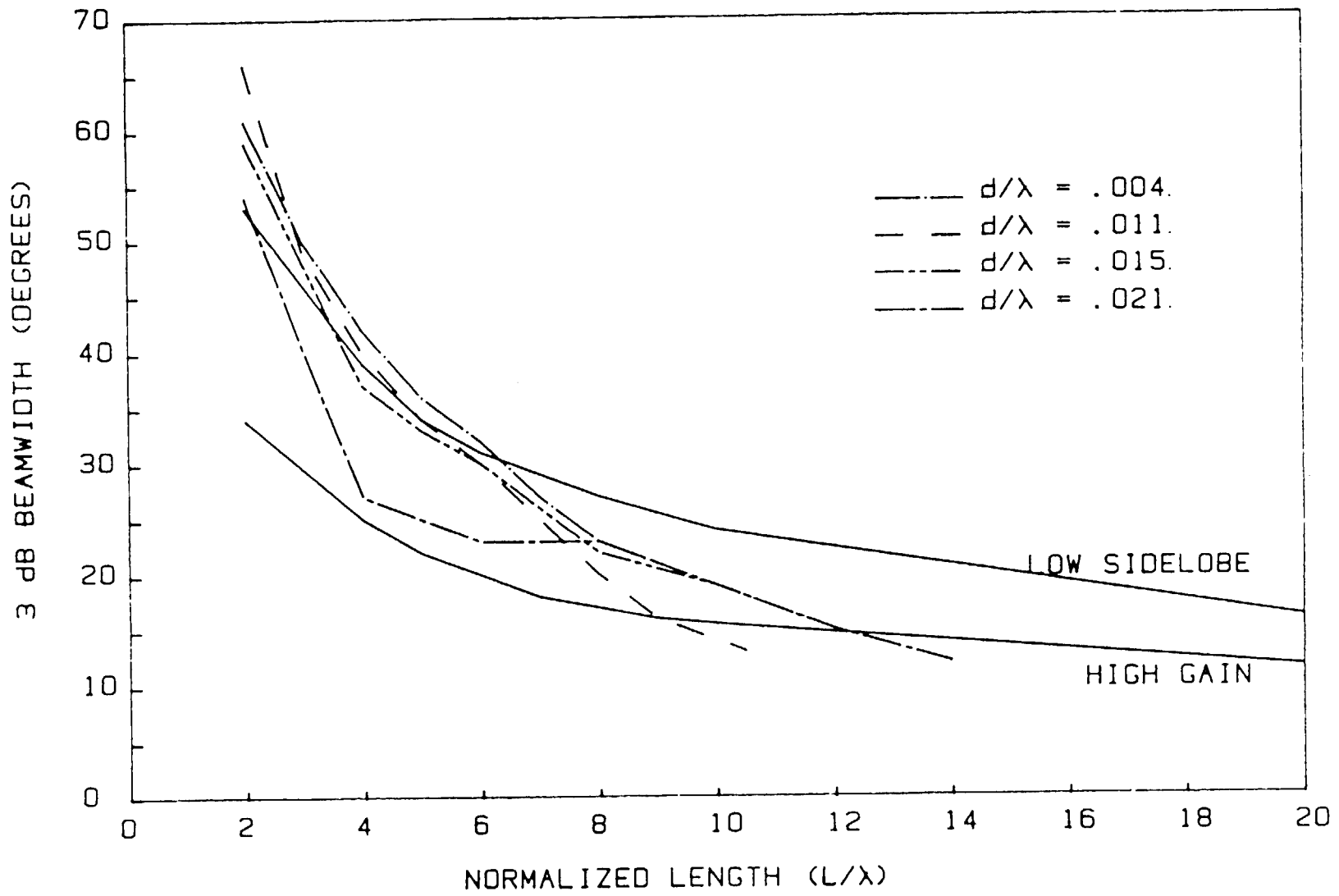


Figure 2.1.4. 3 dB beam width versus L/λ_0 for the same antennas as in Figure 2.1.2.
 (a) E-plane (b) H-plane.

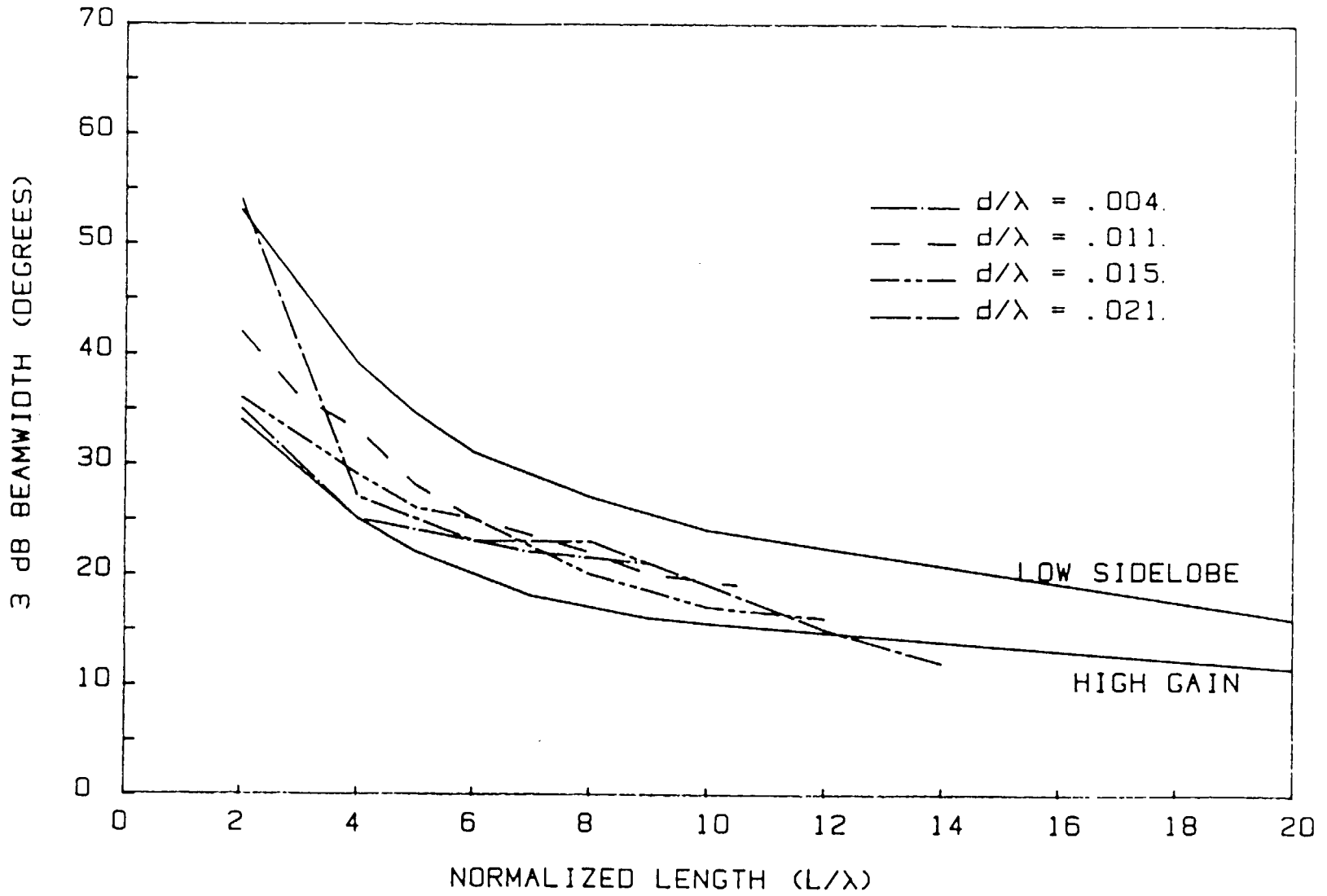


Figure 2.1.4b.

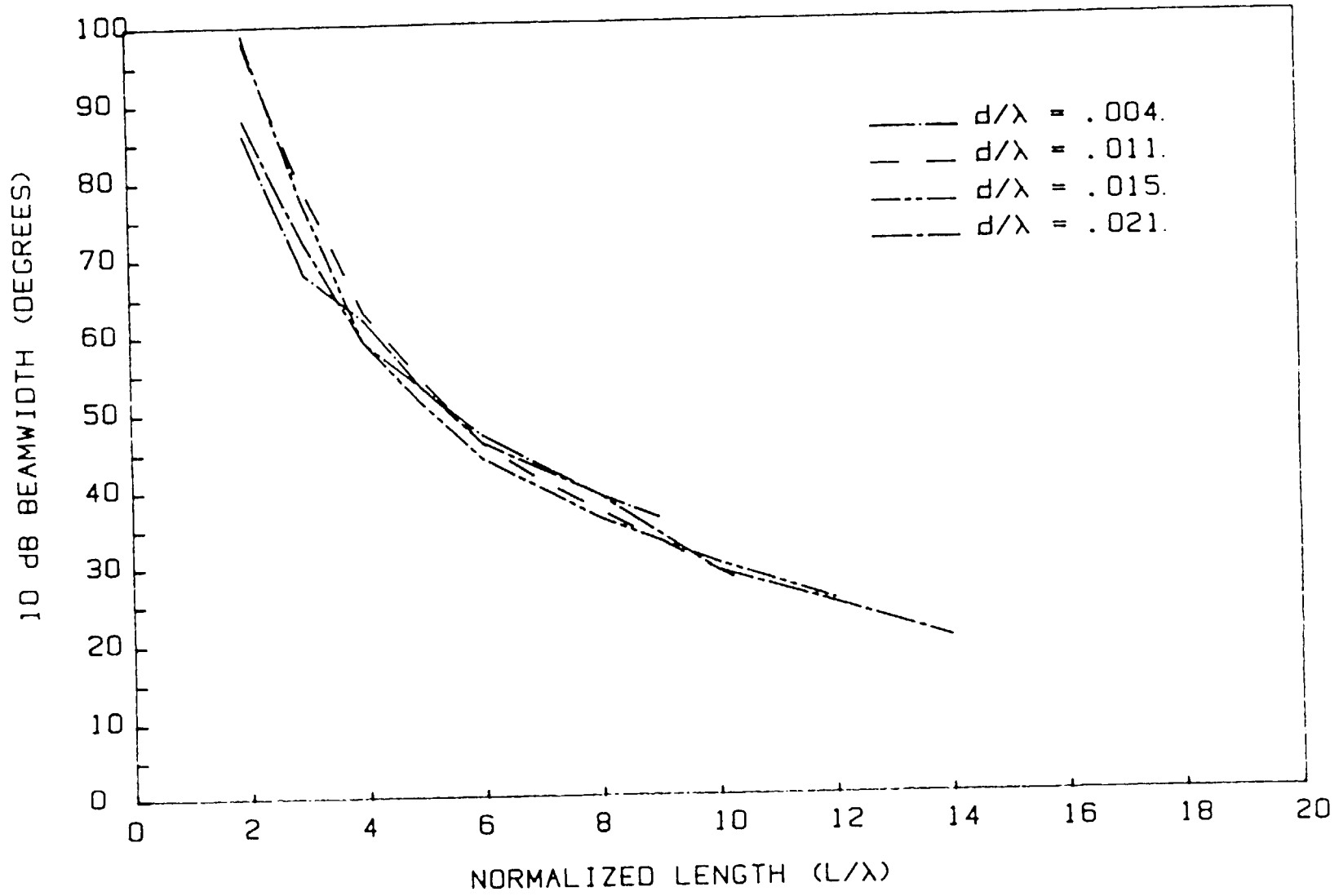


Figure 2.1.5. 10 dB beamwidth versus L/λ_0 for the same antennas as in Figure 2.1.2.
 (a) E-plane (b) H-plane.

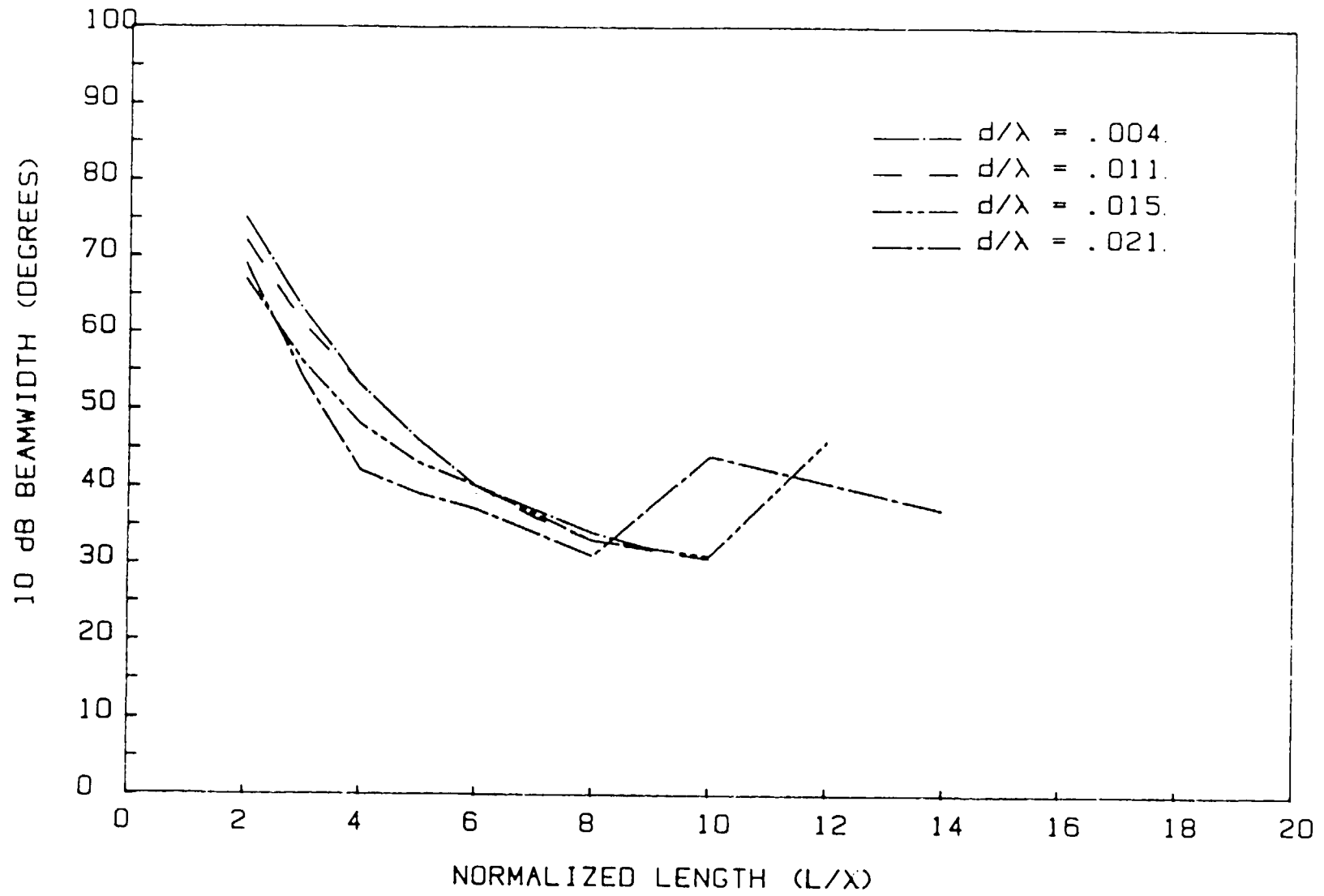


Figure 2.1.5b.

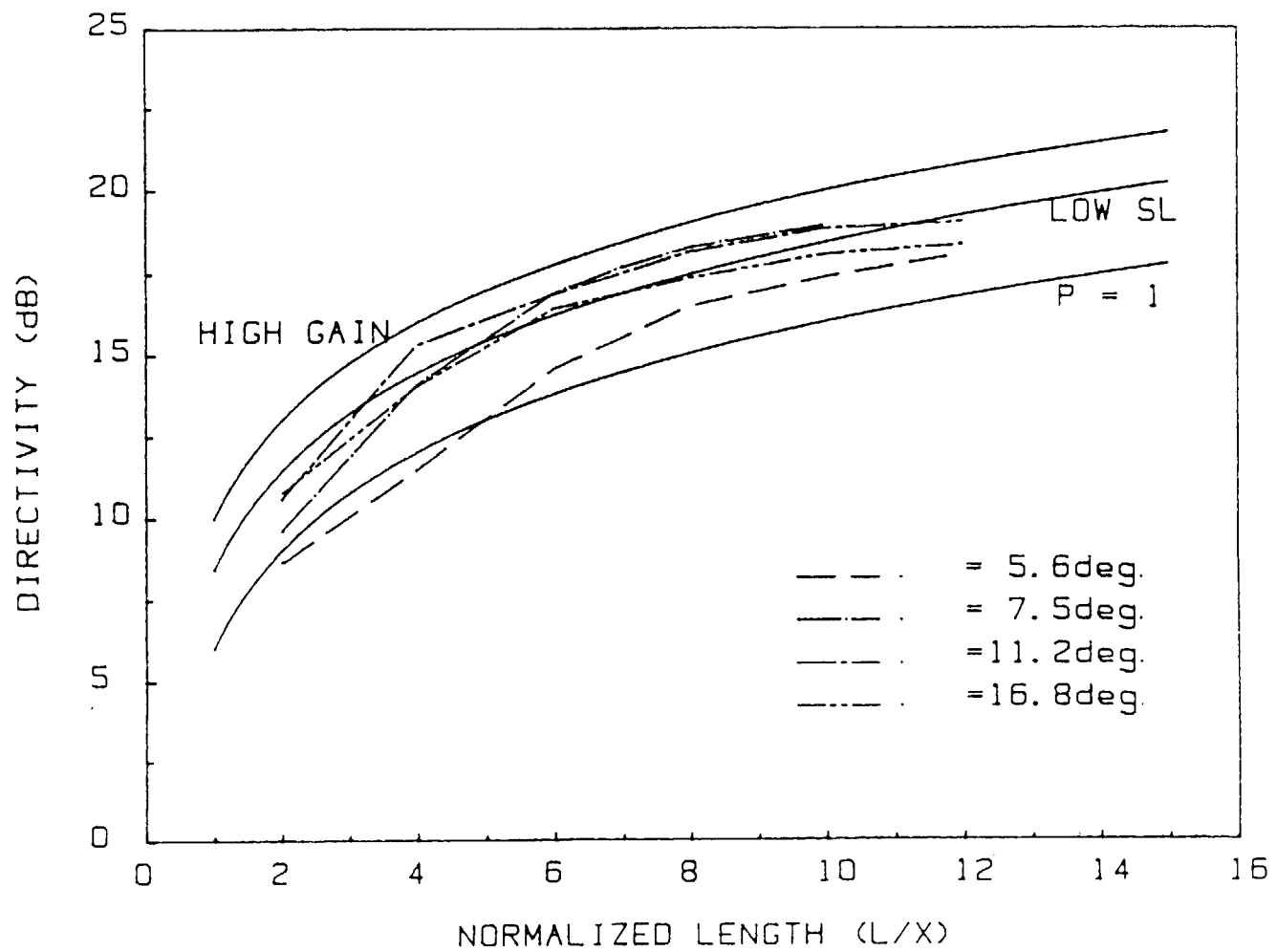


Figure 2.1.6. Directivity versus normalized length for LTSA single elements with the opening angle (2γ) as a parameter. Substrate: 5 mil (0.13 mm) Kapton.

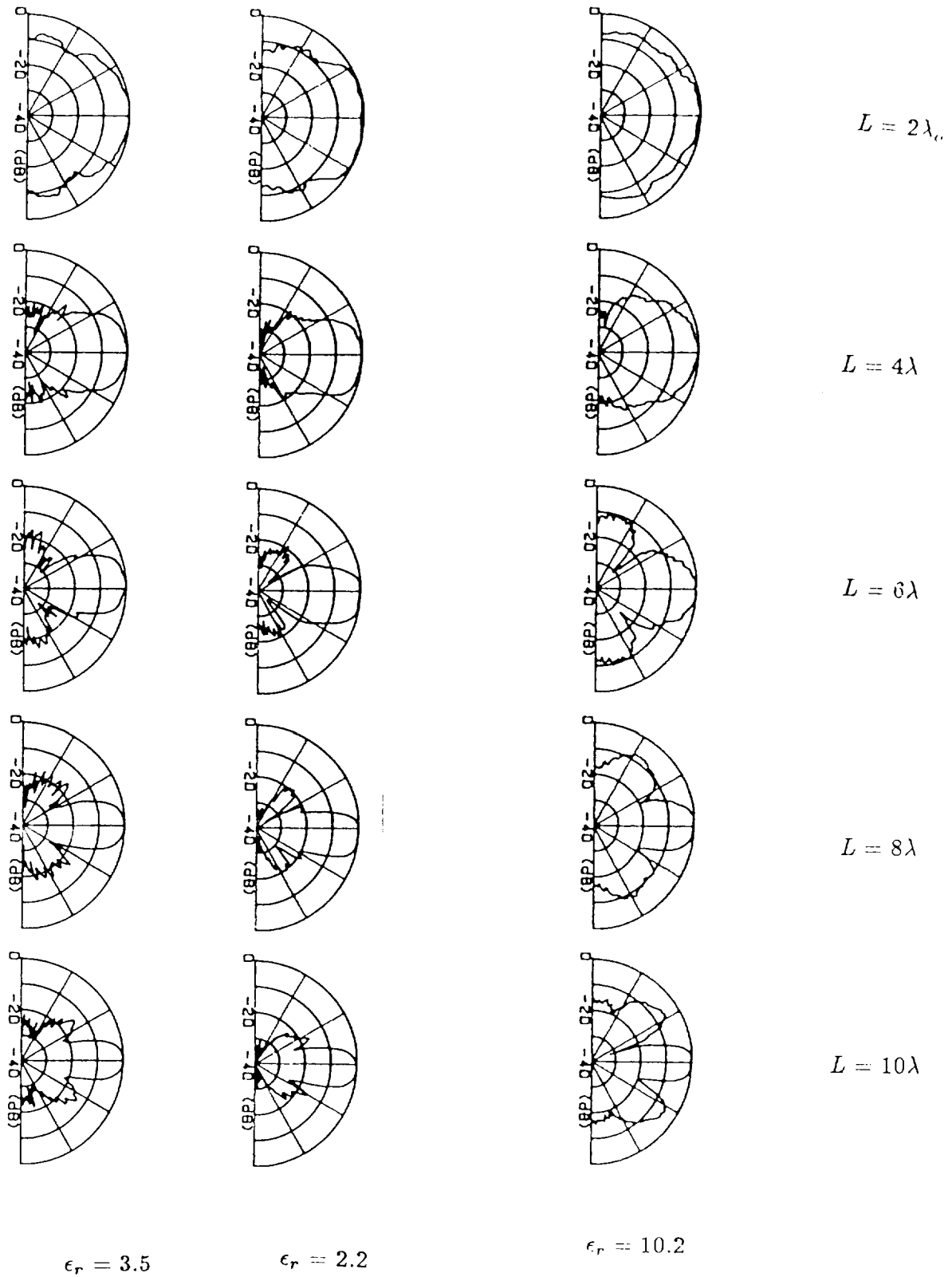


Figure 2.1.7. Radiation patterns of LTSA single elements on three different substrates, all of 5 mil (0.13 mm) thickness: (1) Kapton ($\epsilon_r = 3.5$), (2) Duroid ($\epsilon_r = 2.2$), (3) Duroid 6010 ($\epsilon_r = 10.2$), $2\gamma = 11.2^\circ$ (a) E-plane (b) H-plane.

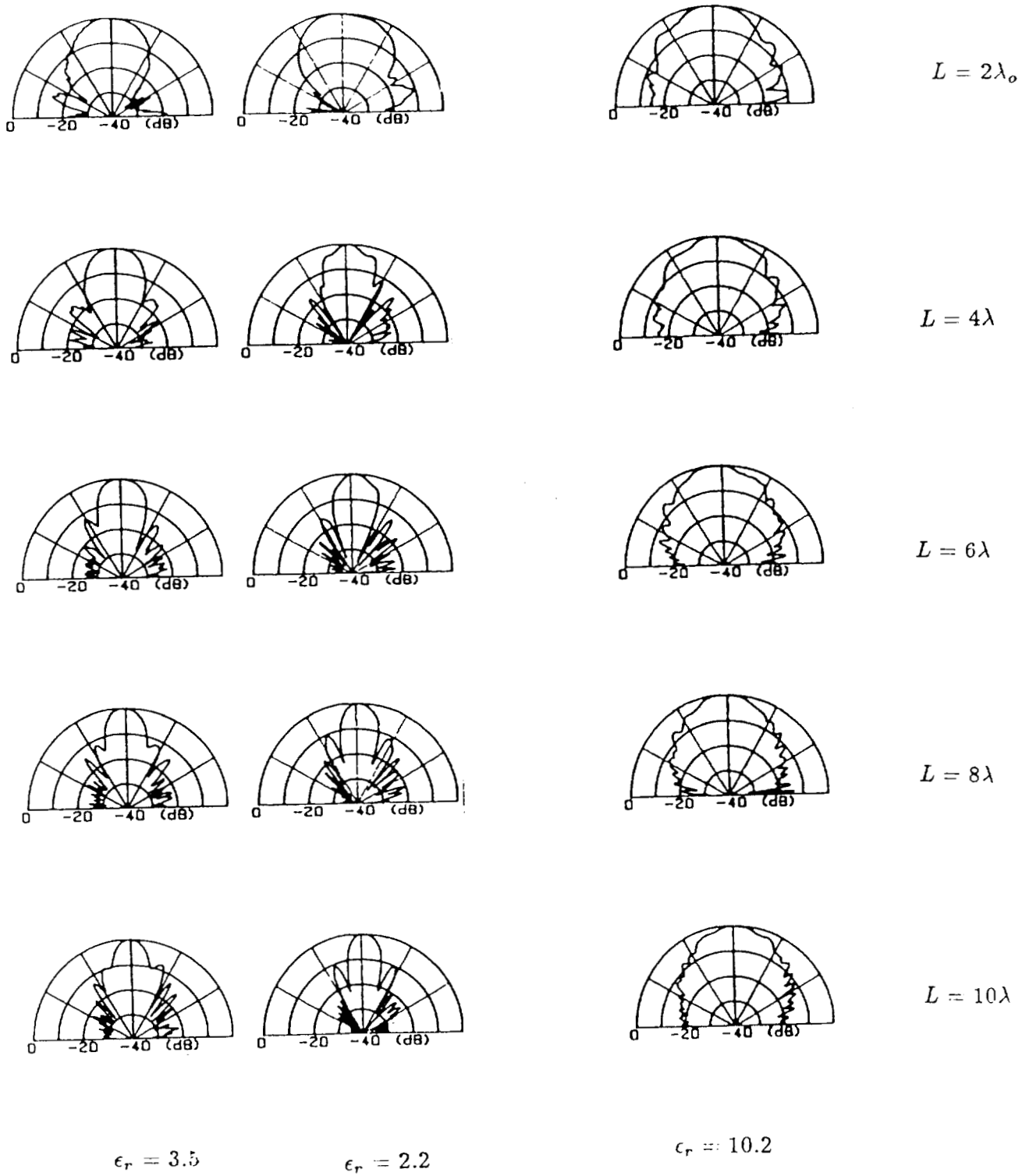


Figure 2.1.7b.

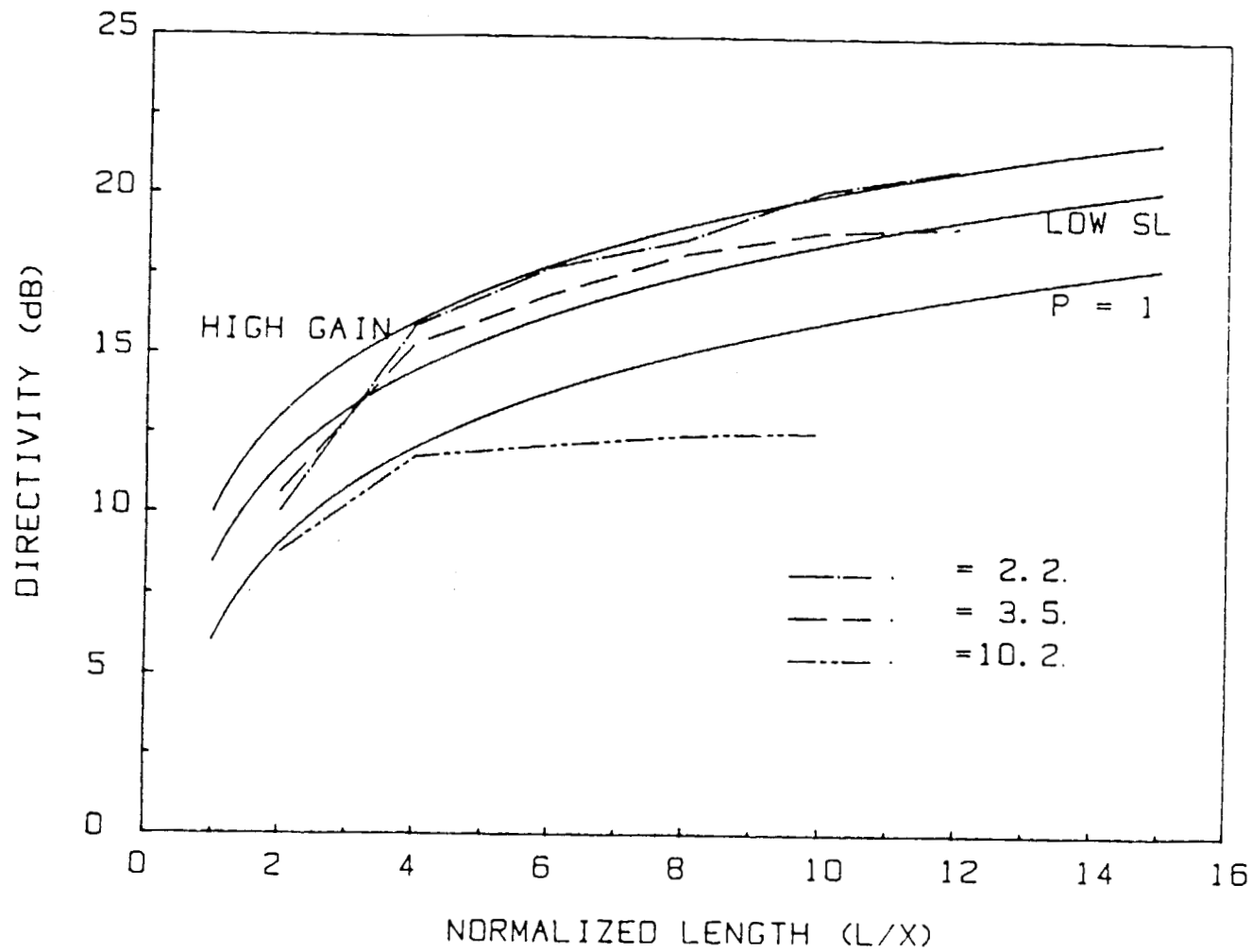
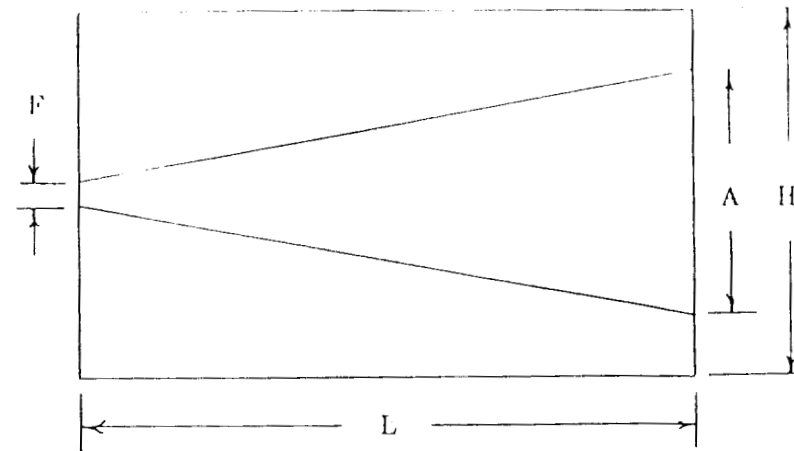
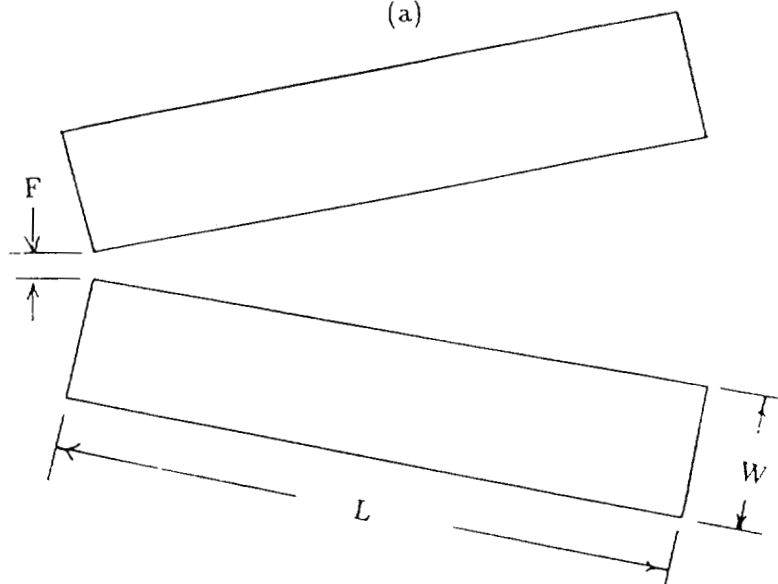


Figure 2.1.8. Directivity versus normalized length for the same LTSA's as in Figure 2.1.7.



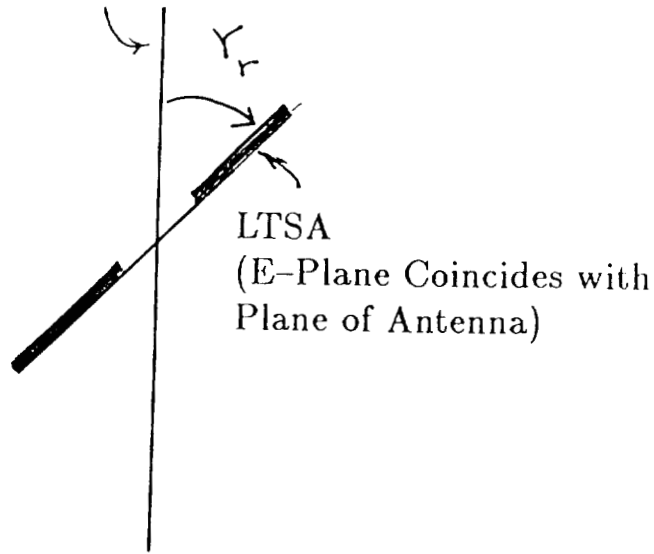
(a)



(b)

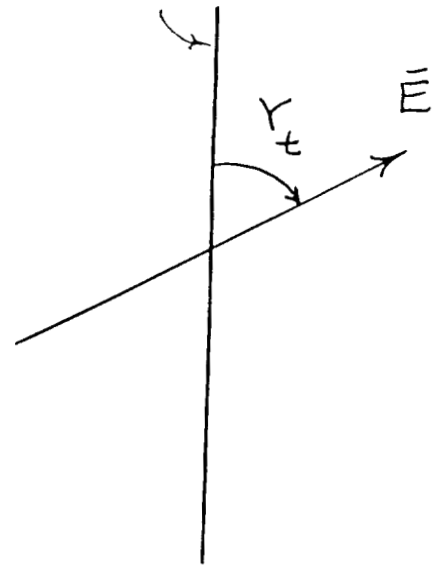
Figure 2.2.1. Antenna geometries and dimensions.

Vertical Line
(Axis of Rotation)



(a)

Vertical Line



(b)

Figure 2.2.2. Definitions of antenna orientation (a) and transmitted field (b) for radiation pattern measurements.

Date: 1 Mar 1900 Time: 02:04
Reference Level: -5.34 dB

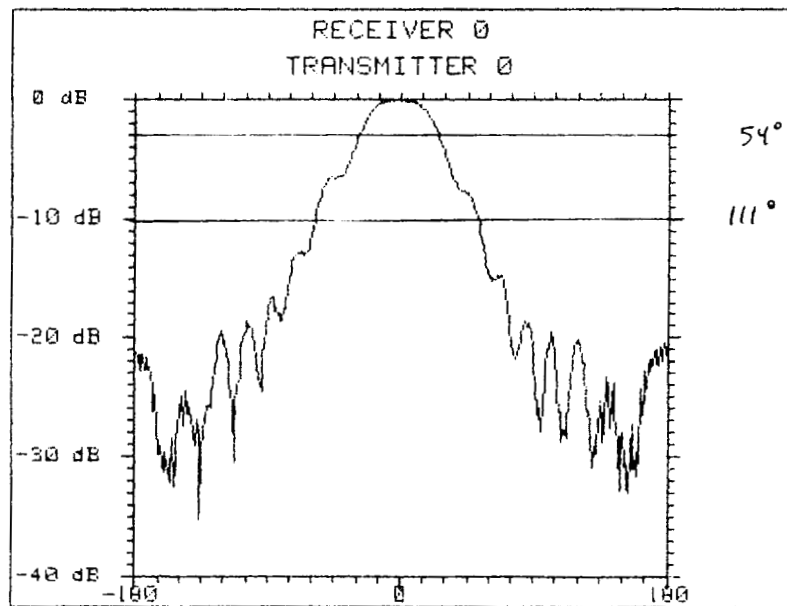
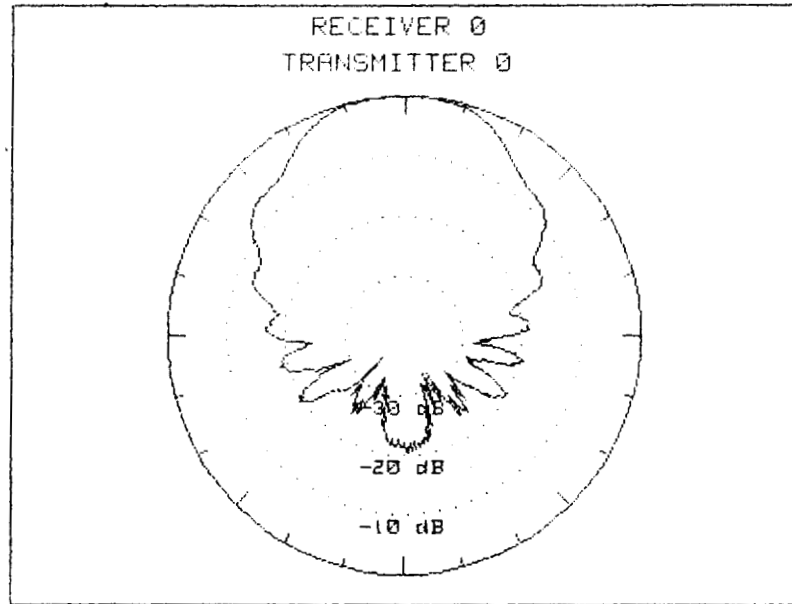


Figure 2.2.3. (12 pages of diagrams) - 1 of 12

Figure 2.2.3. Radiation patterns of antenna number 4 at 7 GHz.

Date: 1 Mar 1900 Time: 02:06
Reference Level: -24.86 dB

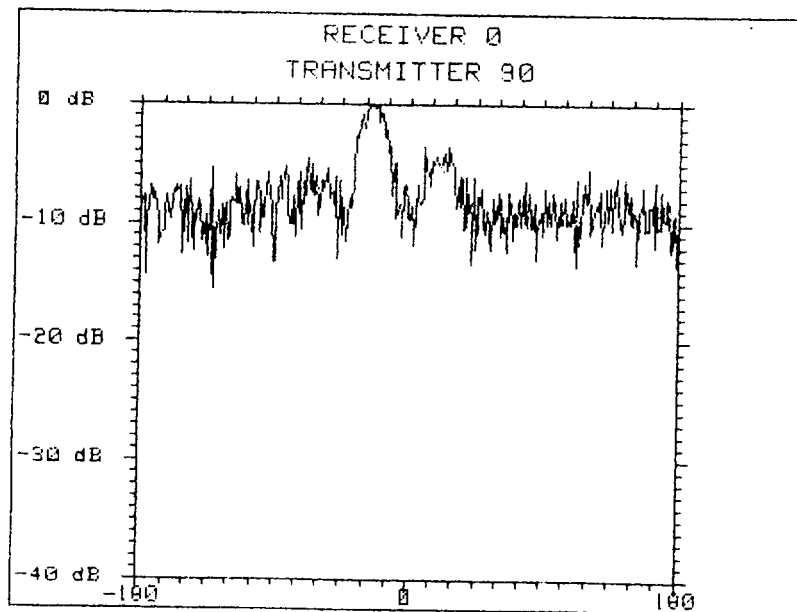
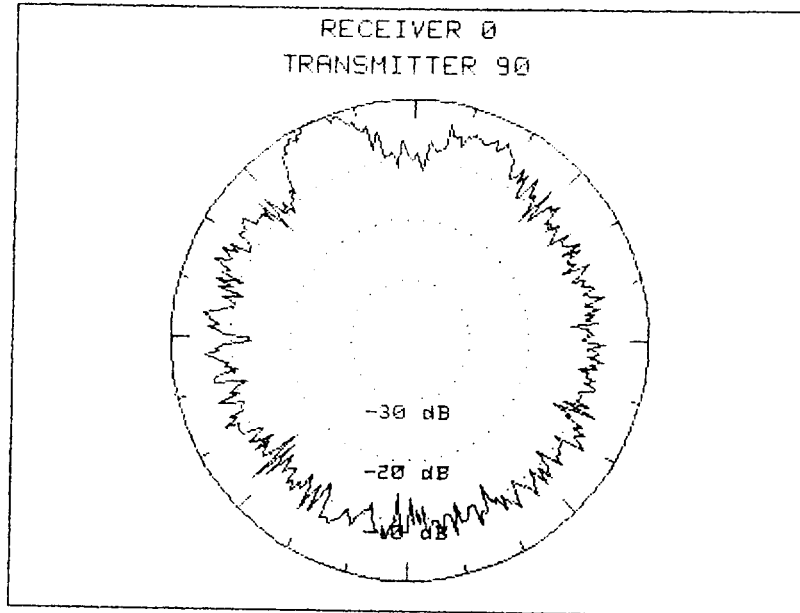


Figure 2.2.3. (12 pages of diagrams) - 2 of 12

Date: 1 Mar 1900 Time: 02:07
Reference Level: -4.69 dB

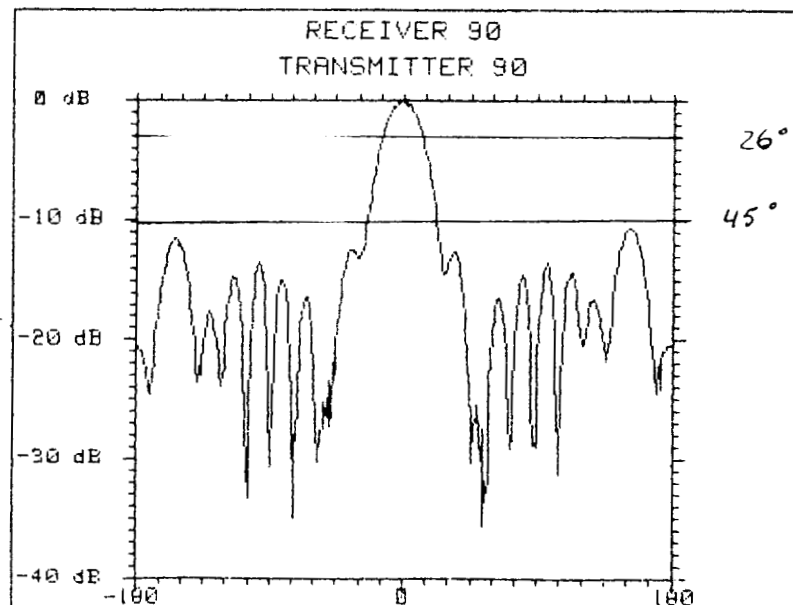
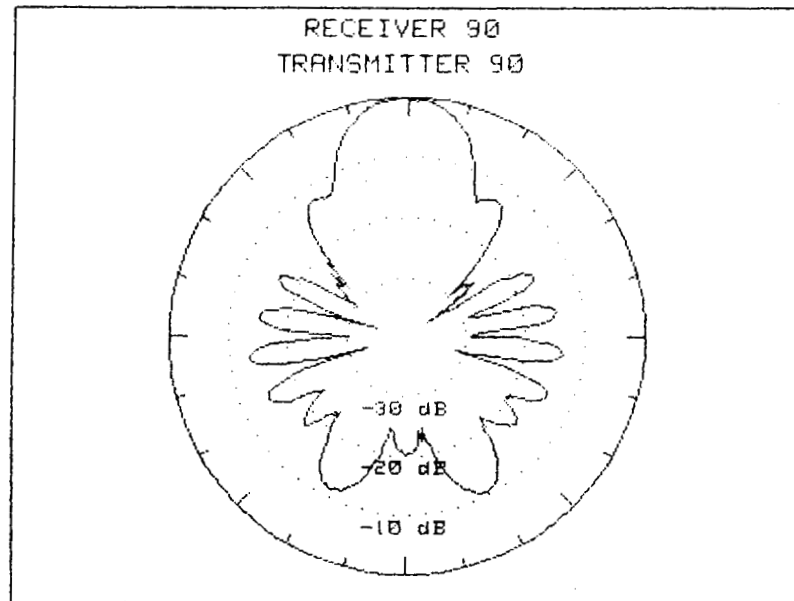


Figure 2.2.3. (12 pages of diagrams) - 3 of 12

Date: 1 Mar 1900 Time: 02:08
Reference Level: -25.13 dB

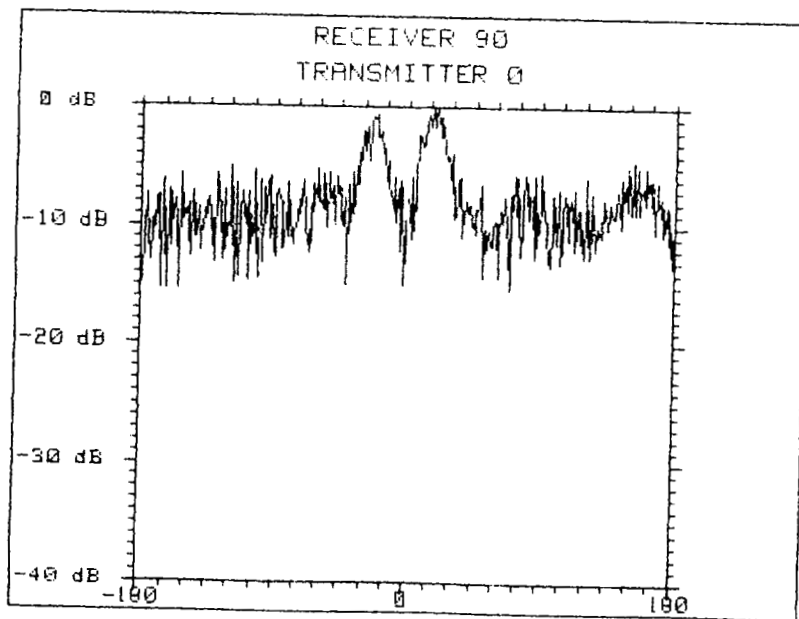
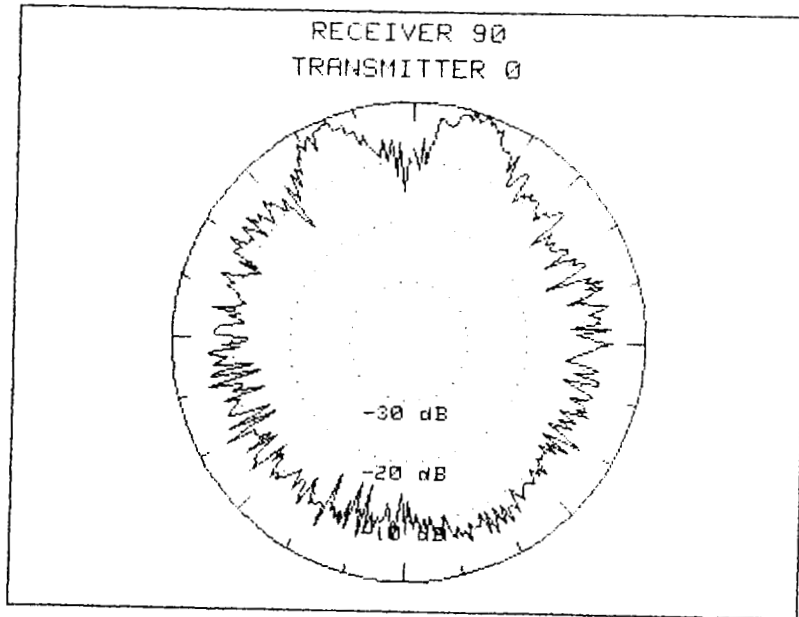


Figure 2.2.3. (12 pages of diagrams) - 4 of 12

Date: 1 Mar 1900 Time: 02:09
Reference Level: -5.02 dB

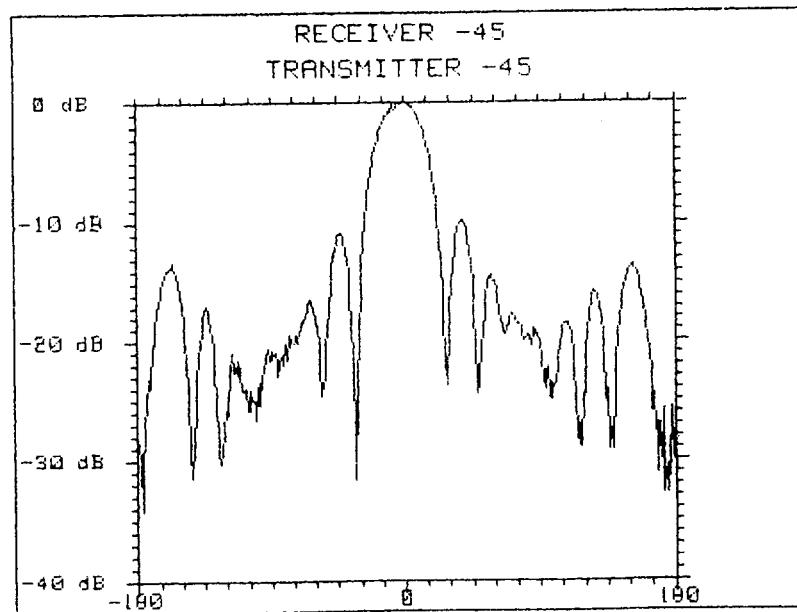
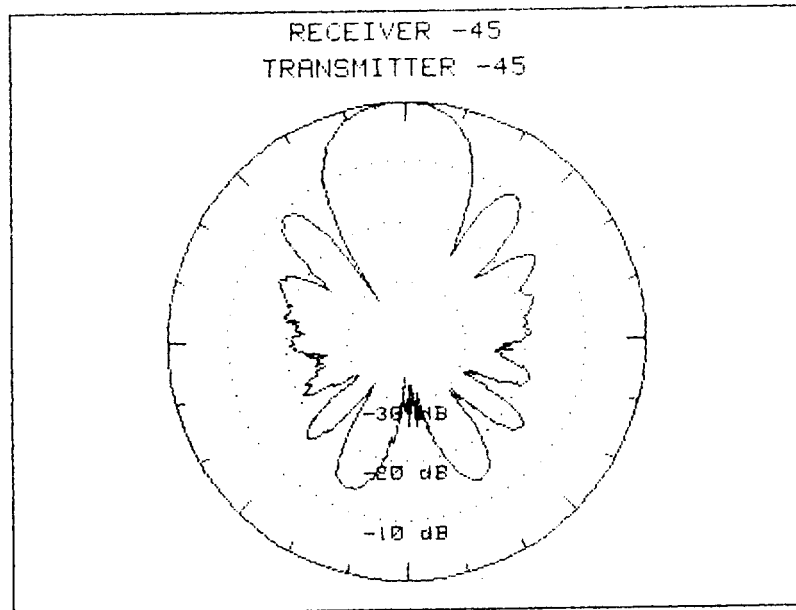


Figure 2.2.3. (12 pages of diagrams) - 5 of 12

Date: 1 Mar 1900 Time: 02:10
Reference Level: -13.02 dB

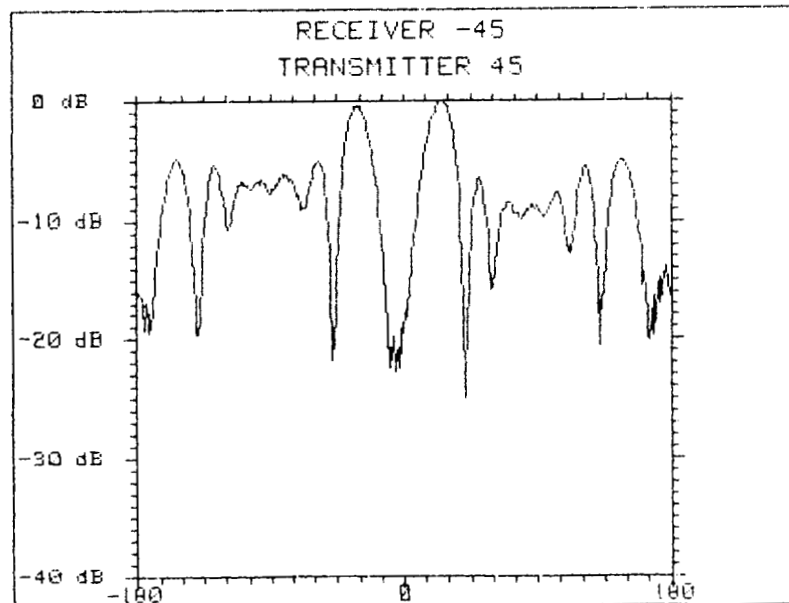
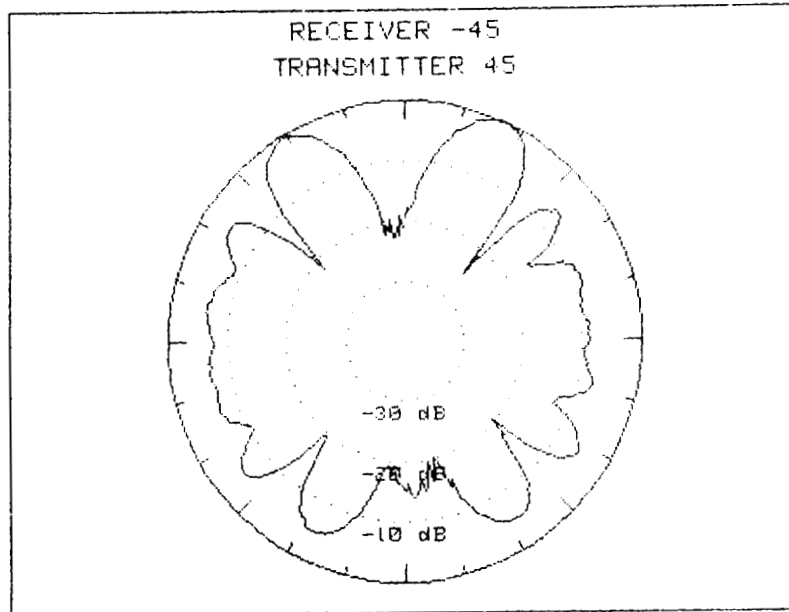


Figure 2.2.3. (12 pages of diagrams) - 6 of 12

Date: 1 Mar 1900 Time: 02:11
Reference Level: -4.97 dB

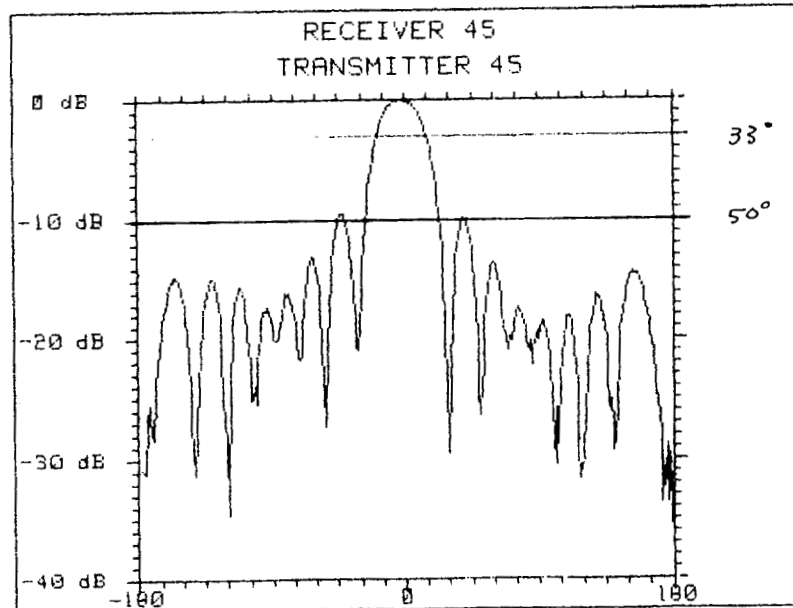
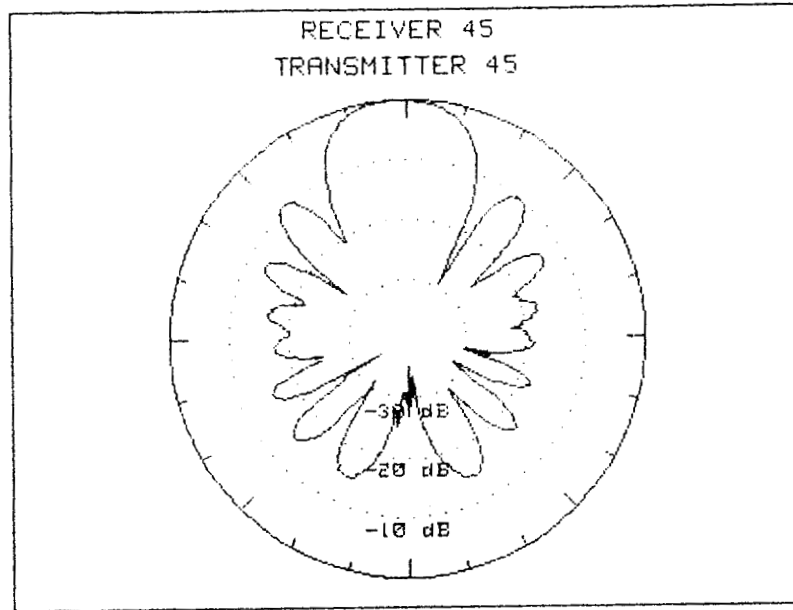


Figure 2.2.3. (12 pages of diagrams) - 7 of 12

Date: 1 Mar 1900 Time: 02:12
Reference Level: -13.02 dB

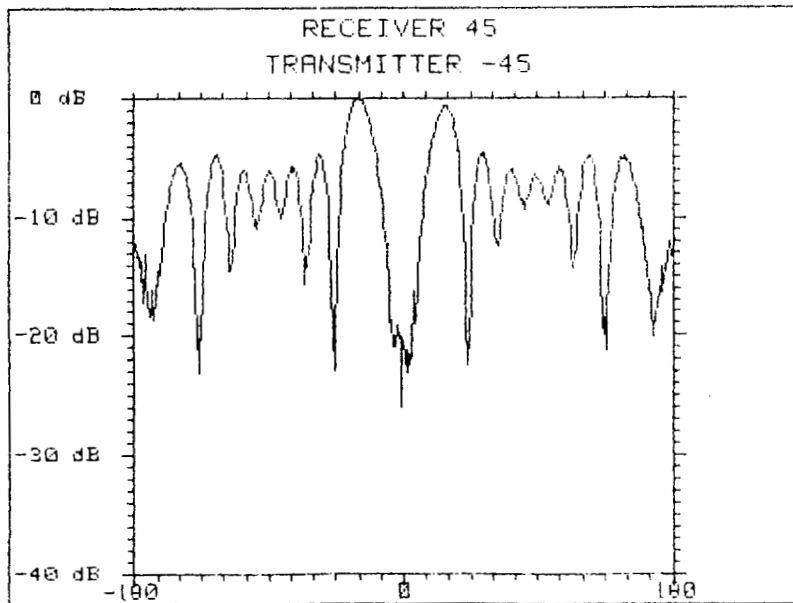
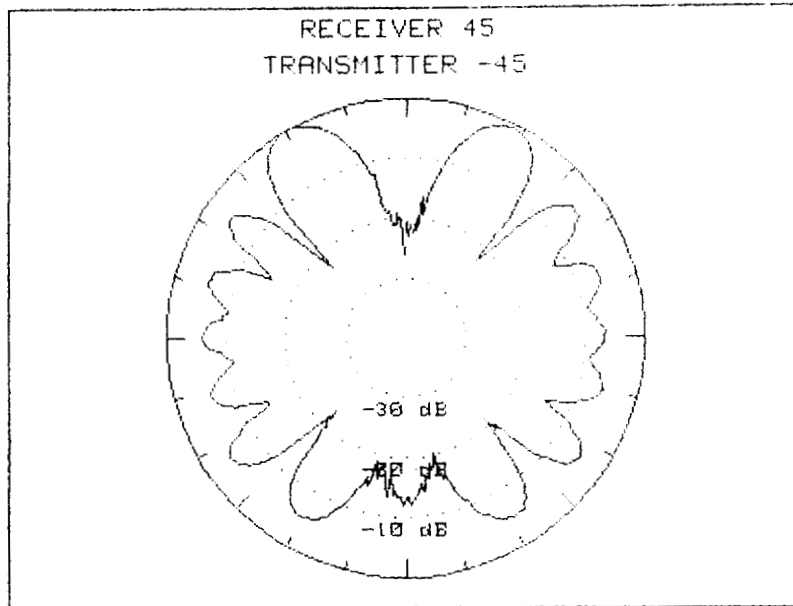


Figure 2.2.3. (12 pages of diagrams) - 8 of 12

Date: 1 Mar 1900 Time: 02:25
Reference Level: -5.26 dB

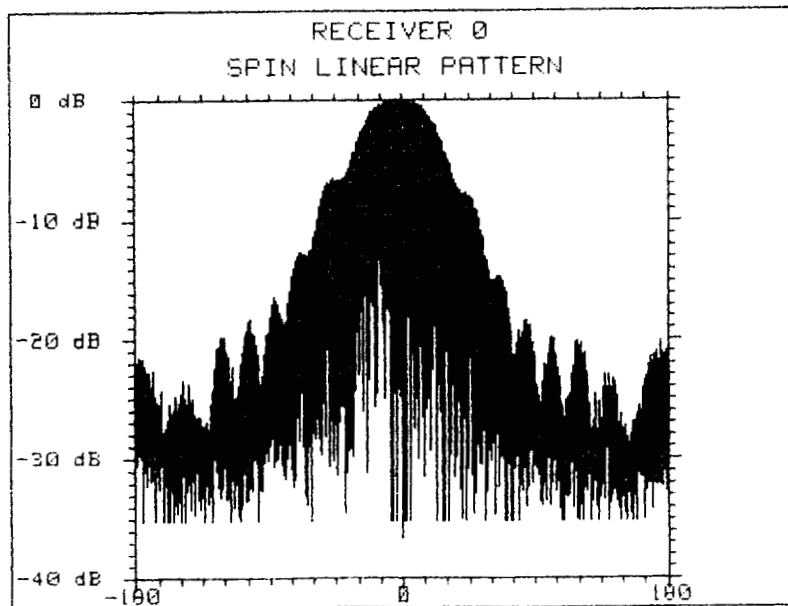
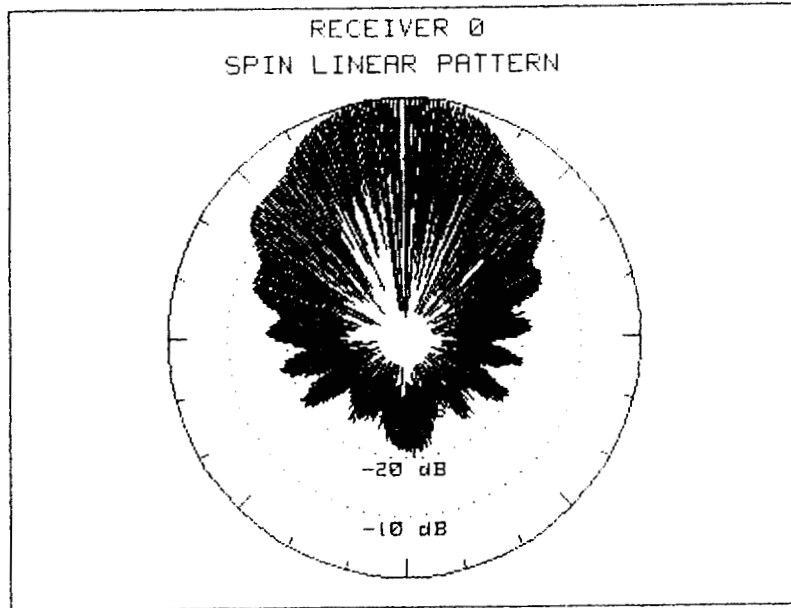


Figure 2.2.3. (12 pages of diagrams) - 9 of 12

Date: 1 Mar 1900 Time: 02:28
Reference Level:-4.54 dB

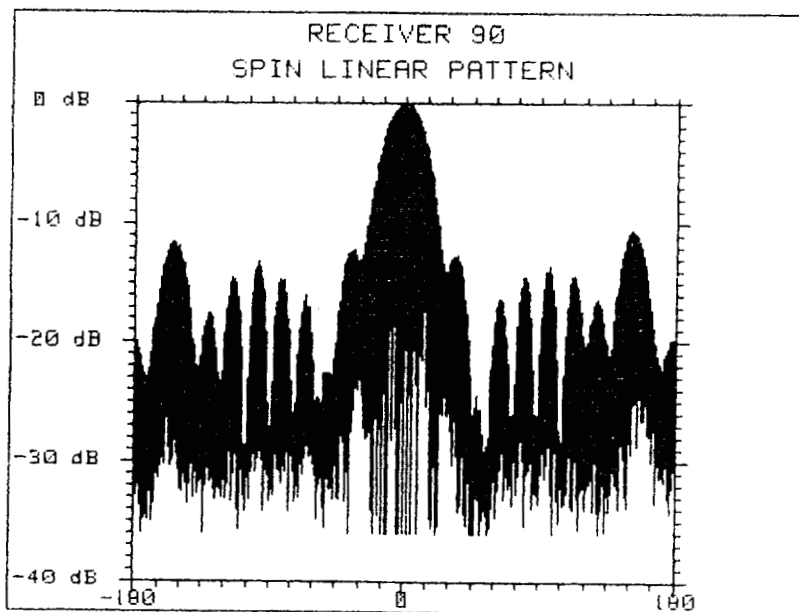
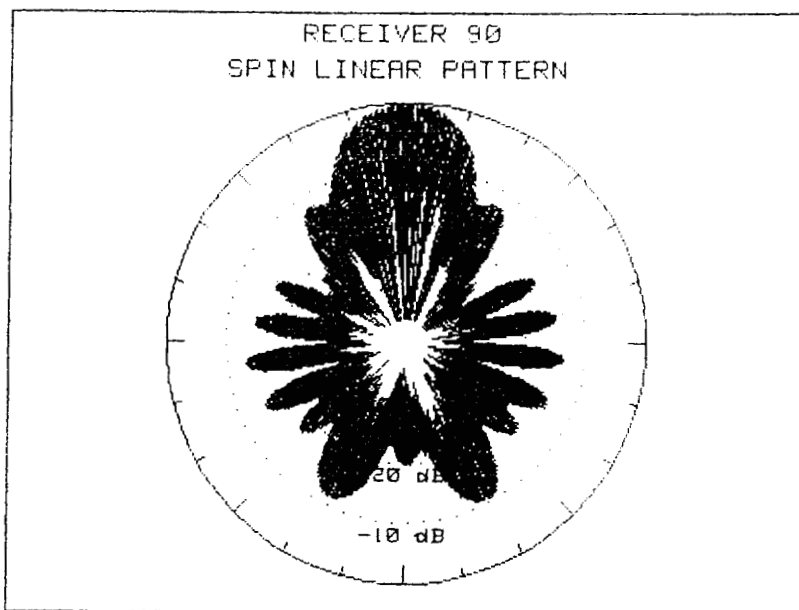


Figure 2.2.3. (12 pages of diagrams) - 10 of 12

Date: 1 Mar 1900 Time: 02:30
Reference Level: -4.99 dB

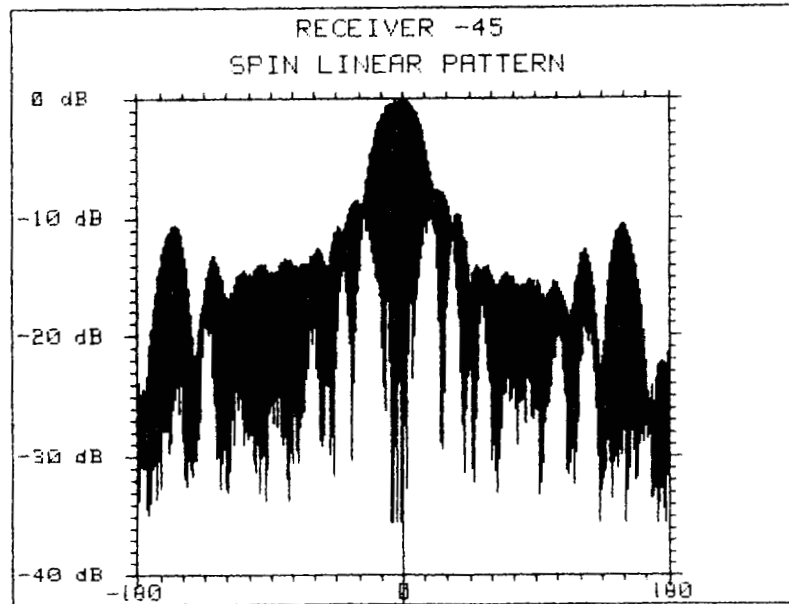
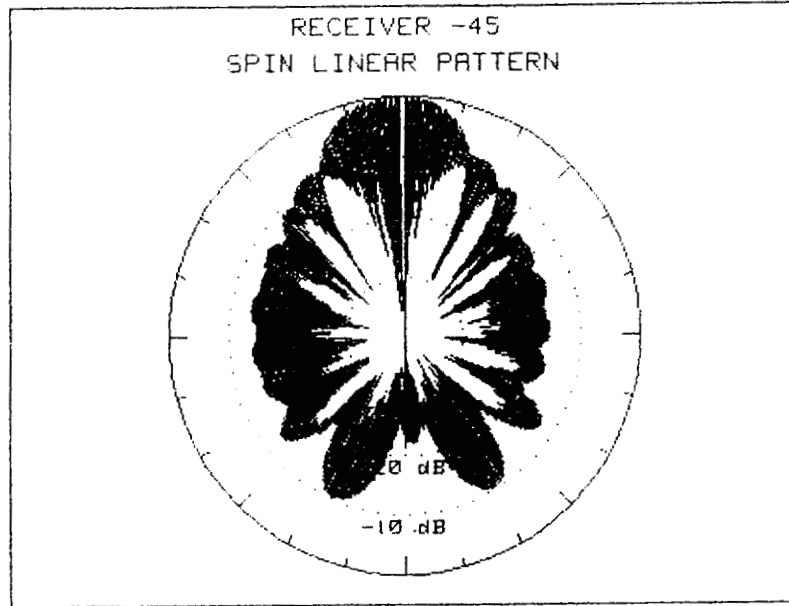
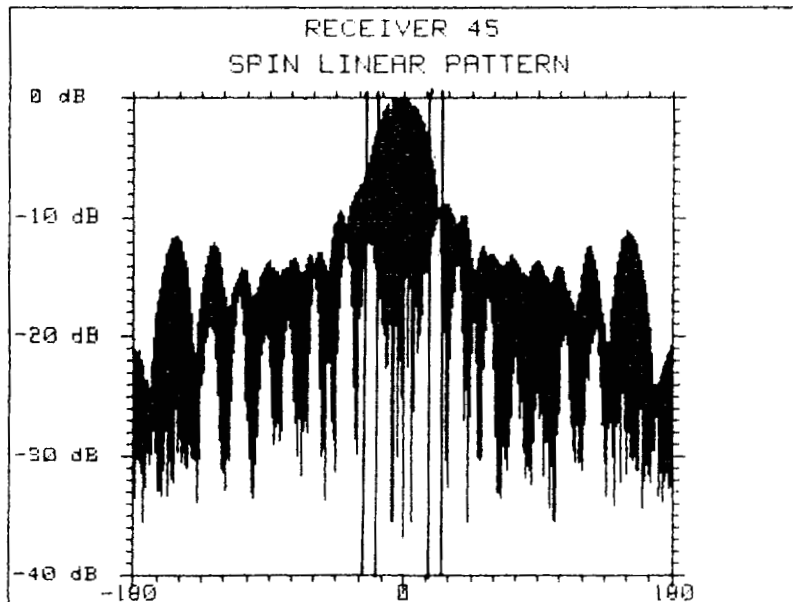
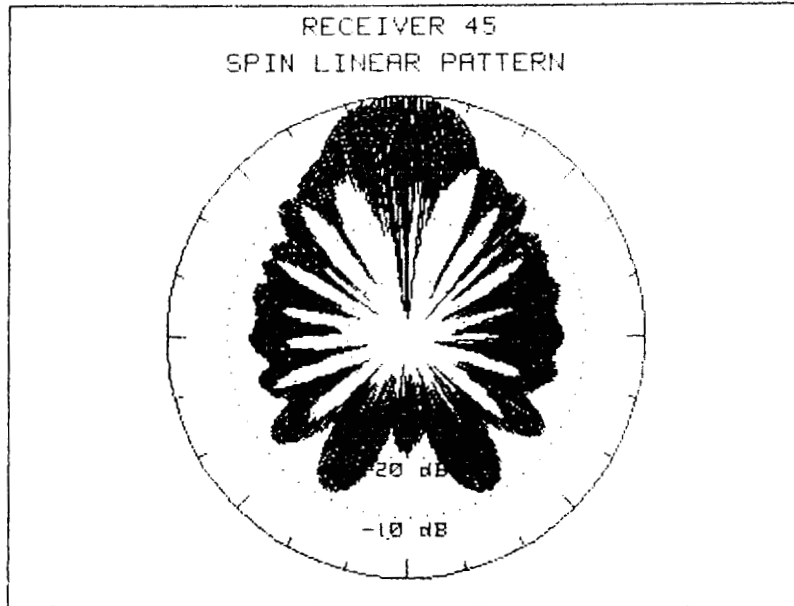


Figure 2.2.3. (12 pages of diagrams) - 11 of 12

Date: 1 Mar 1900 Time: 02:33
Reference Level: -4.97 dB



$AR_3 = 10.7$
 $AR_{10} = 0.9$

Figure 2.2.3. (12 pages of diagrams) - 12 of 12

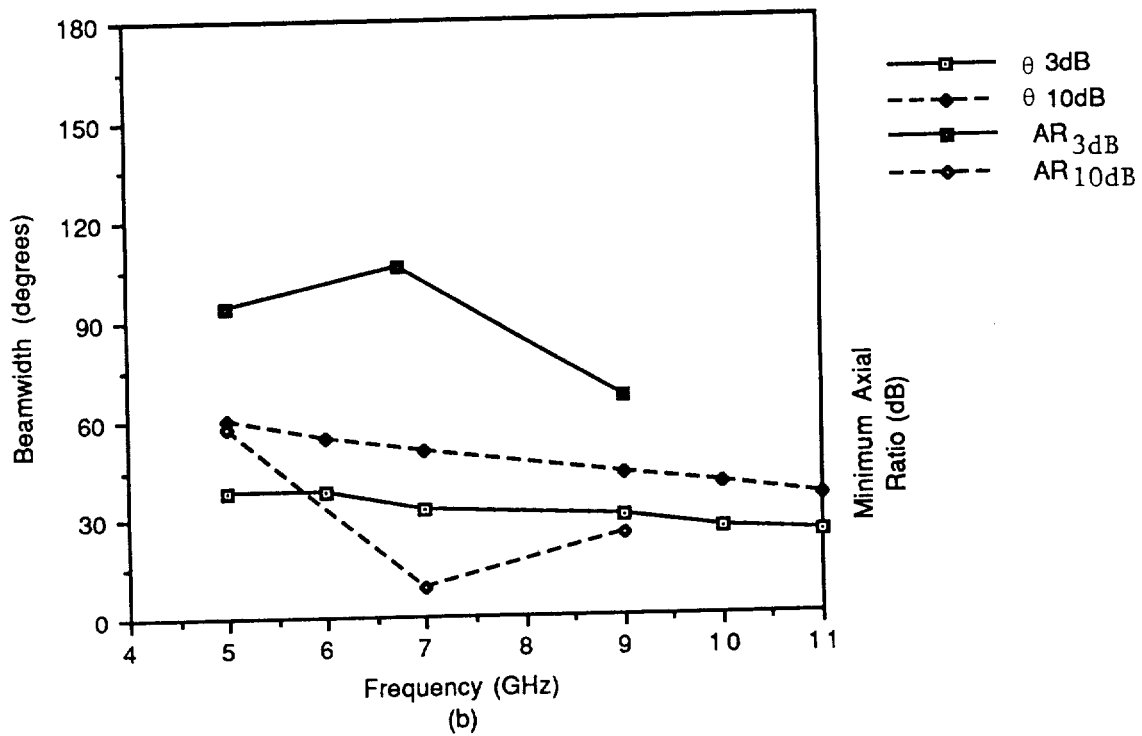
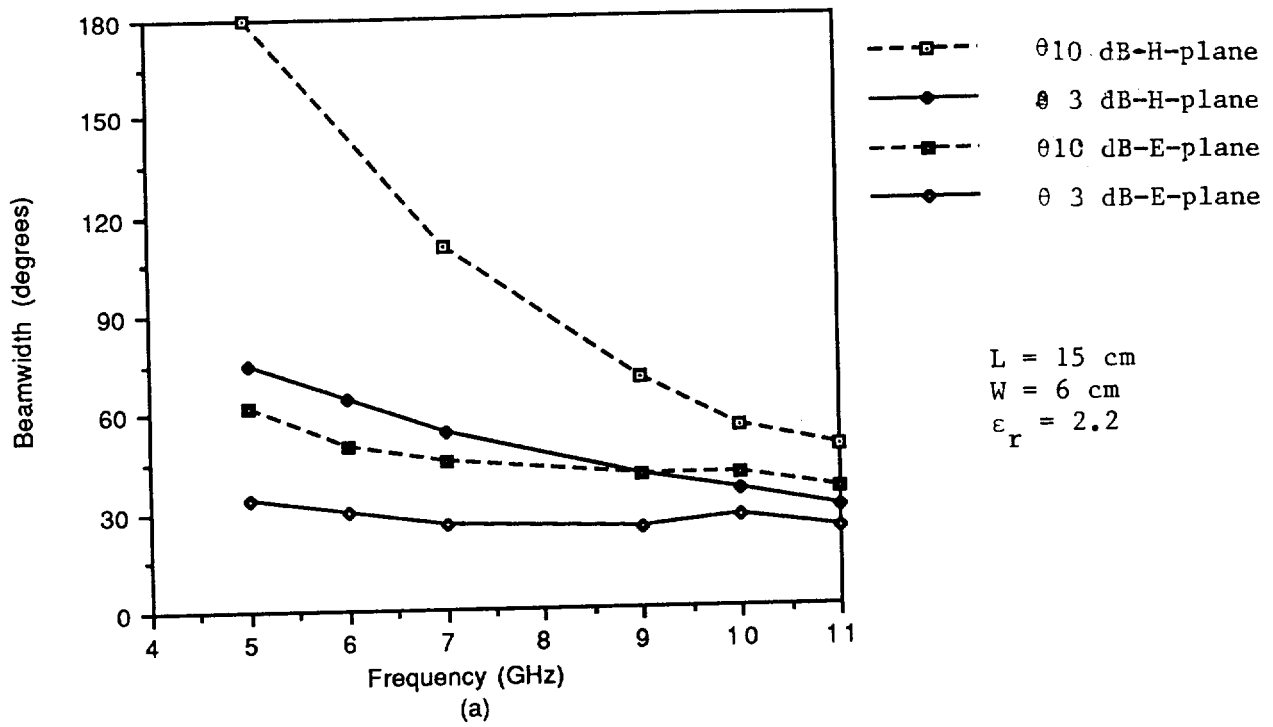


Figure 2.2.4. Beamwidths and axial ratios of antenna 4 (a) principal plane beamwidths, (b) diagonal plane beamwidths and axial ratios.

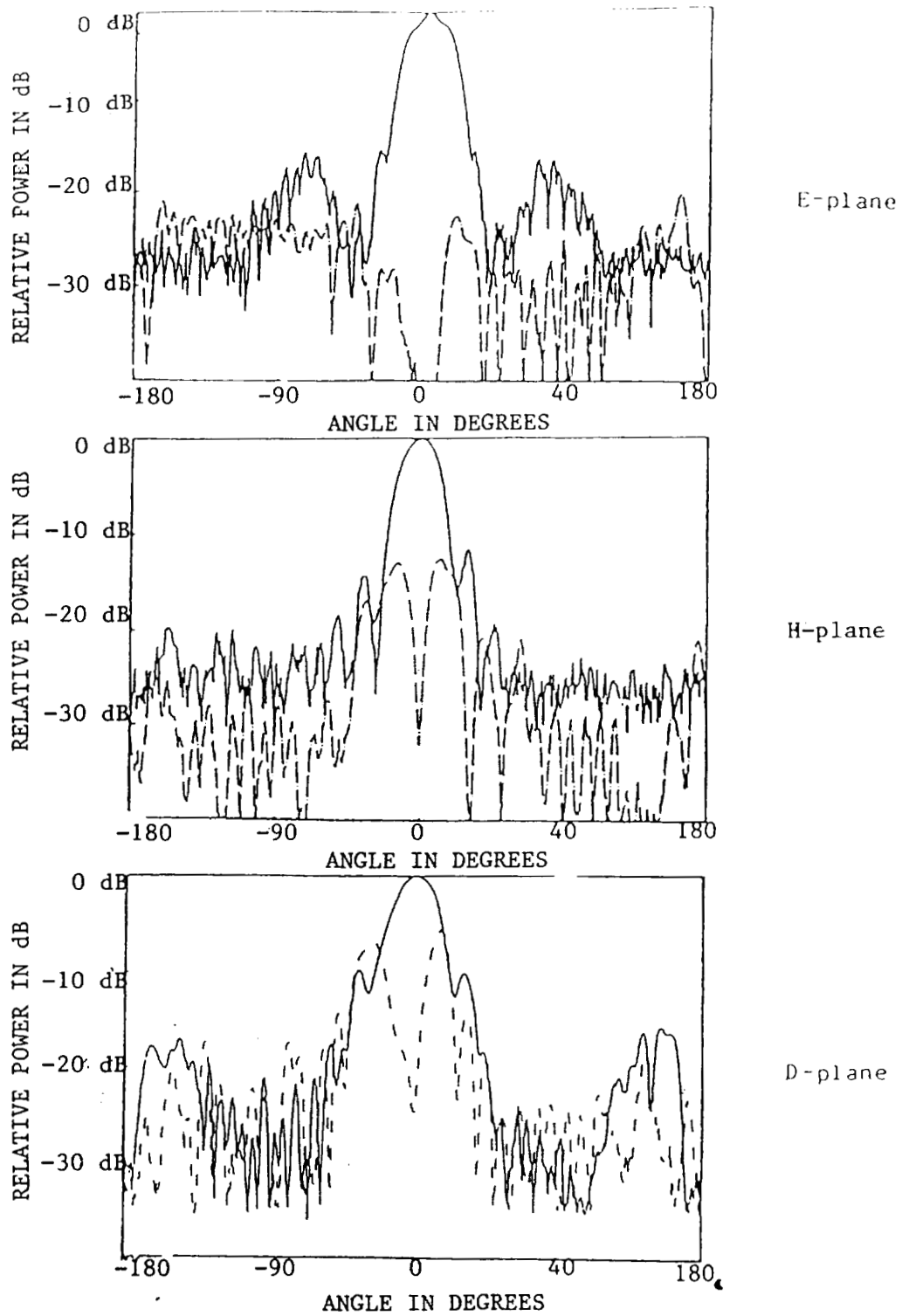


Figure 2.3.1 Co- and cross-polarized radiation patterns of the single element LTSA with $2\gamma = 11.2^\circ$ and $L/\lambda = 6$ on a 0.0127 cm Kapton substrate at 35 GHz (— co-pol, - - - x-pol)

53.54

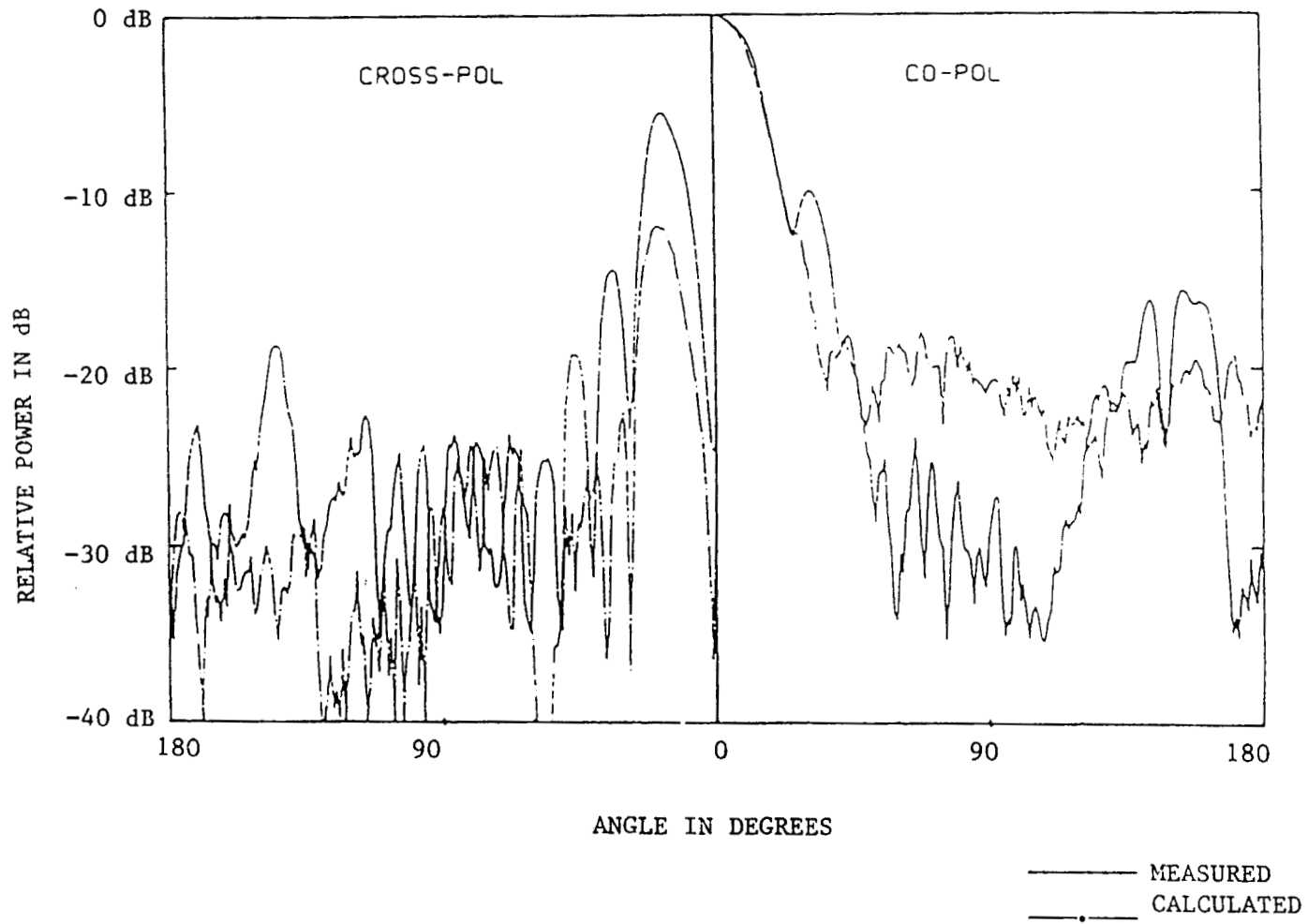


Figure 2.3.2. Comparison of calculated and measured patterns in the D-plane of a single LTSA.

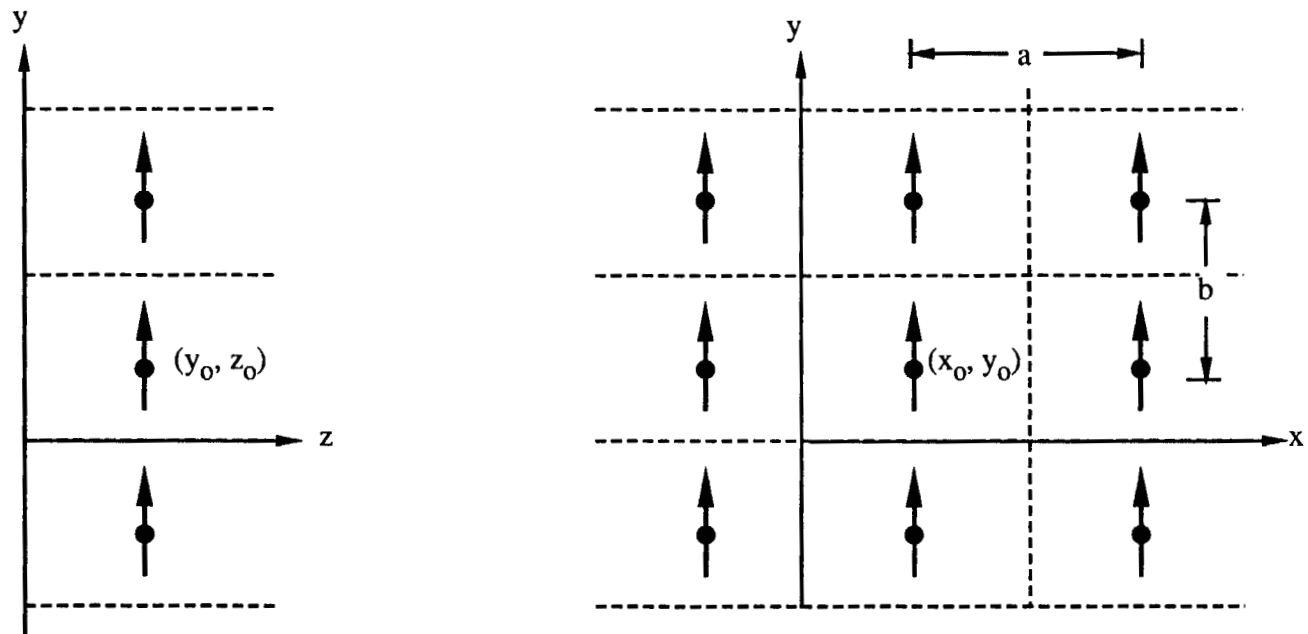


Figure 3.1.1. Array of y -directed currents for Green's function.

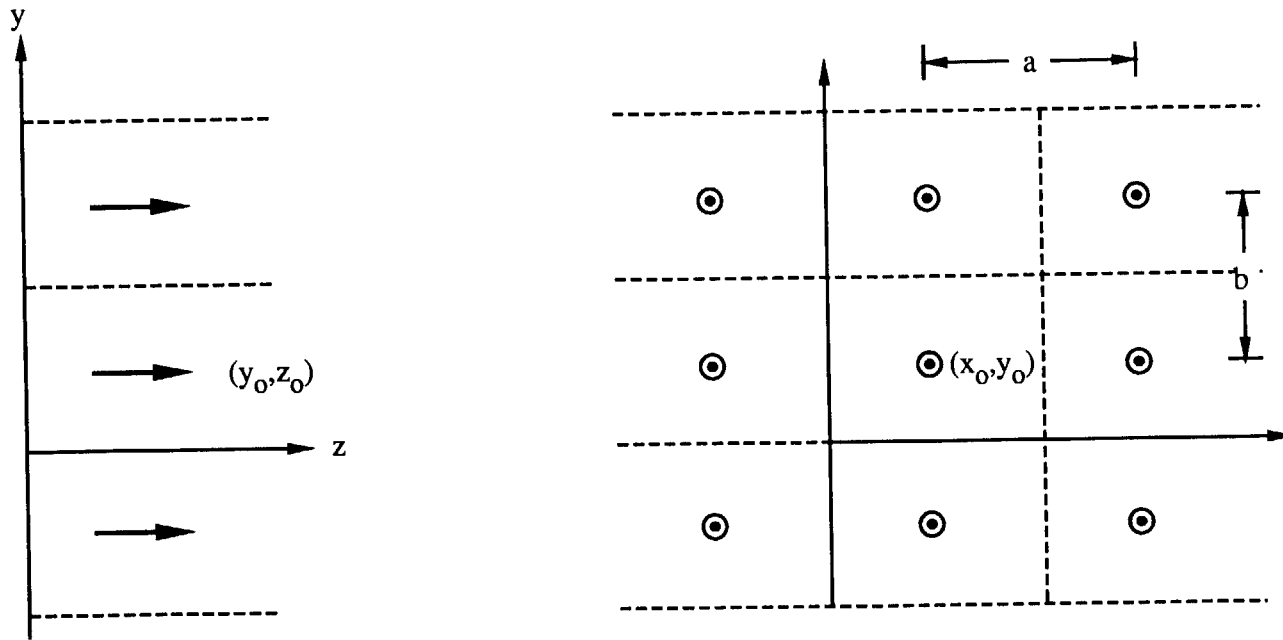


Figure 3.1.2. Array of z -directed currents for Green's function.

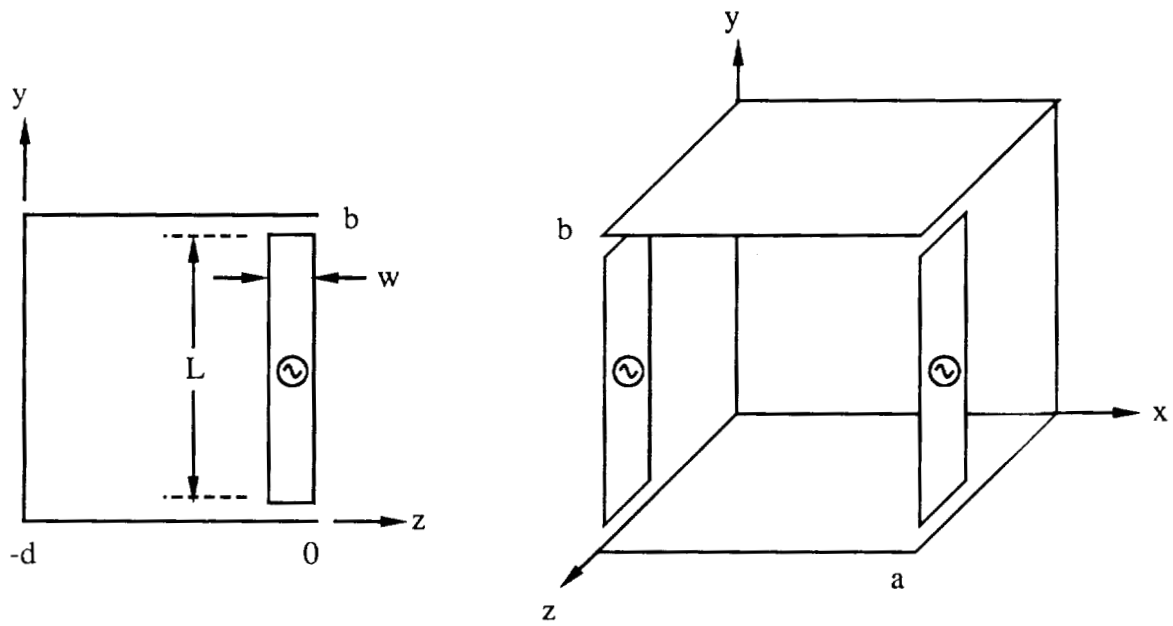


Figure 3.2.1. Strip dipole array configuration.

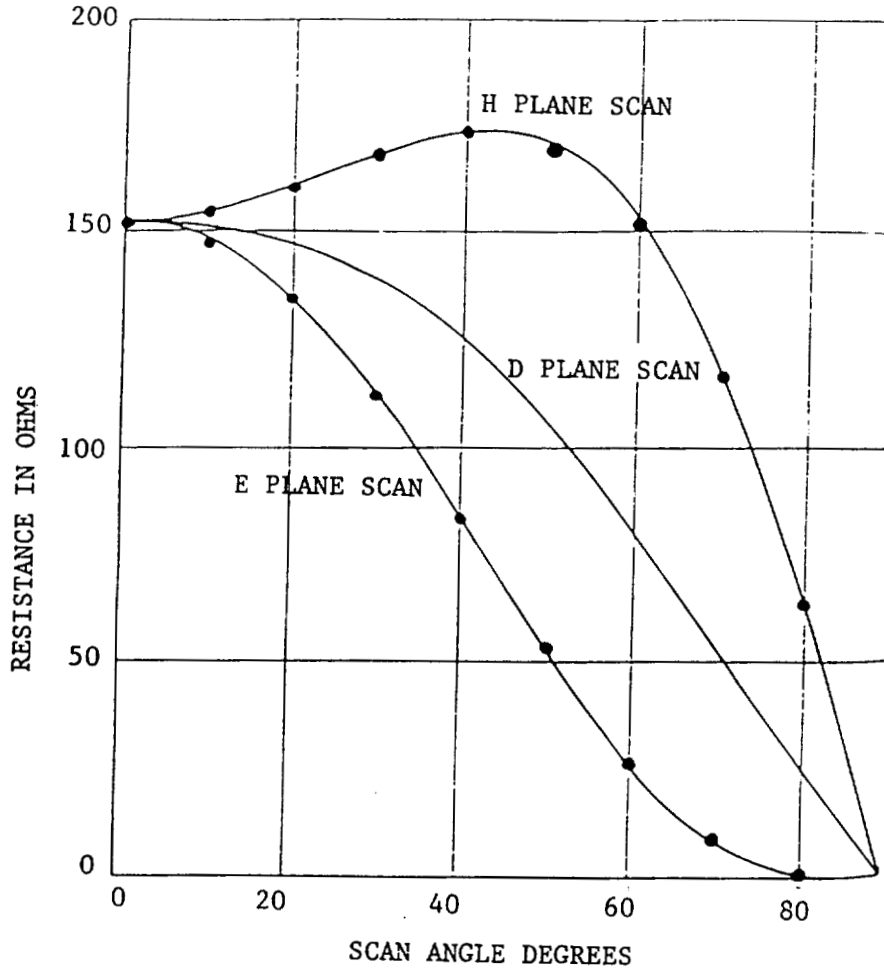


Figure 3.2.2. Resistance versus scan of 0.5-wavelength dipoles 0.25-wavelength above ground plane. $a = b = 0.5$ wavelength.

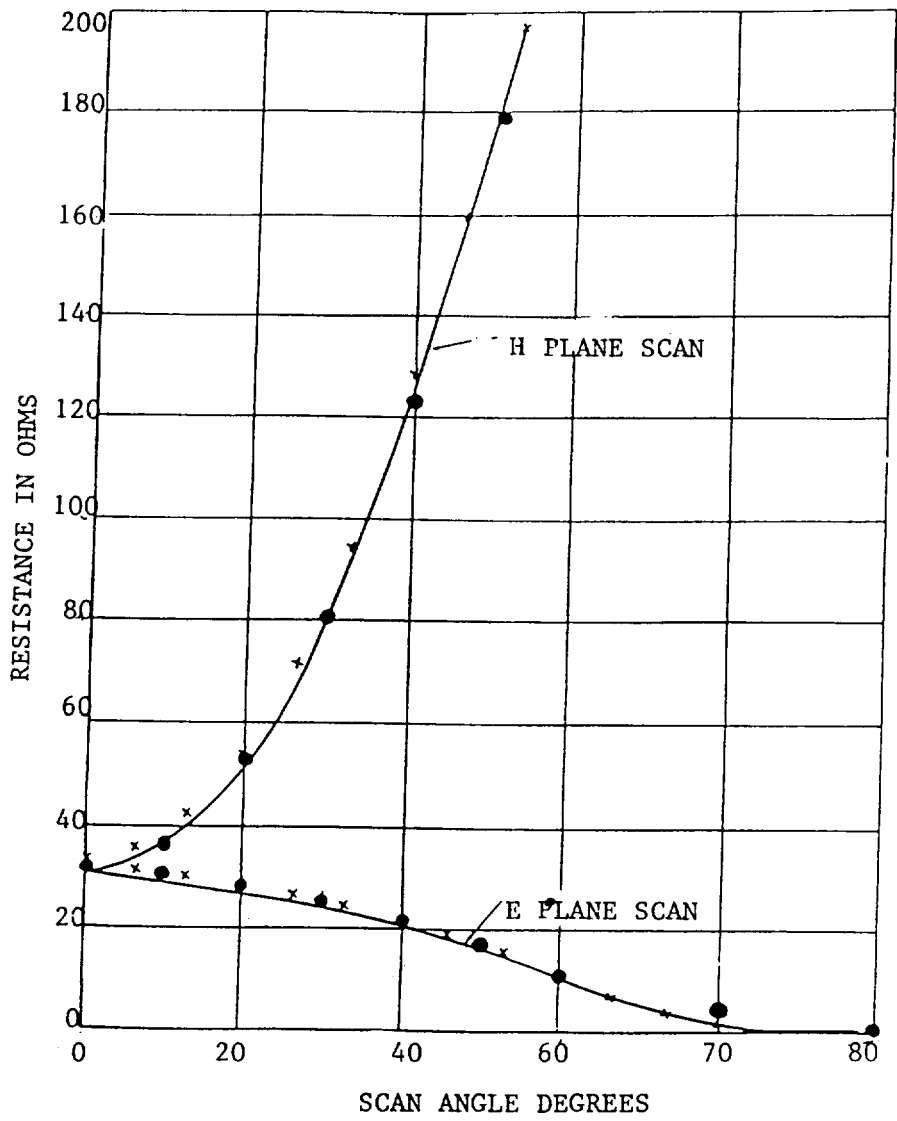


Figure 3.2.3. Reactance versus scan of 0.5-wavelength dipoles 0.25-wavelength above ground plane. $a = b = 0.5$ wavelength.

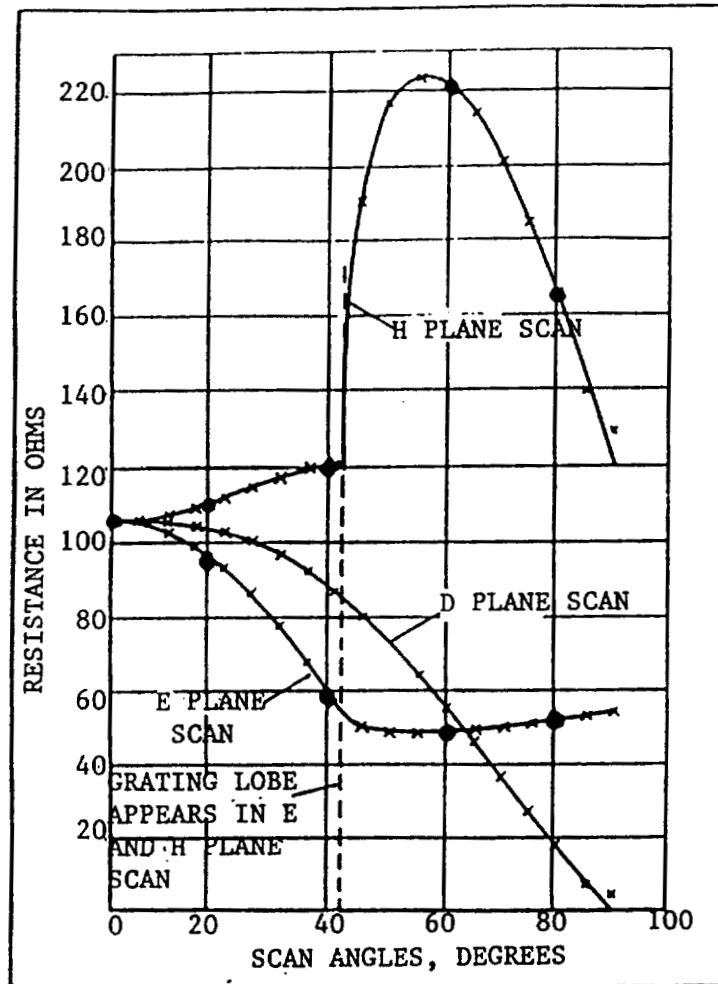


Figure 3.2.4. Resistance versus scan of 0.5-wavelength dipoles 0.25-wavelength above ground plane. $a = b = 0.6$ wavelength.

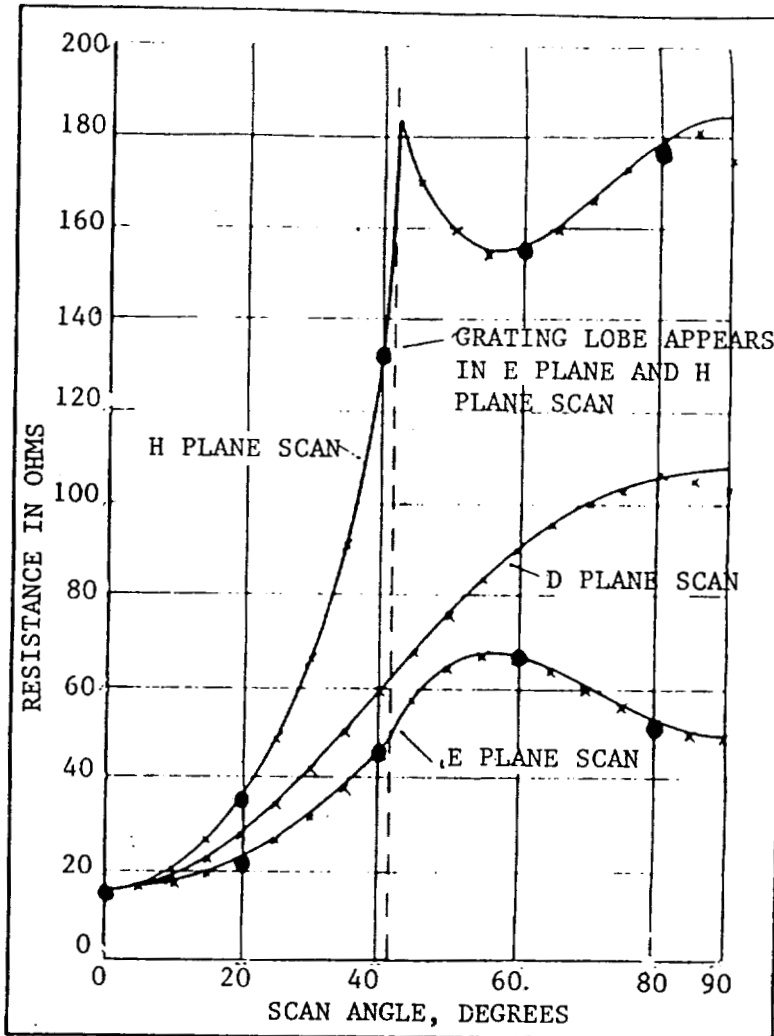


Figure 3.2.5. Reactance versus scan of 0.5-wavelength dipoles 0.25-wavelength above ground plane. $a = b = 0.6$ wavelength.

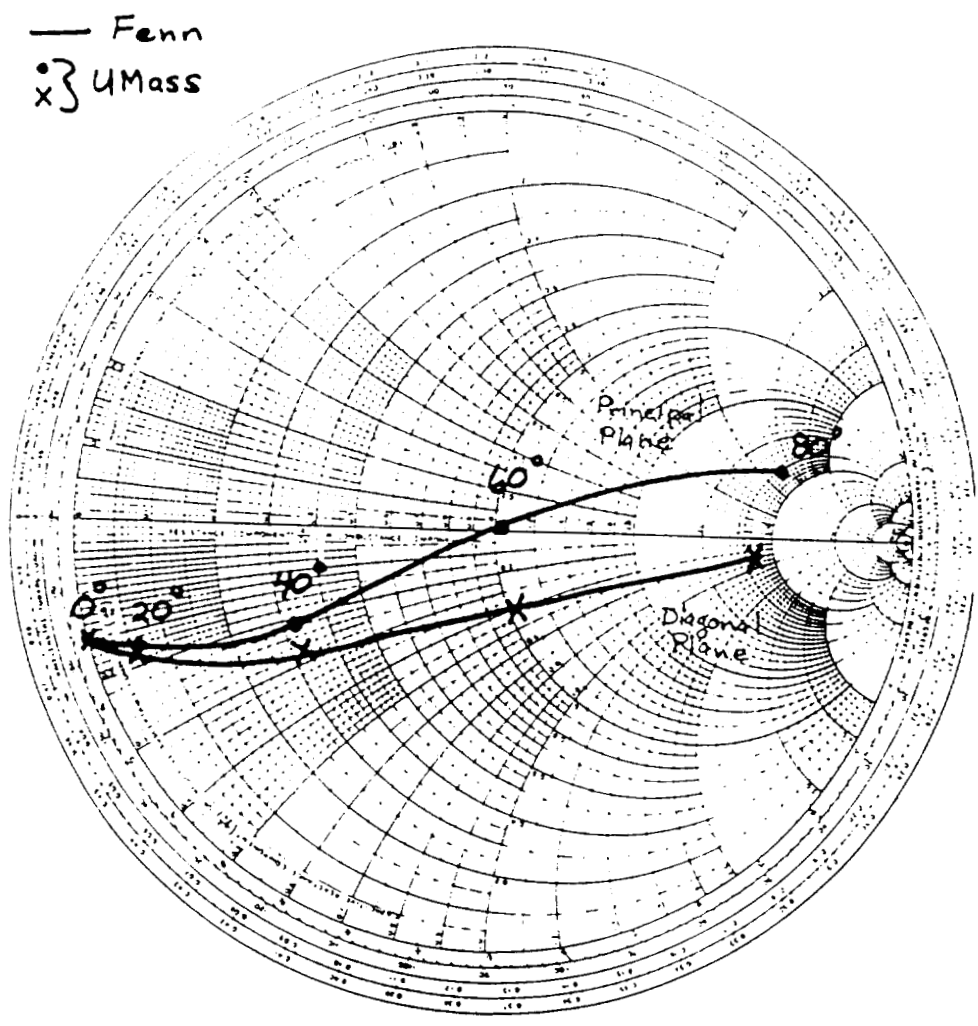


Figure 3.2.6. Comparison of calculations with SPECASMNASA to those of Fenn [7]. Fenn's data points coincide nearly perfectly with the points plotted for UMass.

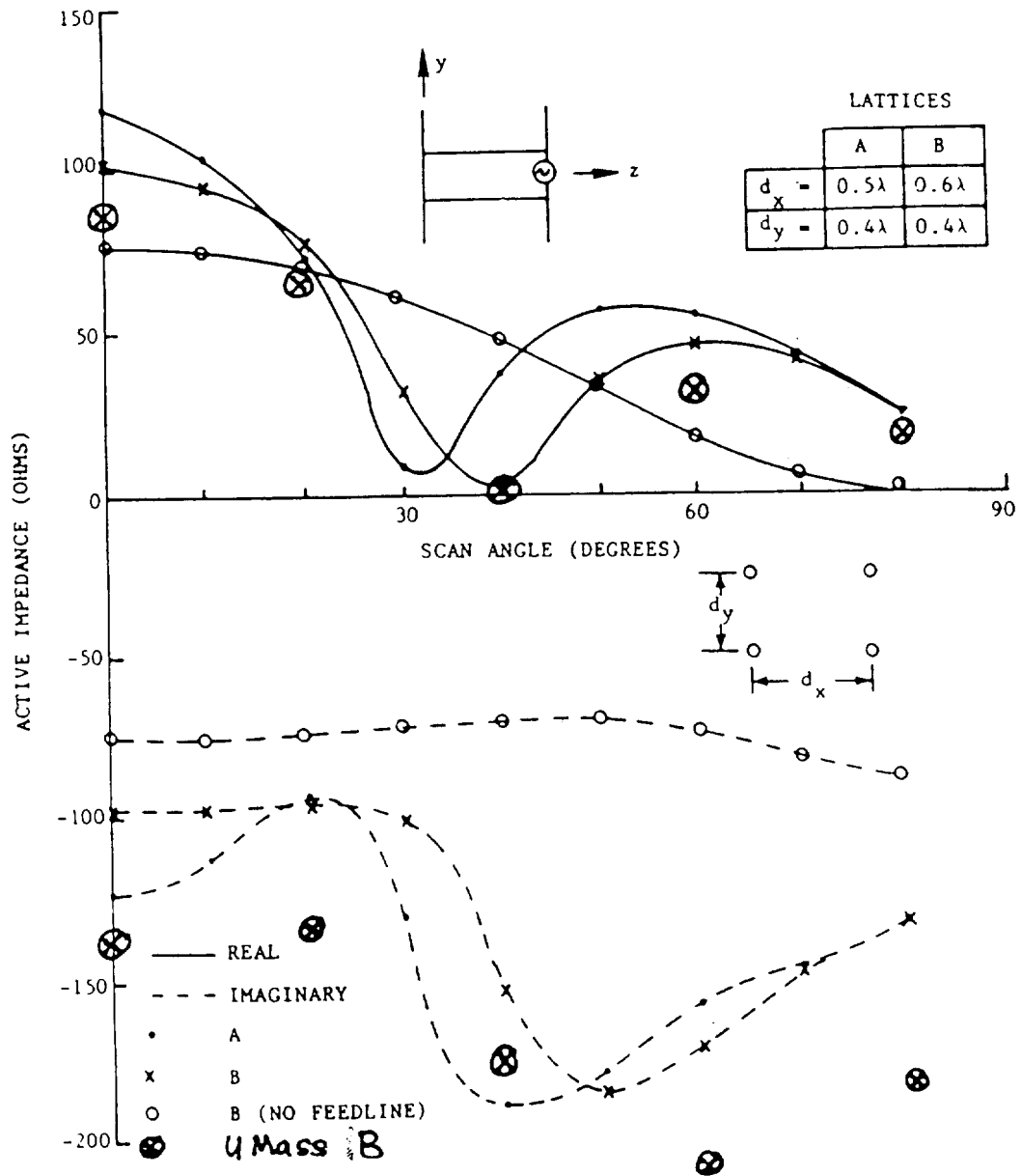


Figure 3.2.7. Dipole over ground with two-wire balun. UMass data for case B plotted on graph from [8].

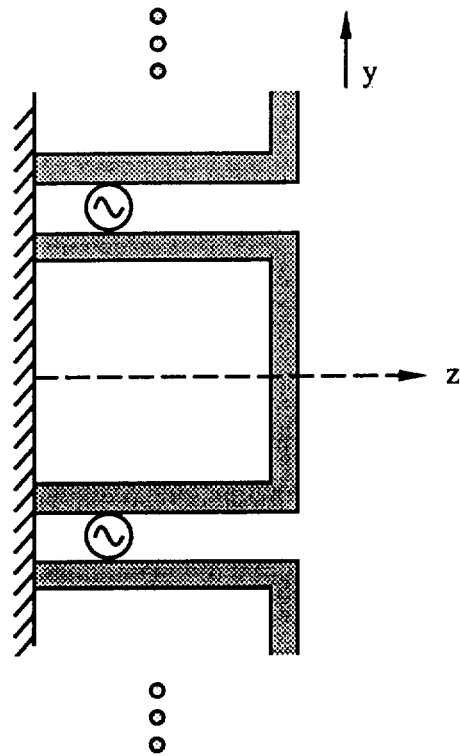
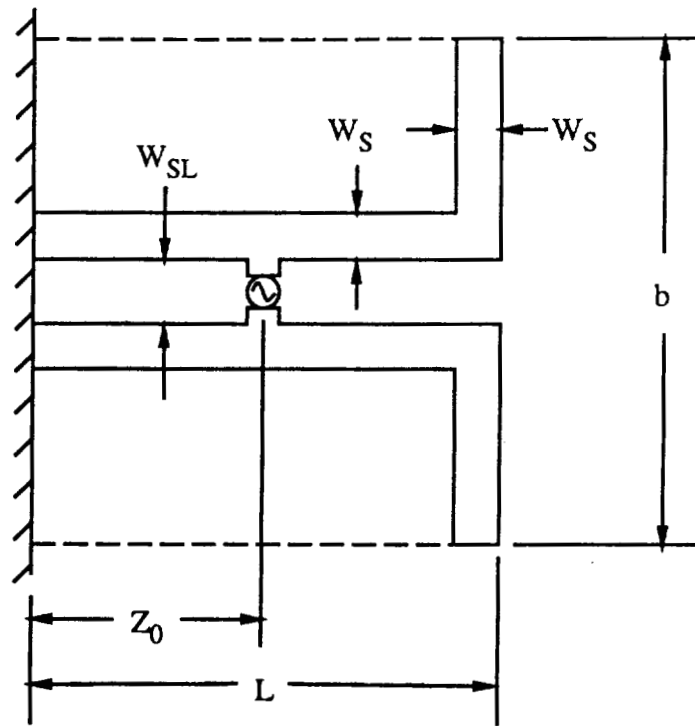


Figure 3.2.8. Strip-loop antenna array used as test case of computer program.



$$a = 2.377 \text{ cm}$$

$$b = 2.215 \text{ cm}$$

$$Z_0 = 3.00 \text{ cm}$$

$$L = 4.50 \text{ cm}$$

$$W_S = .250 \text{ cm}$$

$$W_{SL} = .200 \text{ cm}$$

Figure 3.2.9. Dimensions of strip-loop antenna.

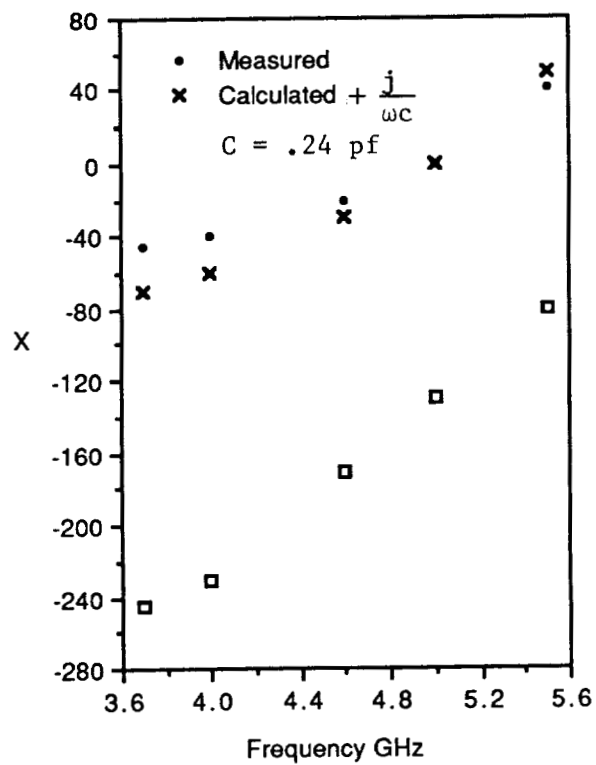
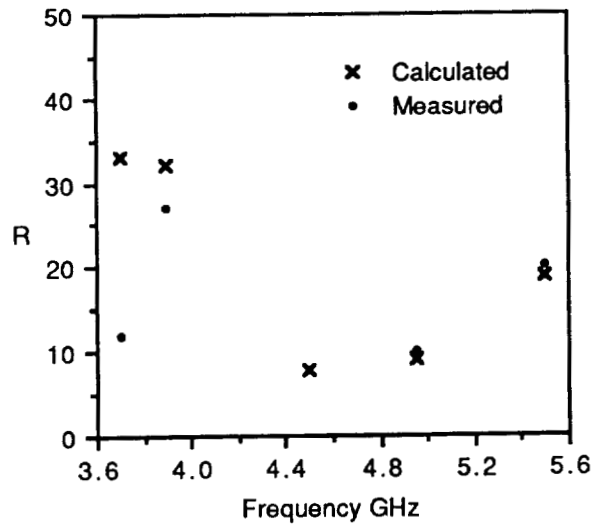


Figure 3.2.10. Measured and calculated impedance of strip-loop antenna in waveguide simulator. Square boxes of reactance plot are raw computations and Xs are obtained by removing an equivalent capacitance of 0.24 pf.

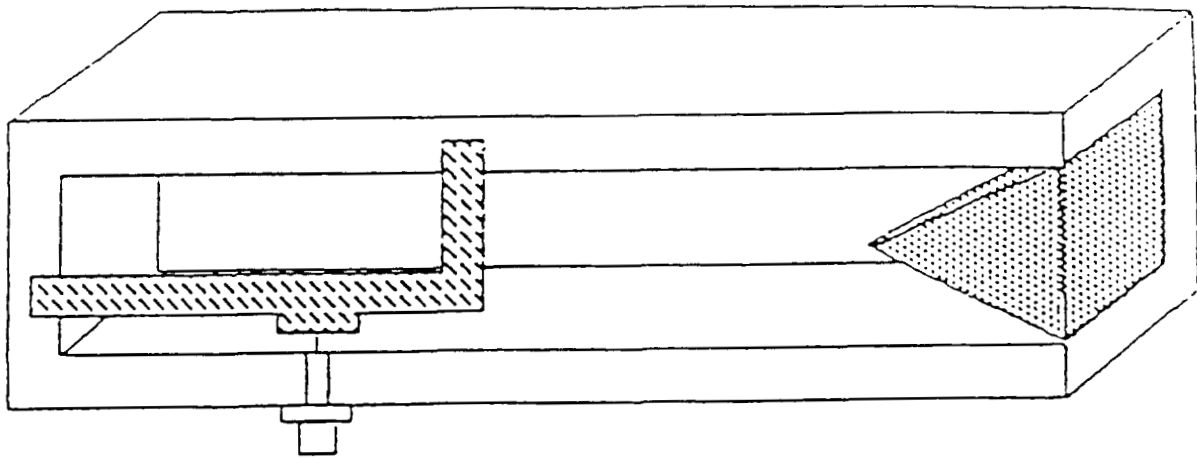
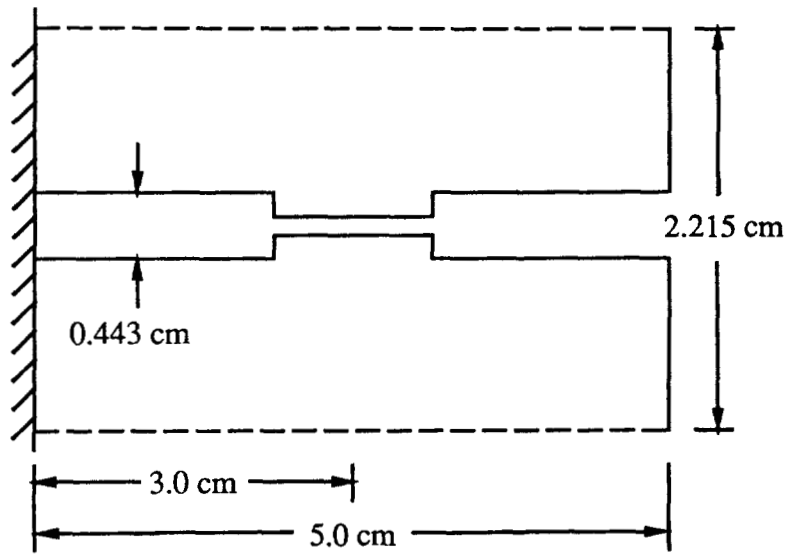


Figure 3.2.11. Waveguide simulator for strip-loop array.



$$a = 2.377 \text{ cm}$$

Figure 3.2.12. Dimensions of CWSA element.

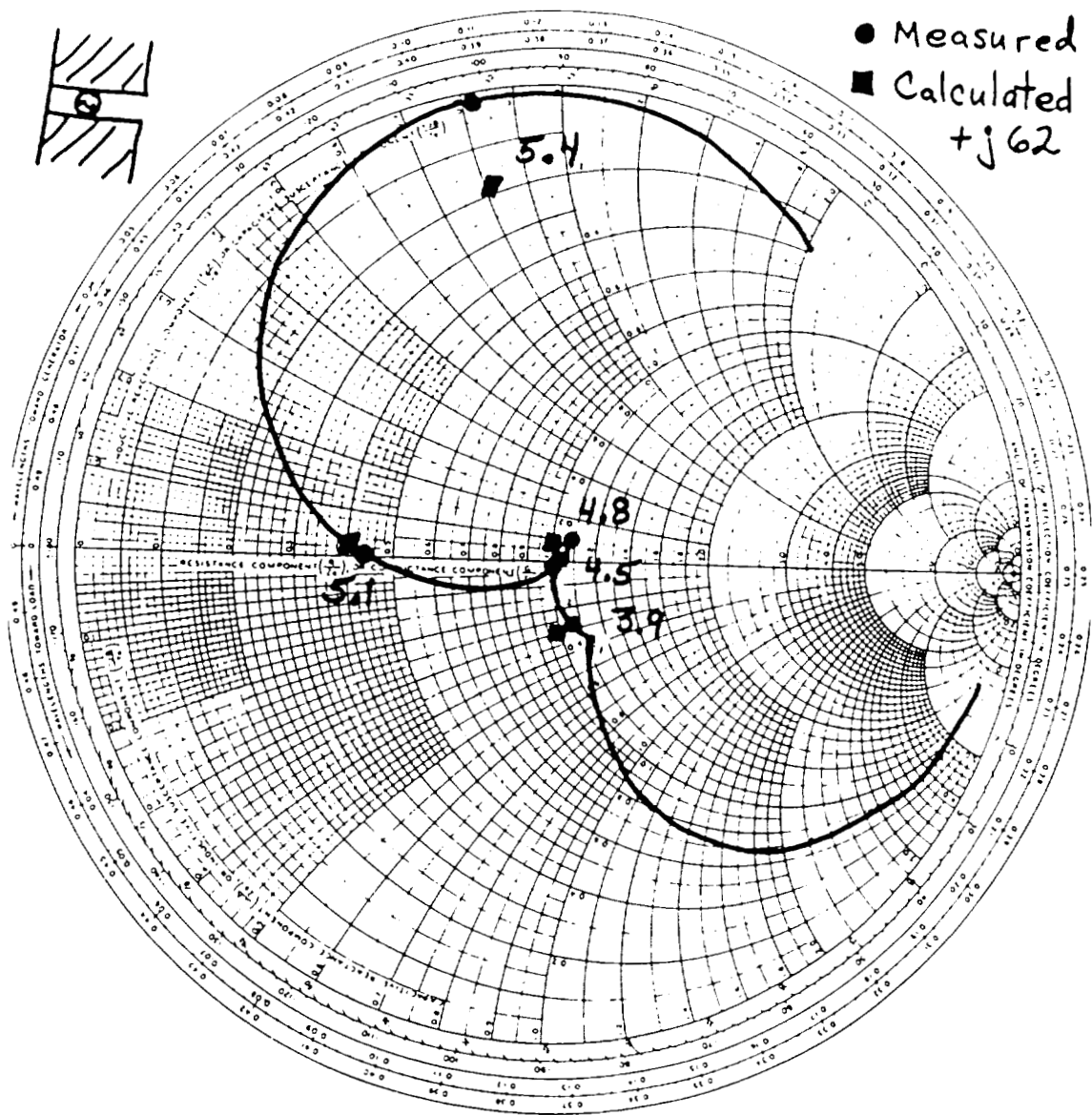
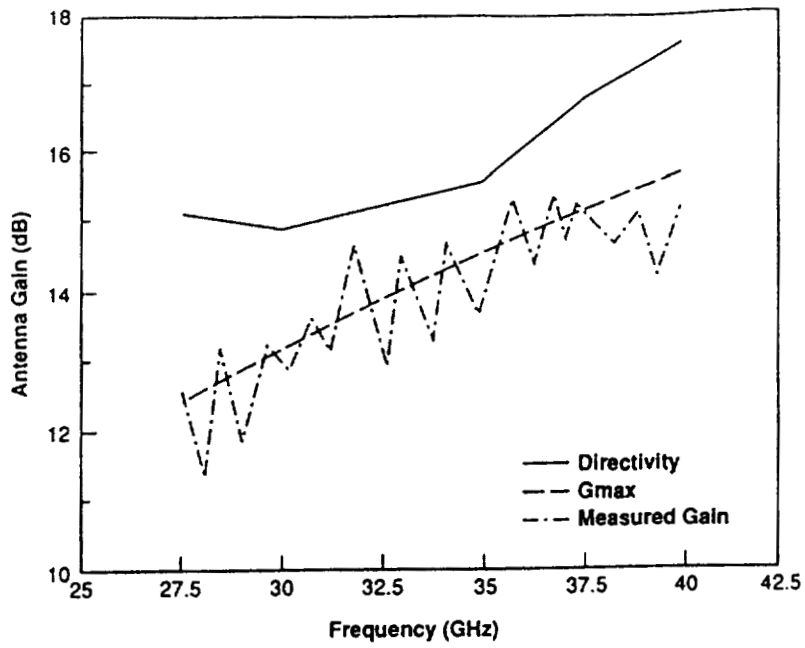
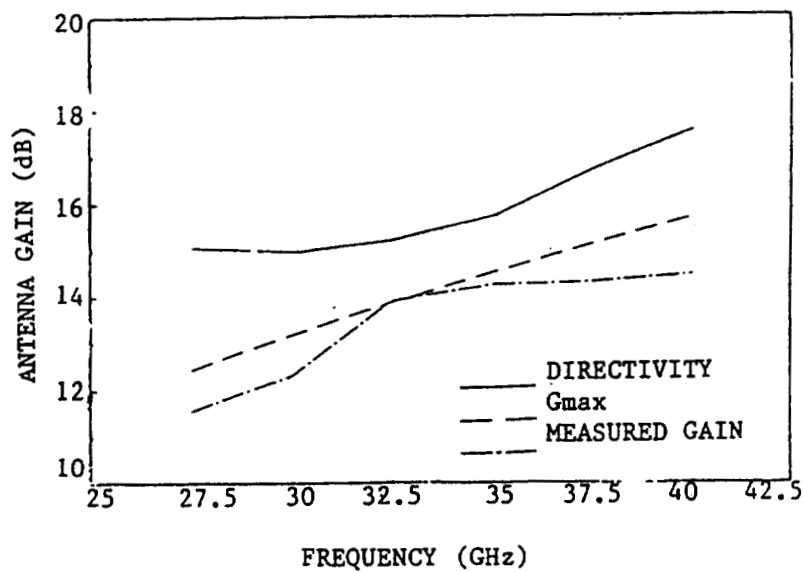


Figure 3.2.13. Measured and calculated impedance of CWSA array. Calculated data are adjusted for excess capacitive reactance of 62 ohms.



(a)



(b)

Figure 3.4.1. Comparison of the measured gain, G_{max} , and directivity of the 5×5 array center element with $d/\lambda = 1.5$: (a) $2\gamma = 7.5^\circ$ and $L/\lambda = 10$, and (b) $2\gamma = 11.2^\circ$ and $L/\lambda = 7.6$.

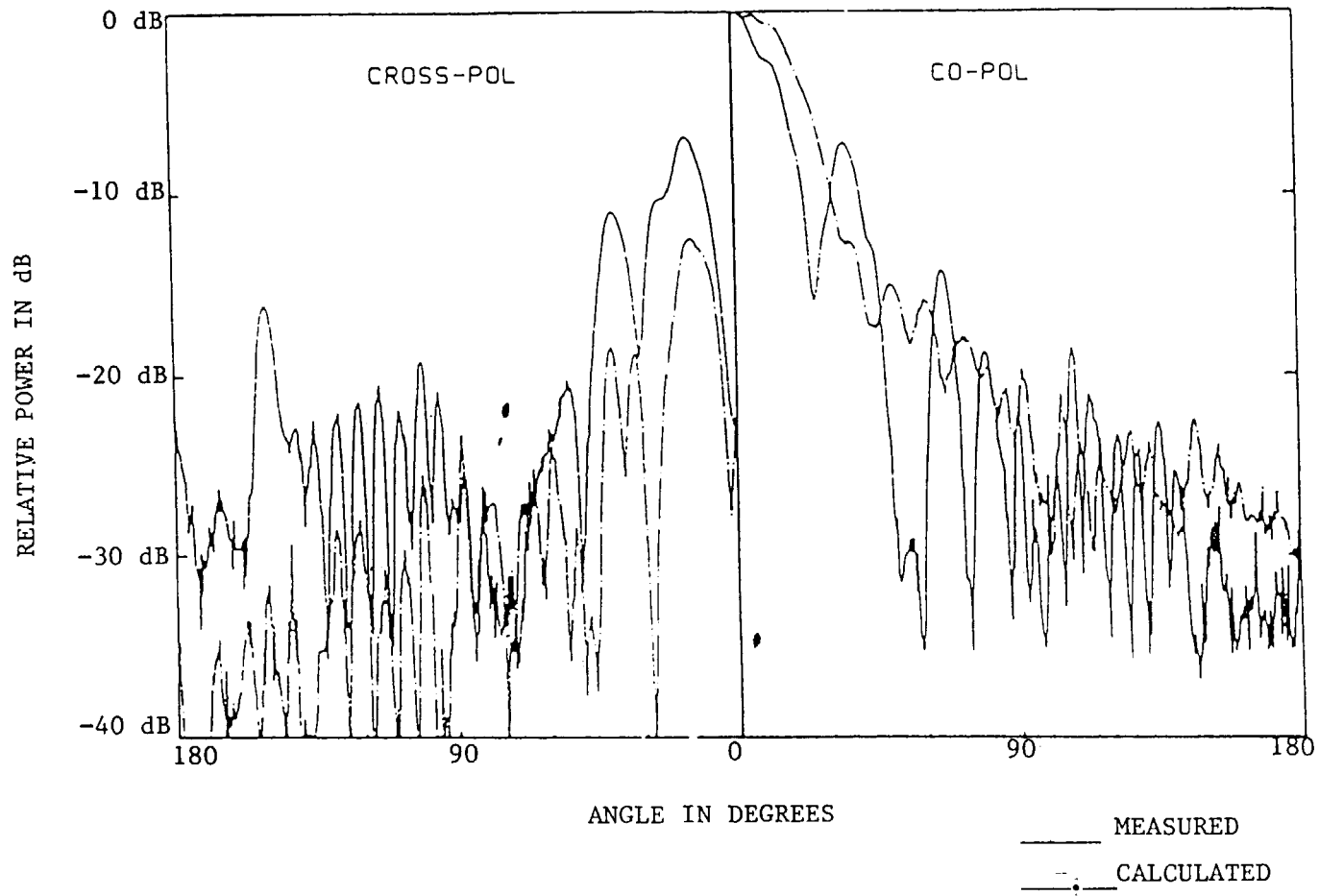
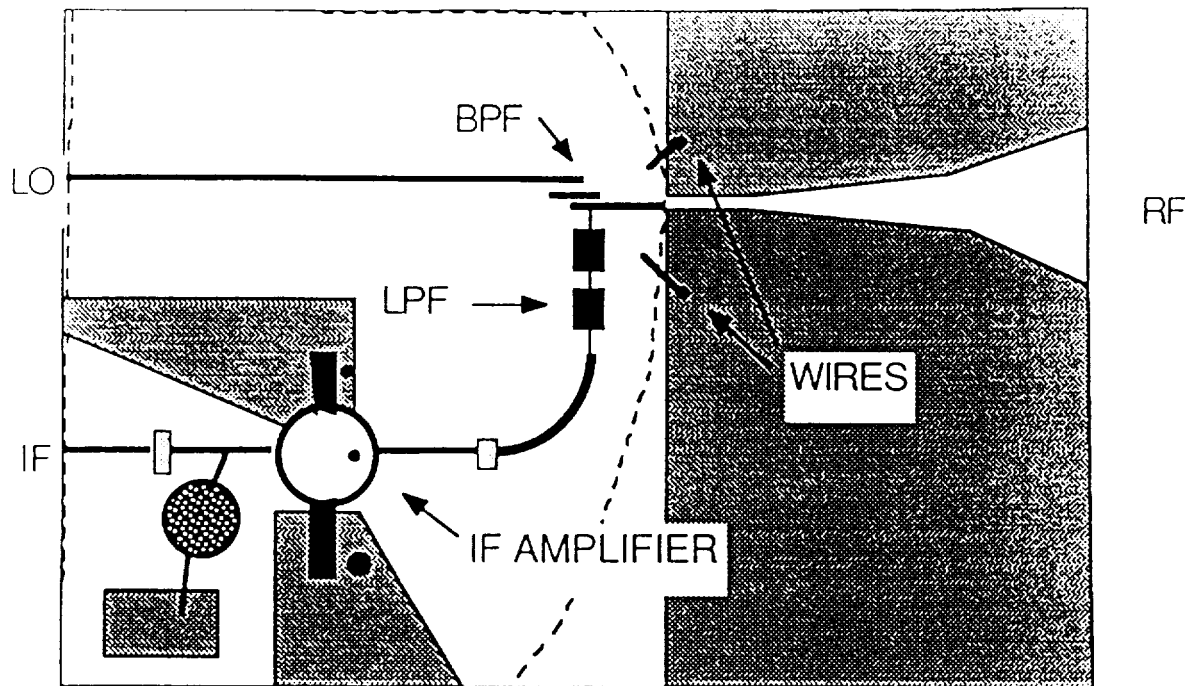

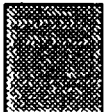


Figure 3.4.2. Comparison of calculated and measured patterns in the D-plane of the center element in an LTSA array with $d/\lambda = 1.5$.



 = Ground plane on bottom of substrate..

 = Ground plane on top of substrate.

NOTE: The amplifier circuit is explained in detail in section 3.1.4

Figure 4.1 General layout of the balanced mixer.

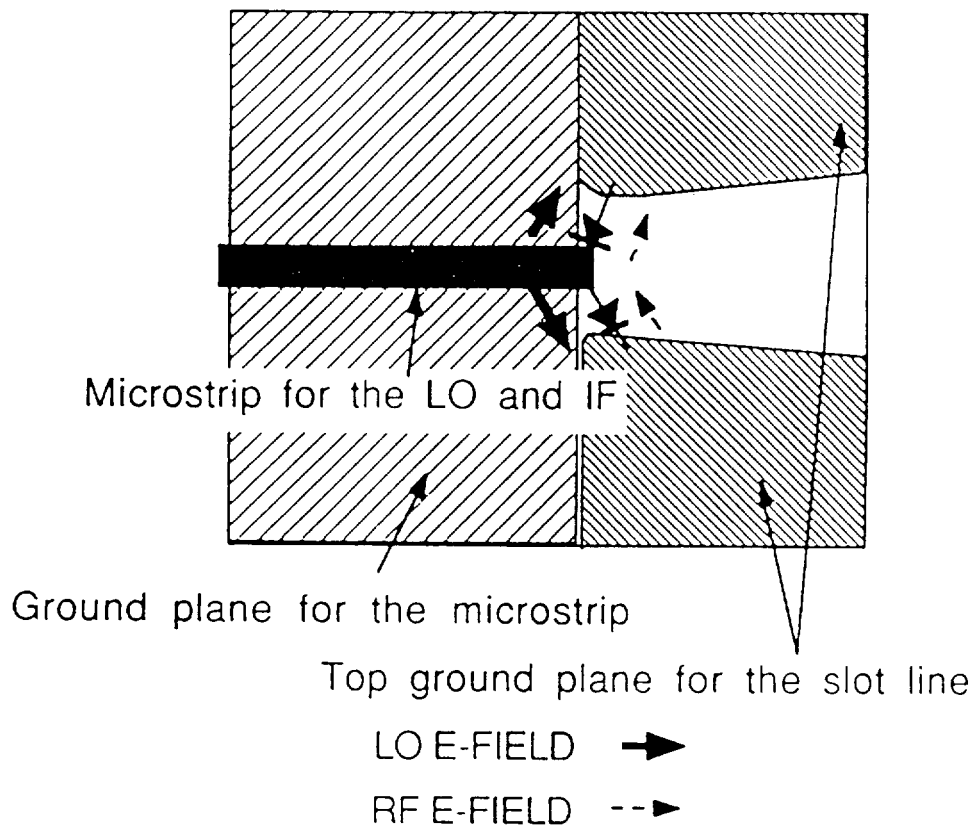


Figure 4.2. Detailed layout of the mixer.

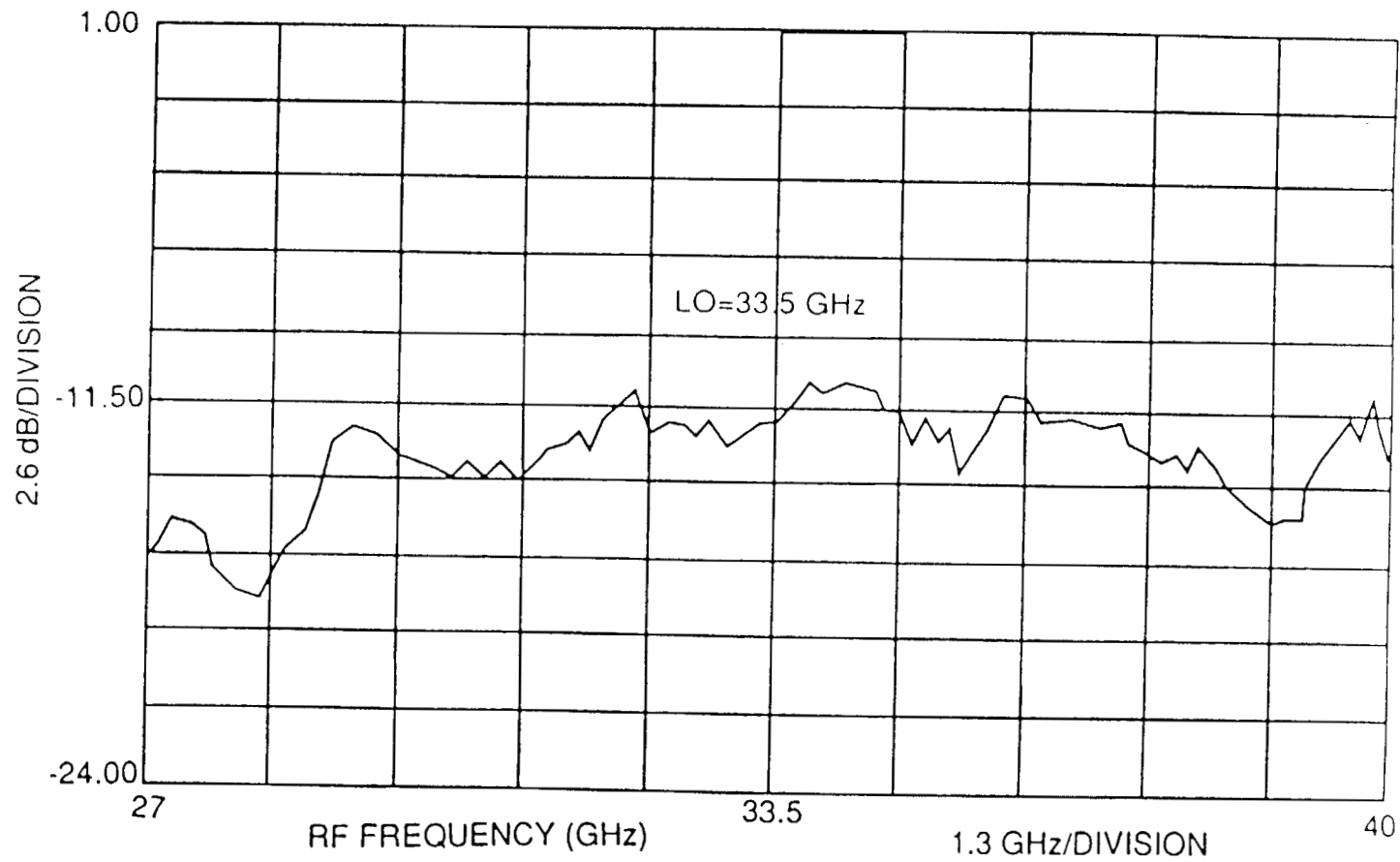


Figure 4.3. Conversion loss versus frequency for the mixer shown in Figure 4.2.

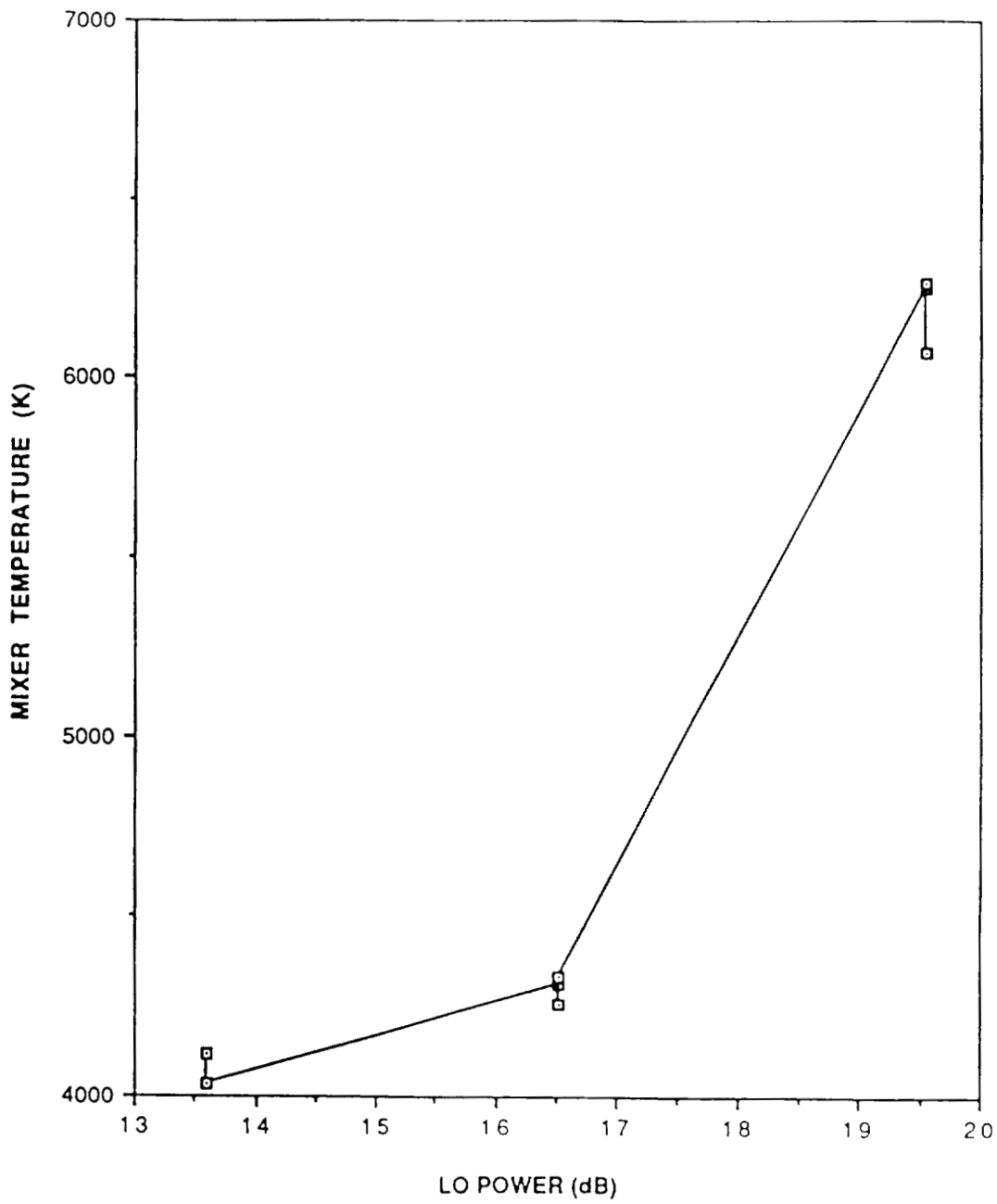


Figure 4.4. Mixer noise temperature versus LO power.

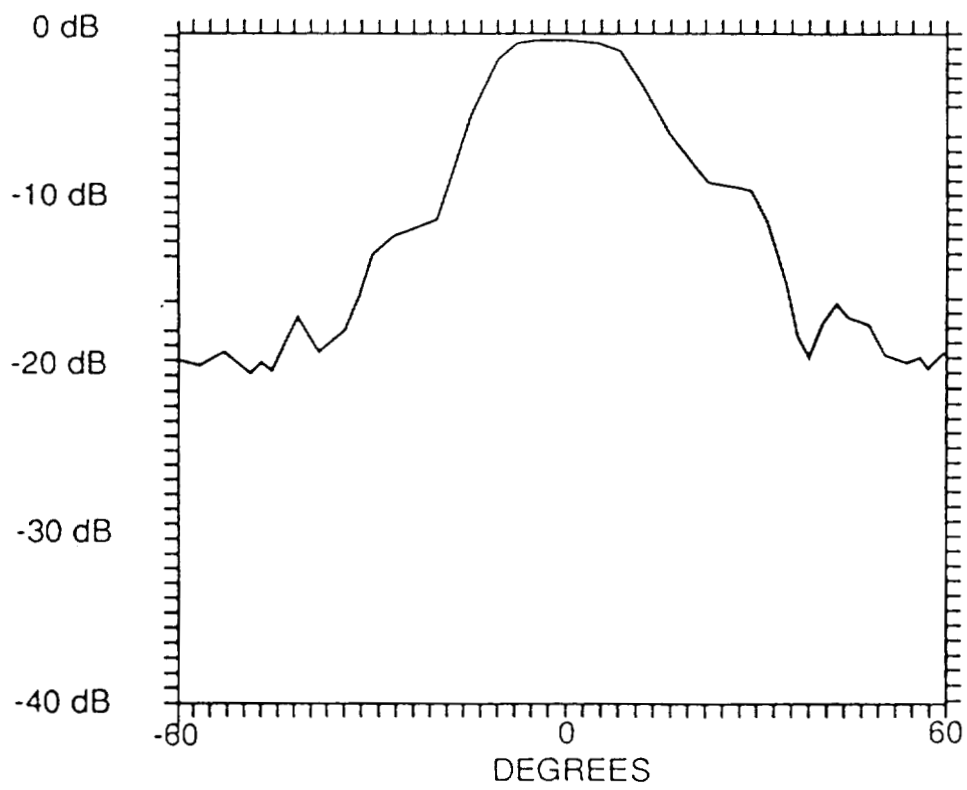


Figure 4.5a

Figure 4.5. Radiation patterns of the mixer integrated with a Vivaldi antenna.

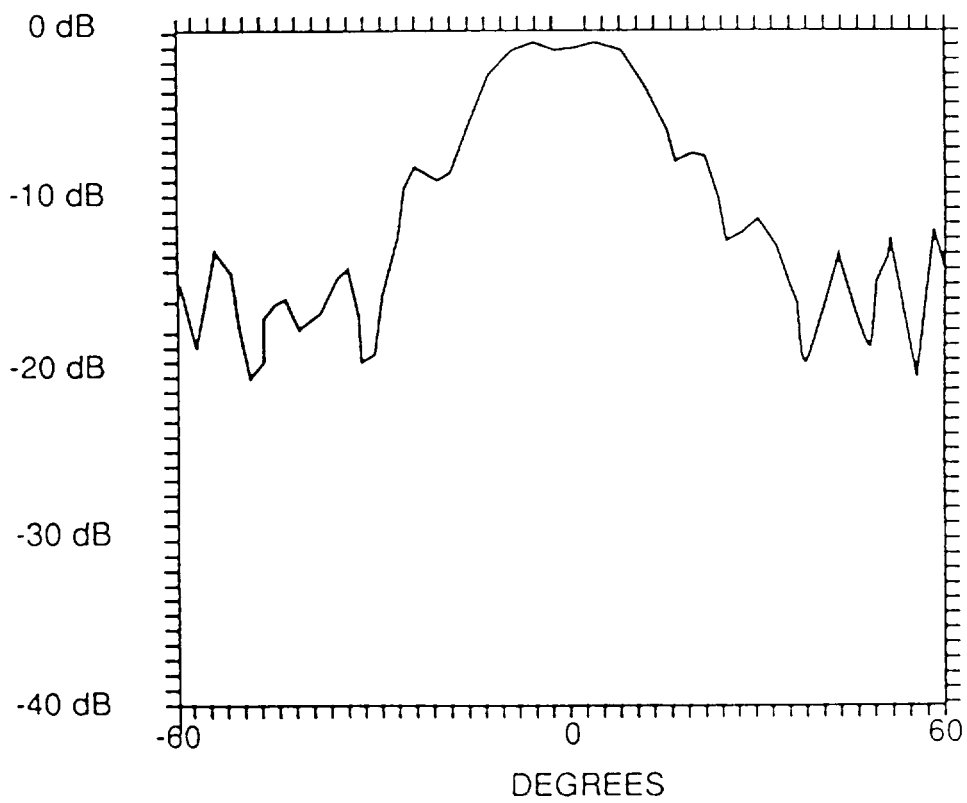


Figure 4.5b

```
# SET DEF [SCHAUBERT.NASA]
# FUN SPECASMNASA
SCHUMAN
SCHUMANOUT
# EXIT
```

Figure B1

```

TEST CASE FOR COMPARISON TO SCHUMAN, ET AL
0.6,0.4,      A,B(METERS)
0.3,          FREQ(GHZ)
7,12,1.,     * OF X MODES,* OF Z MODES,KE/KO OF SOURCE FIVE
20.,30.,60.,45.,2,1, THETA0,PHI0,CTHETA,CPHI,NTHETA,NPHI(FOR SCAN)
150,0.0001,  ALPMA/KO USED FOR INTEGRAL,TOLERANCE TO STOP
15,          NMAX USED IN SUMMATION
0.09375,0.25,0.09375,0.02  Y_CEN,Z_CEN,H/W OF NECESSARY MODES FOLLOWED BY I
0.18750,0.25,0.09375,0.02
0.28125,0.25,0.09375,0.02
0.14625,0.25,0.02000,0.02
0.16625,0.25,0.02000,0.02
0.20875,0.25,0.02000,0.02
0.22875,0.25,0.02000,0.02
0.15625,0.000,0.065,0.02
0.15625,0.065,0.065,0.02
0.15625,0.130,0.065,0.02
0.15625,0.195,0.065,0.02
0.15625,0.220,0.020,0.02
0.15625,0.240,0.020,0.02
0.21875,0.000,0.065,0.02
0.21875,0.065,0.065,0.02
0.21875,0.130,0.065,0.02
0.21875,0.195,0.065,0.02
0.21875,0.220,0.020,0.02
0.21875,0.240,0.020,0.02
2,          RCEN (MODE NUMBER TO WHICH SOURCE IS APPLIED)

```

Figure B2

ORIGINAL PAGE IS
OF POOR QUALITY

```

* IS FOR (SCHUMER) (DATA)
* FOR SPECASIMASH
ENTER NAME OF INPUT DATA FILE
SCHUMAN
ENTER NAME OF OUTPUT FILE
SCHUMANOUT

```

PROGRAM SPECASM

26-JUL-89 16:25:49

TEST CASE FOR COMPARISON TO SCHUMAN, ET AL

```

A = 0.60000 B = 0.40000 FREQ = 0.300
ALPHA INTEGRATION CARRIED OUT TO 150.0 K_0 WITH TOLERANCE = 0.100E-03
RADIUS AROUND POLE IS 0.00100 TIMES K_0
FLOQUET SUM TO 15 MODES

```

```

7 Y-DIRECTED MODES ARE USED WITH K_E/K_0 = 1.0000
* Y_CENTER Z_CENTER HALF-LENGTH WIDTH EDGE UNKN #
1 0.09375 0.25000 0.09375 0.02000 0 1
2 0.18750 0.25000 0.09375 0.02000 0 2
3 0.28125 0.25000 0.09375 0.02000 0 3
4 0.14625 0.25000 0.02000 0.02000 0 4
5 0.16625 0.25000 0.02000 0.02000 0 5
6 0.20875 0.25000 0.02000 0.02000 0 6
7 0.22875 0.25000 0.02000 0.02000 0 7

```

```

12 Z-DIRECTED MODES ARE USED WITH K_E/K_0 = 1.0000
* Y_CENTER Z_CENTER HALF-LENGTH WIDTH EDGE UNKN #
1 0.15625 0.00000 0.06500 0.02000 1 8
2 0.15625 0.06500 0.06500 0.02000 0 9
3 0.15625 0.13000 0.06500 0.02000 0 10
4 0.15625 0.19500 0.06500 0.02000 0 11
5 0.15625 0.22000 0.02000 0.02000 0 12
6 0.15625 0.24000 0.02000 0.02000 0 13
7 0.21875 0.00000 0.06500 0.02000 1 14
8 0.21875 0.06500 0.06500 0.02000 0 15
9 0.21875 0.13000 0.06500 0.02000 0 16
10 0.21875 0.19500 0.06500 0.02000 0 17
11 0.21875 0.22000 0.02000 0.02000 0 18
12 0.21875 0.24000 0.02000 0.02000 0 19

```

DRIVEN ELEMENT IS * 2

SCAN ANGLE IS 20.00 90.00

COMPLETED Z_YY CPU TIME AT BEGINNING OF ZYYFIL = 2.70 SEC

COMPLETED Z_YZ CPU TIME AT BEGINNING OF ZYZFIL = 533.93 SEC

COMPLETED Z_ZZ CPU TIME AT BEGINNING OF ZZZFIL = 2918.52 SEC
CPU TIME AT END OF ZZZFIL = 5951.77 SEC

```

CURRENT DISTRIBUTION
1 0.2560E-02 0.3557E-02
2 0.2950E-02 0.6007E-02
3 0.2882E-02 0.4671E-02
4 0.1759E-03 -0.3598E-03
5 -0.1194E-03 -0.3225E-03
6 -0.1239E-03 -0.9050E-03
7 0.1801E-03 0.4358E-03
8 -0.1513E-02 -0.2595E-02
9 -0.1405E-02 -0.2306E-02
10 -0.1099E-02 -0.1504E-02
11 -0.6690E-03 -0.3803E-03
12 -0.6717E-04 0.2599E-03
13 -0.1587E-03 0.4139E-03
14 0.1260E-02 0.5999E-02
15 0.1171E-02 0.5597E-02
16 0.9241E-03 0.4447E-02
17 0.5998E-03 0.2793E-02
18 0.9253E-04 0.3034E-03
19 0.2024E-03 0.6935E-03

```

Figure B3

ORIGINAL PAGE IS
OF POOR QUALITY

SCAN ANGLE IS 80.00 90.00

COMPLETED Z_YY CPU TIME AT BEGINNING OF ZYYFIL = 5954.86 SEC
COMPLETED Z_YZ CPU TIME AT BEGINNING OF ZYZFIL = 6494.14 SEC
CPU TIME AT BEGINNING OF ZZZFIL = 9179.15 SEC
CPU TIME AT END OF ZZZFIL = 12192.32 SEC

COMPLETED Z_ZZ

CURRENT DISTRIBUTION

1	-0.1228E-03	0.3815E-02
2	0.5246E-03	0.5417E-02
3	0.7718E-03	0.3115E-02
4	-0.1648E-03	0.1607E-03
5	0.1269E-03	-0.6861E-03
6	-0.5377E-04	-0.4828E-03
7	0.9497E-04	-0.1253E-03
8	0.4623E-03	-0.4680E-02
9	0.4526E-03	-0.4324E-02
10	0.4263E-03	-0.3320E-02
11	0.4160E-03	-0.1893E-02
12	0.1411E-03	-0.1070E-03
13	0.2723E-03	-0.3047E-03
14	0.3911E-03	0.3542E-02
15	0.3681E-03	0.3233E-02
16	0.3059E-03	0.2362E-02
17	0.2403E-03	0.1095E-02
18	0.6447E-04	-0.1043E-03
19	0.1295E-03	-0.1116E-03

ZIN = 0.1771E+02 -0.1829E+03

* EXIT

SCHAUBERT job terminated at 26-JUL-1989 22:41:21.11

Accounting information:

Buffered I/O count:	59	Peak working set size:	724
Direct I/O count:	915	Peak page file size:	4487
Page faults:	768	Mounted volumes:	0
Charged CPU time:	0 03:23:16.80	Elapsed time:	0 06:15:38.27

Figure B3 (cont.)

TEST CASE FOR COMPARISON TO SCHUMAN, ET AL

A = 0.60000 B = 0.40000 FREQ = 0.300
 ALPHA INTEGRATION CARRIED OUT TO 150.0 K_0 WITH TOLERANCE = 0.100E-03
 RADIUS AROUND POLE IS 0.00100 TIMES K_0
 FLUXLET SUM TO 15 MODES,

7 X-DIRECTED MODES ARE USED WITH K_E/K_0 = 1.0000

#	Y_CENTER	Z_CENTER	HALF-LENGTH	WIDTH	EDGE	UNKN #
1	0.09375	0.25000	0.09375	0.02000	0	1
2	0.18750	0.25000	0.09375	0.02000	0	2
3	0.28125	0.25000	0.09375	0.02000	0	3
4	0.14625	0.25000	0.02000	0.02000	0	4
5	0.16625	0.25000	0.02000	0.02000	0	5
6	0.20875	0.25000	0.02000	0.02000	0	6
7	0.22875	0.25000	0.02000	0.02000	0	7

12 Z-DIRECTED MODES ARE USED WITH K_E/K_0 = 1.0000

#	Y_CENTER	Z_CENTER	HALF-LENGTH	WIDTH	EDGE	UNKN #
1	0.15625	0.00000	0.06500	0.02000	1	8
2	0.15625	0.06500	0.06500	0.02000	0	9
3	0.15625	0.13000	0.06500	0.02000	0	10
4	0.15625	0.19500	0.06500	0.02000	0	11
5	0.15625	0.22000	0.02000	0.02000	0	12
6	0.15625	0.24000	0.02000	0.02000	0	13
7	0.21875	0.00000	0.06500	0.02000	1	14
8	0.21875	0.06500	0.06500	0.02000	0	15
9	0.21875	0.13000	0.06500	0.02000	0	16
10	0.21875	0.19500	0.06500	0.02000	0	17
11	0.21875	0.22000	0.02000	0.02000	0	18
12	0.21875	0.24000	0.02000	0.02000	0	19

DRIVEN ELEMENT IS # 2

SCAN ANGLE IS 20.00 90.00

CPU TIME AT BEGINNING OF ZYYPIL = 2.70 SEC
 CPU TIME AT BEGINNING OF ZZZFIL = 538.93 SEC
 CPU TIME AT BEGINNING OF ZZZFIL = 2918.52 SEC
 CPU TIME AT END OF ZZZFIL = 5551.77 SEC

ZMAT(1 1) = 0.27060E+02 -0.75246E+03
 ZMAT(1 2) = 0.19635E+02 0.42374E+03
 ZMAT(1 3) = -0.56736E+01 0.11644E+03

 THE REMAINING MATRIX ELEMENTS APPEAR HERE

ZMAT(19 17) = 0.31767E-01 0.66297E+02
 ZMAT(19 18) = 0.64348E-02 0.57497E+03
 ZMAT(19 19) = 0.36705E-02 -0.16996E+04

CURRENT DISTRIBUTION

1	0.2560E-02	0.3557E-02
2	0.2350E-02	0.6007E-02
3	0.2582E-02	0.4671E-02
4	0.1759E-03	-0.3593E-03
5	-0.1194E-03	-0.3225E-03
6	-0.1239E-03	-0.9050E-03
7	0.1301E-03	0.4358E-03
8	-0.1513E-02	-0.2595E-02
9	-0.1405E-02	-0.2306E-02
10	-0.1099E-02	-0.1504E-02
11	-0.6690E-03	-0.3803E-03
12	-0.6717E-04	0.2599E-03

Figure B4

ORIGINAL PAGE IS
 OF POOR QUALITY

13	-0.1587E-03	0.4139E-03
14	0.1260E-02	0.5999E-02
15	0.1171E-02	0.5597E-02
16	0.9241E-03	0.4447E-02
17	0.5998E-03	0.2793E-02
18	0.9253E-04	0.3034E-03
19	0.2024E-03	0.6935E-03

ZIN = 0.6587E+02 -0.1341E+03

SCAN ANGLE IS 80.00 90.00

CPU TIME AT BEGINNING OF ZYYFIL = 5954.86 SEC
 CPU TIME AT BEGINNING OF ZYZFIL = 6494.14 SEC
 CPU TIME AT BEGINNING OF ZZZFIL = 9179.15 SEC
 CPU TIME AT END OF ZZZFIL = 12192.32 SEC

ZMAT(1 1) =	0.34858E+00	-0.75383E+03
ZMAT(1 2) =	-0.92664E+01	0.40905E+03
ZMAT(1 3) =	-0.30589E+02	0.50453E+02

 THE REMAINING MATRIX ELEMENTS APPEAR HERE

ZMAT(19 17) =	0.21831E+02	0.61096E+02
ZMAT(19 18) =	0.65935E+01	0.57373E+03
ZMAT(19 19) =	0.65567E+01	-0.17003E+04

CURRENT DISTRIBUTION

1	-0.1228E-03	0.3815E-02
2	0.5246E-03	0.5417E-02
3	0.7718E-03	0.3115E-02
4	-0.1648E-03	0.1607E-03
5	0.1269E-03	-0.6861E-03
6	-0.5377E-04	-0.4828E-03
7	0.9497E-04	-0.1253E-03
8	0.4623E-03	-0.4680E-02
9	0.4526E-03	-0.4324E-02
10	0.4263E-03	-0.3320E-02
11	0.4160E-03	-0.1893E-02
12	0.1411E-03	-0.1070E-03
13	0.2723E-03	-0.3047E-03
14	0.3911E-03	0.3542E-02
15	0.3681E-03	0.3233E-02
16	0.3059E-03	0.2362E-02
17	0.2403E-03	0.1095E-02
18	0.6447E-04	-0.1043E-03
19	0.1295E-03	-0.1116E-03

ZIN = 0.1771E+02 -0.1829E+03

Figure B4 (cont.)

ORIGINAL PAGE IS
 OF POOR QUALITY

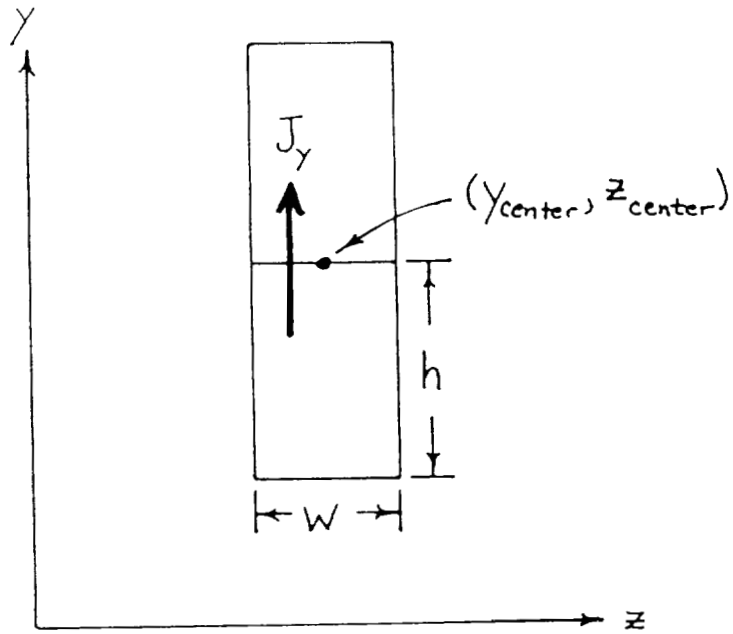


Figure B.5.

Definition of center coordinates, half-length (h), and width (w) for one expansion mode.

Appendix A: Description of the Computer Program for Analysis of LTSA-Type Arrays.

The computer program is written in VAX FORTRAN and is comprised of several modules, each containing routines associated with a portion of the computations. The modular concept was continued in the various routines, many of which contain blocks of codes identical to other routines within the module. It was felt that an efficient and accurate code could be more easily obtained by developing each routine as a separate entity with minimal branching. This results in a lengthy code, but it is easier to read, debug, and modify.

The modules comprising the program are:

- SPECASM: The main program, containing input and output statements and controlling execution by calling other routines when required.
- ZFILASM: Contains three routines that fill the submatrices Z_{ij} in equation (3.13). These routines perform the higher level operations and call other routines for numerical evaluation of most formulas.
- RQUAD: Adaptive quadrature routine for numerical evaluation of integrals in (3.14)–(3.17).
- INTR: Routines to evaluate alpha dependence of integrands in (3.14)–(3.17) when β_n is real.
- INTI: Routines to evaluate alpha dependence of integrands in (3.14)–(3.17) when β_n is imaginary. (The cases for β_n real and imaginary are treated separately so that real arithmetic can be used throughout the time-consuming evaluations of (3.14)–(3.17). Using complex arithmetic would increase execution time substantially.)
- INTIAS: Routines to evaluate the integrand of the first integral on the right-hand side of equation (3.28).

CUR: Routines to evaluate the factors in (3.26) and (3.27) that are not dependent on alpha. These factors are evaluated once.

ASYM: Routines to control the asymptotic evaluations related to equation (3.28).

POLE: Locates poles of $K(\beta_n)$.

RES: Evaluates residues of (3.14)–(3.17) at the poles of $K(\beta_n)$.

EXCVEC: Fills the right-hand-side vector of equation (3.13).

MATRIX: Matrix solution routines.

Appendix B: Using the Computer Program

The program is written to query the user for interactive entry of the names of input and output data files. However, it is usually executed in batch mode by submitting a command file like the one in Figure B.1. This file and the discussion of this appendix relate to execution under the DEC VMS operating system. The line following the run command is the name of the file where input data are available and the next line is the name of a file to which additional output data are written. All of the output data normally needed by the user are written to the system output device, which is the log file for batch execution and the screen for interactive execution. A sample input data file is shown in Figure B.2 and the associated log file and output file are shown in Figures B.3 and B.4.

The sample log file contains the following information:

1. Program name and date and time of execution.
2. Identifying information.
3. Grid spacings in meters and frequency in GHz.
4. Maximum value of alpha that is used for evaluating the integrals in (3.14)–(3.17) and the relative accuracy used to terminate the adaptive quadrature routine.
5. Radius of semicircular arc around pole of $K(\beta_n)$. Numerical integration is used for values of alpha outside this limit, and the analytical residue yields the value on the arc.
6. $|n_{\max}|$ used for the summations in (3.14)–(3.17).
7. Model segmentation information. Each expansion mode is described by its center coordinates, half-length (h) and width (w) as shown in Figure B.5. Modes of J_z that

are centered at the ground plane are half modes and are denoted by an edge parameter of 1. All dimensions are in meters.

8. Number of the mode representing the feed. A delta gap voltage source is used in this program.
9. Theta and phi values of the array scan angle.
10. CPU time for the matrix fill. The time denoted for $ZYZF1L$ is for both Z_{yz} and Z_{zy} because these two submatrices are filled simultaneously.
11. Expansion coefficients obtained by solution of the matrix equation.
12. Input impedance, real and imaginary parts.

Our experience with the program suggests that antennas can be modelled using criteria similar to those appropriate for other surface patch discretization schemes. For example, we have used the following guidelines:

1. Half-length between 0.125 and 0.025 wavelength.
2. Width less than half-length.
3. Near feeds and sharp discontinuities, additional patches that are 2 to 5 times smaller than the above guidelines often are required.
4. When metalization is continuous from cell to cell in the y direction, a J_y mode is centered at the lower cell boundary, and the upper most J_y mode ends at the upper cell boundary.
5. When metalization touches the ground plane at $z = 0$, a J_z mode, is centered at $z = 0$. This is recognized by the program as a half mode. The sizes and aspect ratios of the expansion modes have been varied outside the guidelines given by 1 and 2 and useful results have been obtained. Experimentation with grid schemes has not been extensive and the user should check convergence of solutions that are obtained and should also attempt to validate some results with simulator experiments.



Report Documentation Page

1. Report No. NASA CR-4417		2. Government Accession No.		3. Recipient's Catalog No.	
4. Title and Subtitle Development of Theoretical Models of Integrated Millimeter Wave Antennas			5. Report Date December 1991		
			6. Performing Organization Code		
7. Author(s) K. Sigfrid Yngvesson and Daniel H. Schaubert			8. Performing Organization Report No.		
			10. Work Unit No. 506-44-21-03		
9. Performing Organization Name and Address University of Massachusetts Department of Electrical and Computer Engineering Amherst, MA 01003			11. Contract or Grant No. NAS1-18310		
			13. Type of Report and Period Covered Contractor Report 8-20-86 to 8-19-89		
12. Sponsoring Agency Name and Address National Aeronautics and Space Administration Langley Research Center Hampton, VA 23665-5225			14. Sponsoring Agency Code		
			15. Supplementary Notes Langley Technical Monitor: M.C. Bailey Final Report		
16. Abstract <p>Extensive radiation patterns for <i>LTSA Single Elements</i> are presented in this report. The directivity of LTSA elements is predicted correctly by taking the cross-polarized pattern into account. A moment-method program predicts radiation patterns for air LTSAs with excellent agreement with experimental data.</p> <p>A moment-method program has also been developed for the task <i>LTSA Array Modeling</i>. Computations performed with this program are in excellent agreement with published results for dipole and monopole arrays, and with waveguide simulator experiments, for more complicated structures.</p> <p>Empirical modeling of LTSA arrays has demonstrated that the maximum theoretical element gain can be obtained. Formulations were also developed for calculating the aperture efficiency of LTSA arrays used in reflector systems. It was shown that LTSA arrays used in multi-beam systems have a considerable advantage in terms of higher packing density, compared with waveguide feeds.</p> <p>The task <i>Preliminary Design of a Mizer Suitable for Use With LTSA Arrays</i> has been completed. Conversion loss of 10 dB was demonstrated at 35 GHz.</p>					
17. Key Words (Suggested by Author(s)) Integrated Antenna Arrays, Millimeter Waves, Electromagnetic Modeling, Integrated Mixers			18. Distribution Statement Unclassified - Unlimited Subject Category 32		
19. Security Classif. (of this report) Unclassified		20. Security Classif. (of this page) Unclassified		21. No. of pages 96	22. Price A05